Person-specific Calibration of a Partial Body Counter

Pedro Miguel Agostinho Nogueira

Helmholtz Zentrum München
Institut für Strahlenschutz
Komm. Direktor: Dr. Peter Jacob

Person-specific Calibration of a Partial Body Counter

Dissertation
Zum Erwerb des Doktorgrades der Humanbiologie
an der Medizinischen Fakultät der
Ludwig-Maximilians-Universität zu München

vorgelegt von
Pedro Miguel Agostinho Nogueira
aus Torres Novas, Portugal
2014

Mit Genehmigung der Medizinischen Fakultät
der Universität München

Berichterstatter:	Prof. Dr. Werner Rühm
Mitberichterstatter:	Priv. Doz. Dr. Thomas Pfluger
	Prof. Dr. Katja Radon
Mitbetreuung durch den promovierten Mitarbeiter:	---
Dekan:	Prof. Dr. med. Dr. h.c. M. Reiser, FACR, FRCR
Tag der mündlichen Prüfung:	13.10.2014

Contents

Abstract

^{241}Am is a radionuclide of special concern due to its ability to replace calcium in the bone structure, and its emitted alpha particles which will deposit their energy on a short distance resulting in damage to the surrounding tissues, such as the bone marrow.

Direct measurements using detectors placed externally to the body are a typical method used to quantify protracted incorporations of ^{241}Am, as it allows a rapid determination of the radionuclide incorporated. However, such estimations are dependent on the calibration of such a partial body counter with an anatomical phantom containing a known activity of the radionuclide of interest, so that it simulates the characteristics of the measured individual. Differences in critical body parameters between the calibration phantom and the patient (e.g. size, shape, or activity distribution) will bias the determination of the incorporated activity and related dose, and increase the associated uncertainty. The improvement of the measurement calibration is then fundamental for the improvement of the estimation of the incorporated ^{241}Am activity, which can also be used to provide more accurate data for the biokinetic models.

As part of this thesis, the Helmholtz Center Munich (HMGU) partial body counter (PBC) dedicated to detect incorporated low-energy "bone seeking" radionuclides has been calibrated for skull geometries using three different phantoms, the USTUR case 102 phantom, the BfS phantom, and the CSR phantom. To validate these calibrations an international intercomparison with world-wide internal dosimetry reference laboratories was organized, through the European Radiation Dosimetry Group (EURADOS) network. The intercomparison results analysed in the frame of this work, showed an excellent agreement between the HMGU measurements and the other 11 participants of the intercomparison, with relative differences less than 10% for all measurements.

To fully understand the detection efficiency of low energy gammas one of the HMGU PBC detectors was simulated using the GEANT4 Monte Carlo code, and verified by comparison with an identical computational set-up in the MCNPX Monte Carlo code. The experimental results using several point radiation sources were then used to improve the computational detector model and validate it. Finally a computational representation (voxel phantom) of the skull phantom USTUR case 102, previously used for calibration, was implemented in the GEANT4 and the MCNPX codes, and validated through comparison with experimental results.

Using this set-up for the first time all critical body parameters concerning skull measurements were studied systematically using GEANT4, and the following results were obtained.

In a first stage the USTUR phantom was used to analyse the influence of the ^{241}Am activity distribution in the skull surface on the detection efficiency. This revealed changes in the detection efficiency of up to 9% depending on the distance between the detector and the phantom surface.

To study additional critical body parameters that influence the detection efficiency of low-energy gammas, the head of the Max-06 voxel phantom, a computational phantom based on human anatomical cross-sectional images obtained from computed tomography, was implemented in GEANT4. Biokinetic data was then used to study the influence of the activity variation with time in the cortical bone and trabecular bone. The results demonstrated a reduction of the detection efficiency up to 28% depending on the time between the exposure and the measurement.

Another critical parameter is the variable thickness of soft tissue covering the contaminated skull. Through the addition of adipose layers to the Max-06 voxel phantom external surface, the influence of the various scalp thickness values was studied. These calculations showed that for a typical thickness range between 3.6 and 6.0 mm, the detection efficiency changes up to 10%.

Although the head is generally considered to show – in terms of size – a limited inter-individual variability, the results obtained in this work, revealed that the detection efficiency for a small head radius is a factor of 2 larger than that for a big head radius. Using a similar method, the influence of the head shape on the detection efficiency was also studied. However, the results showed that this parameter has only a small influence on the detection efficiency.

These Monte Carlo results were then used to calculate "correction factors" for the detection efficiency as a function of the critical body parameters. These factors were then used to provide "individual-specific" calibrations for two recent cases of human incorporation of ^{241}Am. As a result, estimated incorporated activities are 1.6 and 1.9 times larger than those estimated using the BfS anthropomorphic phantom without applying any correction for person-specific parameters.

Zusammenfassung

[241] Am ist ein Radionuklid von besonderem Interesse, weil es Kalzium in der Knochenstruktur ersetzen kann und weil die bei seinem Zerfall emittierten Alphateilchen ihre Energie über eine kurze Strecke an das umgebende Gewebe wie zum Beispiel das Knochenmark abgeben.

Direkte Messungen mit einem Teilkörperzähler bestehend aus Detektoren, welche außerhalb des Körpers angeordnet sind, stellen ein typisches Verfahren dar, um inkorporiertes [241] Am über den Nachweis von beim Zerfall ebenfalls emittierten 60 keV Photonen zu quantifizieren. Dazu muss eine Kalibrierung des Zählers erfolgen, wobei üblicherweise anthropomorphe Phantome, wie zum Beispiel Schädel- oder Kniephantome, die mit einer bekannten [241]Am Aktivität kontaminiert wurden, verwendet werden. Allerdings können bei der Verwendung derartiger Phantome personenspezifische Parameter (z.B. Schädelform und –größe, Dicke der Kopfhaut) nicht berücksichtigt werden, so dass in-vivo Messungen meist mit großen Unsicherheiten verbunden sind.

Im Rahmen dieser Dissertation wurde daher der am Helmholtz-Zentrum München (HMGU) betriebene Teilkörperzähler (Partial Body Counter - PBC) für eine Schädelgeometrie mit drei verschiedenen Phantomen, einem Schädelphantom des US Transuranium and Uranium Registries (USTUR Case 102), einem des Bundesamts für Strahlenschutz (BfS) und einem des National Radiation Protection Institut (CSR), kalibriert. Der PBC des HMGU ist für den Nachweis von in das menschliche Skelett eingebauten Radionukliden, die beim Zerfall Photonen mit niedriger Energie emittieren, optimiert. Um diese Kalibrierung zu validieren, wurde im Rahmen dieser Dissertation ein internationaler Vergleich organisiert, an dem 11 auf in-vivo Messungen spezialisierte Labore aus Europa und Nordamerika teilnahmen. Ein Vergleich der erzielten Messergebnisse zeigte eine hervorragende Übereinstimmung zwischen den HMGU-Messungen und den Messungen der anderen 11 Teilnehmer dieses Ringvergleiches mit relativen Unterschieden von weniger als 10% für alle Messungen.

Parallel dazu wurde einer der im PBC verwendeten Ge-Detektoren unter Verwendung einer Punktquellen-Geometrie rechnerisch kalibriert. Dazu wurde das am CERN entwickelte Monte-Carlo-Programm GEANT4 verwendet und die Ergebnisse durch einen Vergleich mit Simulationen mit dem Monte-Carlo-Programm MCNPX überprüft. Durch einen Vergleich mit Messungen wurde dann das für die Simulationen verwendete Detektormodell angepasst. Dieses Detektormodell wurde dann verwendet, um mit GEANT4 und einem erstmals implementierten Voxelphantom des USTUR-Schädelphantoms die Kalibrierfaktoren dieses Detektors in Schädelgeomterie rechnerisch zu bestimmen. Die Ergebnisse dieser Rechnungen stimmten sehr gut mit den gemessenen überein.

Damit waren alle Voraussetzungen erfüllt, um den Einfluss von den oben erwähnten kritischen Körperparametern, welche Schädelmessungen betreffen, mit Hilfe von GEANT4 zu untersuchen. Als erster Schritt wurde das USTUR-Schädelphantom verwendet, um den Einfluss der flächenhaften [241]Am-Aktivitätsverteilung im Schädelknochen auf den Nachweis von [241]Am zu untersuchen. Es zeigte sich, dass, je nachdem ob eine homogene [241]Am Verteilung oder eine [241]Am Verteilung entsprechend der, die beim USTUR Fall 102 tatsächlich gemessen wurde, in der Simulation angenommen wurde, die Nachweiseffizienz in Abhängigkeit von dem Abstand zwischen dem Detektor und der Phantomoberfläche sich um bis zu 9% änderte.

Um zusätzliche kritische Körperparameter, welche die Nachweiseffizienz des Detektors beeinflussen, zu untersuchen, wurde der Kopf des sog. Max-06 Voxel-Phantoms, ein auf

Basis menschlicher anatomischer CT-Schnittbilder erstelltes Phantom, in GEANT4 implementiert. Anschließend wurden biokinetische Daten verwendet, um den sich mit der Zeit seit der Inkorporation verändernden Anteil von ^{241}Am in kortikalem und trabekulärem Kochen des Schädels zu untersuchen. Die Ergebnisse zeigten eine Verringerung der Nachweiseffizienz um bis zu 28% in Abhängigkeit von der Zeit zwischen der Aufnahme und der Messung.

Ein weiterer kritischer Parameter ist die variable Dicke der Kopfhaut, die einen Teil der beim Zerfall von ^{241}Am im Schädelknochen emittierten 60 keV Photonen absorbieren kann. Indem in den Simulationen dem Max-06 Voxelphantom Hautschichten unterschiedlicher Dicke hinzugefügt wurden, konnte gezeigt werden, dass sich bei einer typischen Dicke im Bereich zwischen 3.6 und 6.0 mm die Nachweiseffizienz um bis zu 10% ändert.

Obwohl die Kopfgröße eine nur begrenzte interindividuelle Variabilität zeigt, ergaben die in dieser Arbeit erzielten Ergebnisse, dass die Nachweiseffizienz für einen kleinen Kopfradius (81.8 cm) um den Faktor 2 größer ist als die für einen großen Kopfradius (105.5 cm). Ähnliche Untersuchungen, bei denen die Kopfform in den GEANT4-Simulationen variiert wurde, zeigten, dass dieser Parameter nur einen geringen Einfluss auf die Nachweiseffizienz hat.

Diese Monte-Carlo-Ergebnisse wurden dann verwendet, um "Korrekturfaktoren" für die Nachweiseffizienz als Funktion der jeweiligen kritischen Körperparameter zu berechnen.

Diese Faktoren wurden schließlich genutzt, um erstmals eine "individuelle" Kalibrierung des HMGU Teilkörperzählers durchzuführen, die speziell für zwei kürzlich aufgetretene Fälle einer Aufnahme von ^{241}Am angewendet werden sollte. Ein wesentliches Ergebnis dieser Untersuchung war, dass die für diese beiden Inkorporationsfälle die auf der Basis von Teilkörpermessungen geschätzten ^{241}Am-Aktivitäten im Skelett 1.6 und 1.9 mal größer sind als die, die man mit dem BfS Phantom ohne Anwendung der hier entwickelten Korrekturfaktoren erzielt hätte. Dies demonstriert die Wichtigkeit der in dieser Dissertation entwickelten Korrekturverfahren.

1 Introduction

1.1 Motivation

Accidental or occupational exposures to radionuclides can result in the internal contamination of workers and members of the public. In such cases the accurate estimation of the internal contamination is fundamental for occupational legal issues, and in case of large incorporation activity, for determination of the proper medical treatment procedure which will depend on the type of radionuclide incorporated (Cohen, Spitz et al. 1977). For gamma emitting radionuclides the direct *in-vivo* measurement using gamma detectors is the most typical method used, as it allows a rapid determination the radionuclide incorporated. However, since direct measurements are dependent on the measurement geometry, the estimation of any incorporated activity by *in-vivo* methods is dependent on the calibration of the detection system with an anatomical phantom containing a known activity of the radionuclide of interest, so that it simulates the characteristics of an individual (Carinou, Koukouliou et al. 2007).

Due to the morphological variability among individuals, it is necessary to conduct several calibration procedures to better estimate the incorporated activity (Kramer, Burns et al. 2002). These procedures are expensive not only because they require the use of several phantoms, but also because they are a time-consuming processes (Carinou, Koukouliou et al. 2007). These disadvantages make computational methods like Monte Carlo methods very attractive for modelling such systems. Furthermore, the use of Monte Carlo simulations in the calibration of detection systems has already been proven to be a powerful tool, with the advantage of being less expensive, as well as time-saving (Kramer, Burns et al. 2002, Gualdrini, Daffara et al. 2005, Moraleda, Gómez-Ros et al. 2005, Kramer and Hauck 2006). The use of Monte Carlo simulations should not preclude the use of physical calibrations: they are suitable for studying the parameters and better understanding the behaviour of the detection system, as well as extrapolating results to different geometries when the appropriate phantoms are not available (Genicot, Koukouliou et al. 2008).

In this work a dedicated counting system (partial body counter (PBC)) that is available at the Helmholtz Center Munich and that is dedicated to the detection of radionuclides accumulated in the human skeleton such as ^{210}Pb, ^{241}Am and ^{226}Ra emitting low-energy photons; was experimentally calibrated using three physical phantoms of the human head. These calibrations were validated by comparing with several international reference laboratories in the frame of an international intercomparison promoted by the European Radiation Dosimetry Group (EURADOS). In addition using Monte Carlo methods the PBC detection system was simulated and using voxel models from the physical phantoms in the comparison used, the experimental measurements could be reproduced. Finally a realistic anthropomorphic voxel model based on the CT scan of a real human head was implemented in the Monte Carlo simulations and modified so that the impact in the PBC detection efficiency could be studied for individual body parameters such as the scalp thickness and skull size. As a result of these efforts, "individual-specific" calibration factors were obtained, which improve the accuracy on the quantification of the incorporated activity and corresponding internal dose for a particular patient. The individual calibrated of the HMGU PBC was applied for two real contaminated cases involving the accidental incorporation of ^{241}Am.

1.2 *In-vivo* measurement of bone seeking radionuclides

The "bone seeking" radionuclides are of especial concern since they behave chemically similar as calcium and are able to replace it in the bone structure, thus the name "bone seeking". Another aspect is that many of these radionuclides emit alpha particles that will deposit their energy on a short distance resulting on extensive damage to the surrounding tissues.

The measurement techniques for detection of these radionuclides are divided in direct and indirect methods.

- Direct methods use radiation detectors placed external to the human body to measure the activity contained inside the body. As previously mentioned, these measurements require calibration procedures with radioactive calibration sources and anthropomorphic phantoms, simulating the attenuation properties of the monitored individuals (ICRU-69 2003, Carinou, Koukouliou et al. 2007). Based on the measurement geometry direct methods can be split in 3 categories: whole body, partial body and organ counting (ICRU-69 2003). The objective of whole body counting is to determine the complete whole body radionuclide content independently of the radionuclide distribution and is mainly used for photons with energies above 100 keV (ICRU-69 2003). For energies below 100 keV, the photons are considerably attenuated by the human tissues. Thus there is a need of performing measurements in localized regions of the human body. This increases the detection sensibility due to the increase of the solid angle between the source and the detector and due to the reduction of the attenuation caused by the air. There are also cases that, due to the human biokinetics, a radionuclide will concentrate in a defined organ; for both cases partial body and organ counting geometries are typically used.

- Indirect methods measure the activity in the excreta (urine, faeces or sweat), or body fluids (blood or saliva), and use biokinetic models to relate the measured value to the activity present in the body (ICRU-69 2003). Alternatively the indirect methods measure the activity from samples of air or surfaces from the work or accident environment (IAEA 1999).

For both direct and indirect methods, by the use of the appropriate biokinetic models it is possible to determine the incorporation activity which allows estimation of the committed effective dose. The choice of method is mainly dependent on the incorporated radionuclide decay scheme, the limit of detection, the incorporation pathway, the biokinetic behaviour and the time between measurement and intake. For guideline the publications ICRP-78 (1997), IAEA (1999) and ICRU-69 (2003) provide an overview of typical radionuclides, the best method for their measurement and ideal counting geometries for direct methods.

In internal dosimetry there is a high uncertainty due to biokinetic models, since they are based on animal models and limited human data from accidental exposure cases (e.g. USTUR case 102). The improvement of the biokinetic models can be done using *in-vivo* counting. For this the improvement of the direct measurement calibration by the reduction of the uncertainties due to the geometry and individual variations is the key stone.

There are several "bone-seeking" radionuclides of interest such as ^{241}Am, ^{210}Pb, ^{226}Ra and ^{90}Sr-^{90}Y. From these radionuclides ^{241}Am is particularly interesting due to the long physical

half-life (432.6 years), the long biological retention half-life (46.6 years on the skeleton (ICRP-78 1997)), the several contamination cases extensively followed up (Fry 1976, Thompson 1983, Kathren, Lynch et al. 2003, Wernli and Eikenberg 2007, Fojtik, Malatova et al. 2013) and the high intensity (35.92%) emission of a 59.54 keV photon with an that allows it to be detected and assessed by *in-vivo* gamma monitoring of the skeleton.

Due to the low-energy photons emitted by ^{241}Am, the International Commission on Radiation Units (ICRU 2003) recommends that the assessment should be done in a region of the body that is isolated or can be shielded from radioactive emissions from other parts of the body (López, Navarro et al. 2004). The radiation detectors should then be arranged around this region and close to the surface of the region to increase the geometrical efficiency of the detection system. As previously mentioned this type of configuration is called partial body counting.

With this assessment, a proper calibration phantom and an estimation of the fraction of skeleton measured, the total ^{241}Am skeleton content can then be estimated through the method developed by Cohen, Spitz et al. (1977), in which is assumed that the ^{241}Am is uniformly distributed in the mineral mass (bone and teeth), and that for example the head represents 15% of the mineral mass and consequently contains 15% of the ^{241}Am deposited in the skeleton.

There are several suitable measurement sites of the human body that make advantage of the small overlaying soft tissue thickness resulting in a consequent improvement of the detection efficiency: these are the skull, knee, elbow and the wrist. While each of these sites shows advantages and disadvantages, in this work the skull was used for measurements for the following reasons:

- It is possible to reduce the contribution of neighbouring contaminated regions of the human body to the measurement signal by proper shielding (Cohen, Spitz et al. 1977).

- Besides the thyroid gland the concentration of bone seeking radionuclides in the nearby organs and soft tissues is reduced (Cohen, Spitz et al. 1977).

- The skull shows a rather small inter-individual variability (Cohen, Spitz et al. 1977).

- The skull has a relatively big surface therefore this allows the use of several detectors to increase the detection efficiency (Cohen, Spitz et al. 1977, Vrba 2010b).

- The skull represents a reasonable percentage of the total bone in the human skeleton, i.e., between 13.1% and 18.4%, and is covered by only a thin layer of soft tissue (ICRP-23 1975, Cohen, Spitz et al. 1977, Navarro, López et al. 2007).

From the detection system point of view there are also factors that can be decisive in the selection of the measurement site, such as the supporting structure of the detectors and the size of the shielding chamber. Both factors will determine the flexibility, number of detectors that can be used and the measurement geometry.

At the Helmholtz Center Munich the partial body counter includes up to four detectors mounted independently to obtain a high geometrical flexibility. This allows to perform both head and knee measurements. This detection system was previously calibrated for knee

measurements and was, as part of the present work, calibrated for skull measurements with three different anatomical skull phantoms.

1.3 History and state of the art of direct measurements

The first direct measurements were done by Blumgart and Weiss (1927) in the frame of a blood flow study in humans using a ionizing chamber. In this study, these authors have injected ^{226}Ra in volunteer test subjects and were able to detect activities between 5 µg and 100 µg of ^{226}Ra (ICRU-69 2003). In 1937 through the optimization of the Geiger-Müller tube for gamma measurements and by taking in account the body geometry and natural background radiation, Evans was able to make significant improvements in the detection sensibility (Evans 1937, Jackson and Lowe 2002).

The first liquid scintillation Whole Body Counter was unintentionally built by Reines, Schuch et al. (1953) during the development of a shielded liquid scintillation detector for neutrino detection (ICRU-69 2003). This development allowed to further decrease the detection limit through the use of dedicated shielding that reduced the natural radiation background and the use of arrays or large and stationary detectors that increased the sensibility, in contrast to the previously used small and portable detectors. Further improvements were introduced by Sievert and Hultqvist (1957) with the use of high-pressure ionization chambers and the reduction of the background through the installation of the detection system below the ground level, to reduce the cosmic rays background (Jackson and Lowe 2002, ICRU-69 2003).

To this point the detectors used were not able to discriminate the energy measured; this was only achieved in 1957 with the use of new liquid, plastic and sodium scintillators (Jackson and Lowe 2002, ICRU-69 2003). From these detectors the sodium iodine was particularly successful, being still in use today in several reference laboratories mainly, due their relatively big size, low cost and reduced maintenance requirements.

The current state of the art in *in-vivo* counting is the use of semiconductors, mainly germanium crystals. These detectors were introduced in the late 1970's and early 1980's (Toohey, Palmer et al. 1991) and have become a success due to their high energy resolution, which is approximately 10 times higher than that of a sodium iodine detector (Jackson and Lowe 2002).This allowed in some cases, even the discrimination of close energy multiple peaks in gamma spectrum. Another advantage is the higher detection efficiency for high energy gammas due to high atomic number of germanium. However, the germanium detectors have still several critical disadvantages in comparison with those made of sodium iodine: they are more expensive, have a reduced geometrical efficiency due to their small size, and need to be maintained at temperatures around -196 °C through the use of liquid nitrogen or electrical cooling. These detectors are also susceptible to damage during storage time due to detector vacuum degradation.

To determine the activity of a particular radionuclide retained in the body, any of these detection systems need to be calibrated for that radionuclide using an anatomical phantom containing a known activity of the radionuclide. These phantoms have become more and more sophisticated in the last 50 years. The level of detail required for calibration is generally dependent on the portion of the body measured, on the radionuclide emission energy, on the radionuclide emission intensity, and respective detection sensitivity required. The standard phantom used for the calibration of whole body counters is the BOMAB (Bottle Manikin

Absorption), a phantom composed by 10 polyethylene containers, filled with a defined activity of the calibration radionuclide in solution. That together have roughly the size, weight and shape of a standard man (Toohey, Palmer et al. 1991). In contrast, the standard phantom for measurement of transuranic radionuclides in the lung, liver and tracheobronchial lymph is the Lawrence Livermore National Laboratory (LLNL) torso, this phantom provides a detailed representation of the human torso organs, rib cage and different thickness of chess plates of various thicknesses to take in account morphological variability. Additionally this phantom has also exchangeable organs to allow the loading with different radionuclides (Griffith, Anderson et al. 1978).

Besides the previous examples there are several other commercially available phantoms. For whole body counters there are: the St Petersburg brick phantom that is composed by small polyethylene bricks loaded with small rods containing the radionuclide of interest (Kovtun, Firsanov et al. 2000); the bottle phantom which consists of simple half litre and one litre or one litre and two litres bottles loaded with the calibration radionuclide in solution and put together to represent the reference man or a specific person dimensions (Carinou, Koukouliou et al. 2007); the Emma phantom designed to replace the BOMAB phantom which is composed of cylinders, cuboids and elliptical cylinders with holes to allow it to be loaded with rods including the radionuclide of interest (Lebacq, Bruggeman et al. 2011); the RMC-II phantom, developed by Canberra/RMC is made of several Perspex plaques and according to the manufacturer able to reproduce the total body calibration coefficients from a BOMAB phantom (Nogueira, Silva et al. 2009).
For partial body counters the most known commercial phantoms besides the LLNL are: the Japan Atomic Energy Research Institute (JAERI) torso phantom, a lung phantom similar to the LLNL phantom, but representing the Asian average man (Shirotani 1988); the Spitz knee phantom built for knee measurements of bone seeking radionuclides, is a solid plaster of a human knee that contains tissue equivalent material used for femur, patella, tibia, and fibula, all them exchangeable to allow the use of different radionuclides (Spitz and Lodwick 2000).

The construction of these phantoms is not only expensive and time consuming but there are several cases where a commercial phantom is not available, as in the case of skull phantoms for bone seeking radionuclides. The majority of the skull phantoms produced until now are derived from real human skull bones artificially contaminated and then filled and covered with tissue equivalent material. Currently the group with most experience in their construction is the Laboratory for Radiation Studies from New York Medical Center's Institute of Environmental Medicine, USA. This group has also taken part on the construction of the USTUR case 102 phantom (Hickman and Cohen 1988).

There are currently nine skull phantoms for ^{241}Am incorporation in the human bone available world-wide, three of them were used in the present work: 1) the USTUR case 102 phantom which is a unique phantom that contains the skeleton bones of an individual who was by accident internally contaminated with ^{241}Am and who donated his body for research, produced by New York Medical Center's (Hickman and Cohen 1988); 2) the BfS skull phantom, produced by New York Medical Center's (Laurer 1993); 3) the CSR skull Phantom, a half sphere that corresponds to the head's top, represents a totally artificial phantom, this phantom was produced by a collaboration between the National Radiation Protection Institute (NRPI, Czech Republic) and the Slovak Medical University (SZU, Slovak Republic) (Fojtik 2011).
The other skull phantoms available are: the UCIN phantom, built in 1994 at the University of Cincinnati, contains ^{241}Am and ^{152}Eu (Kellar 1995, Spitz and Lodwick 2000); the NRPI phantom, a real human skull without soft tissues that uses a point source shifted over the skull surfaces and a mathematical correction to take in account the soft tissue attenuation (Malátová

and Foltánová 2000); the Alderson ENEA skull phantom, a commercial phantom for angiographic analysis calibration modified by the addition of 24 disk like sources with ^{241}Am, at the Ente Nazionale per le Nuove Tecnologie (ENEA, Italy) (Gualdrini, Battisti et al. 2000); the artificial Cohen head phantom, produced by the New York Medical Center's (López, Navarro et al. 2004); the KIT skull phantom produced, in the 1980's with a real human skull, for which no information is available on is construction (Hegenbart and Schwabendand 2011); and the HPA skull phantom, produced by David P Hickman for his PhD thesis, under the supervision of Norman Cohen, at New York University Medical Center (Hickman 1987/8).

The problem of all these skull phantoms is that they are unique in terms of their dimensions, attenuation characteristics, and not exactly reproducible. In addition, all have some limitations or even defects in their design and construction.

Currently the use of physical phantoms is being replaced by the use of numerical calibrations using Monte Carlo methods and computational phantoms, thanks to the increase of computational power and reduction of the computer costs. The current computational power allows to use Monte Carlo simulations of very complex detector models and surroundings (patient chair or bed, counting chamber, detectors supporting structure, *etc...*) in any recent desktop computer. An example is the modelling of the Karlsruhe Institute of Technology (KIT) detection system and complete counting chamber (Hegenbart 2009, Marzocchi 2011, Pölz 2014). This evolution of computational power can also be seen in the increase of detail of the computational phantoms. The first anthropomorphic computational phantoms described the human body and organs shape using simple mathematical shapes, nowadays the state of the art phantoms are built with anatomical cross-sectional images obtained from computational tomography, magnetic resonance imaging or photographs from cryosection cadavers, thus allowing to describe all anatomical features with great detail.

Anthropomorphic voxel models, due to their great detail, are in most of the cases closer to the person characteristics than the physical phantoms, and thus consequently allow increasing the accuracy of the calibration of the detection system. These models have also the advantage to be flexible in terms of their dimensions, composition and shape. This flexibility allows the user to easily adjust the phantom to the measured subject characteristics such as size, mass and shape, thus increasing the accuracy of the quantification of the incorporated activity.

The goal of the present work is to use Monte Carlo methods and the voxel phantoms flexibility to study the influence of critical body parameters in the detection efficiency and calculate "individual-specific" calibration factors for the PBC detection system.

2 Partial Body Counter Measurements

2.1 Description of Partial Body Counter used

The partial body counter at HMGU is composed of four high purity germanium detectors mounted independently in four supporting that provide highly flexible measurement geometries, see Figure 2.1. The design of all detectors was optimized for the measurement of low gamma energies: the detectors' crystal dimensions are characterized by a big diameter and a small thickness which reduces the detection efficiency for high energies and also reduces the background contribution resulting from the Compton scattering from ^{40}K that is naturally present in the human body. Also the construction materials used have a low radioisotope content, and in addition all detectors have an especially long necktube (connection between the dewar and the end cap), in order to reduce the background contribution from the dewar and preamplifier materials.

2.1.1 Detectors

Detector 2 and 3 are identical and were manufactured by Eurisys Canberra. Each detector comprises an n-type planar germanium crystal, with the nominal dimensions of 50 mm diameter and 10 mm thickness. These crystals are mounted within an aluminium cup in a planar configuration and are enclosed by an aluminium end cap with a 1.1 mm thick carbon fiber window. The front edge of the crystals has been rounded to remove weak field regions (bulletization) thus resulting in a 2.5 mm radius bevel.

Detector 4 was manufactured by Canberra and comprises an n-type planar germanium crystal, with the nominal dimensions of 81 mm diameter and 22 mm thickness. This crystal is mounted within a copper cup in a planar configuration and is enclosed by an aluminium end cap with a 0.5 mm thick carbon epoxy window. The front edge of the crystal has not been bulletized.

Detector 6 was manufactured by EG&G Ortec and comprises an n-type close-ended coaxial germanium crystal, with the nominal dimensions of 70.7 mm diameter and 29.5 mm thickness. This crystal is mounted within a copper cup in a coaxial configuration and is enclosed by an aluminium end cap with a 0.76 mm thick carbon fiber window. The front edge of the crystal has been bulletized thus resulting in an 8 mm radius bevel.

The signals of detector's 2, 3 and 4 are amplified by a Canberra AFT Research Amplifier (model 2025), while the signal of detector 6 signal is amplified by a DSPEC from ORTEC. Acquisition and analysis of spectral data was done for each detector separately using the EG&G ORTEC Gamma Vision gamma-ray spectrum analysis software and Multi-Channel Analyser emulation (version 5.33).

Figure 2.1: Partial body counter germanium detectors in skull measurement geometry configuration, on the right detector 2, on the left detector 3, in the middle detector 4, on the top detector 6.

2.1.2 Counting chamber

The counting chamber walls and roof are composed of a graded shielding with 140 mm old steel, 4 mm lead and 2 mm copper. This provides not only the reduction of external natural background, but the graded set of materials also reduces the fluorescent x-ray escape peaks that can be produced from photoelectric absorption of gamma rays by the shielding (Gilmore 2008). The entrance to this chamber is labyrinth shaped and composed of 140 mm old steel walls and roof. The chamber dimensions are 3 m $\times$ 1.5 m $\times$ 2.1 m. It is located in a room 8 m below the surface of the Earth, in order to reduce the natural comic ray background.
Additional precautions are taken in order to avoid the contamination of the room by ^{137}Cs from the Chernobyl fallout and a set of filters is used in the ventilation system to reduce the presence of radon in the air.

To estimate the reduction of the natural background by the shielding two background measurements were performed: one inside the counting chamber and the second out-side the counting chamber but in the same room at 8 meters depth both for a measurement time of 50000 s. By comparing the total count rate between the different spectra it was concluded that the shielding results in reduction of the natural background by a factor of 60, in the energy range from 10 keV to 100 keV and from 10 keV to 2000 keV, however, at 60 keV there is a reduction factor of 75. All these values are less than the 110 factor obtained by a similar shielding chamber at KIT (Marzocchi 2011). However, since background measurements out-side the counting chamber were also performed at a 8 meters depth the factor obtained it does not reflect the reduction of the cosmic rays that is responsible for 40% of a typical natural

background at the surface of the earth (Gilmore 2008). The remain "typical contributors in a typical detector, with no extraordinary precaution might be the detector materials (10%), construction materials (40%) and radon in the air (10%)" (Gilmore 2008).

In Figure 2.2 one can see that the natural background outside the chamber is significantly higher than that inside the chamber, in terms of counting rate, number of peaks observable and the Compton continuum, which is due to natural background radionuclides in building construction materials and possibly also due to the additional contribution from cosmic-rays charged particles such as the Muons. The main peaks were identified and are presented in Table 2.1.
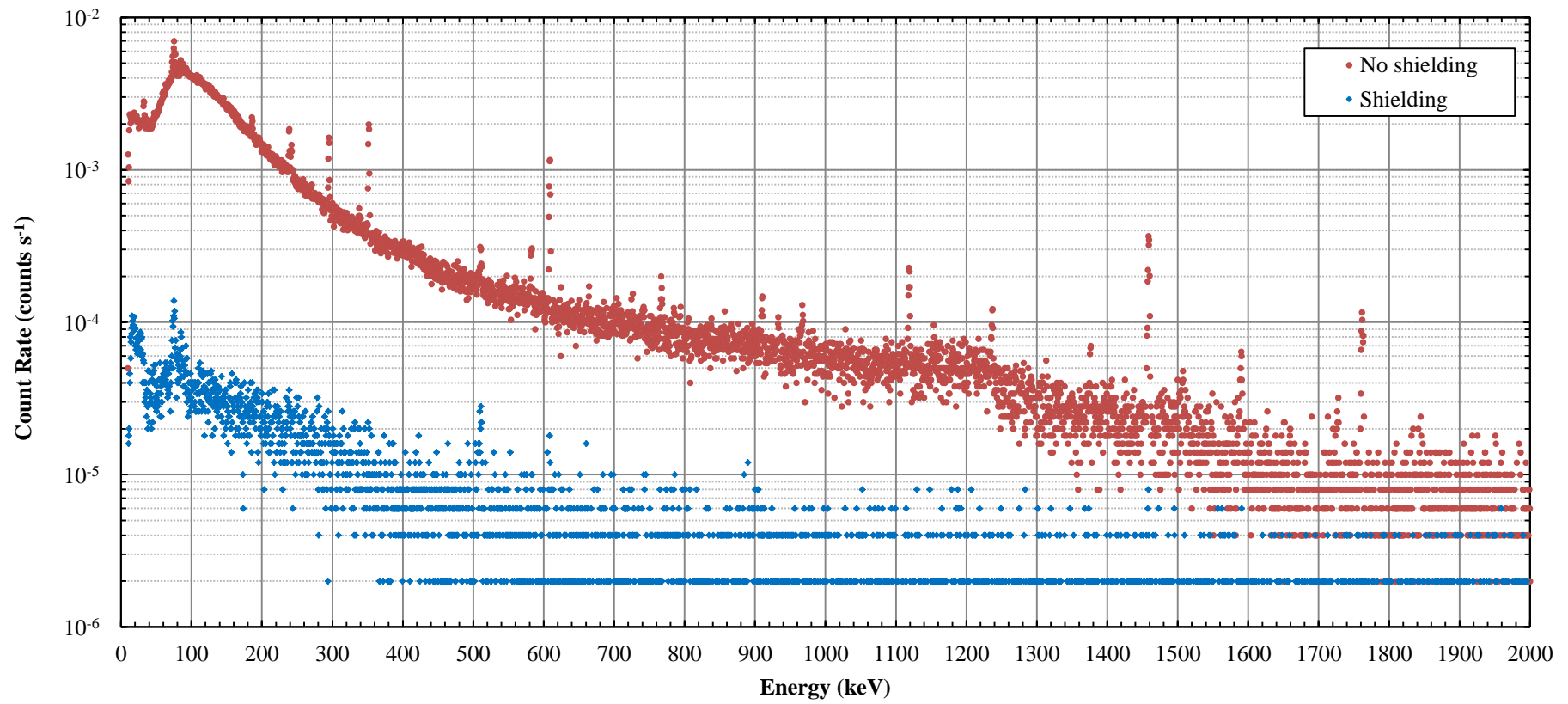
Figure 2.2: Detector 3 measurement of the natural background inside and outside of the counting chamber, for a 50000s measurement time.

Table 2.1: Nuclides identified using HMGU detector 3 in a 50000 measurement of the natural background, values are based on Gilmore (2008) and ICRU-69 (2003).

Energy (keV)	Nuclide	Source
31.81	^{137}Cs Kα_2 flourescence	Fission
32.19	^{137}Cs Kα_1 flourescence	Fission
36.45	^{137}Cs Kβ_1 flourescence	Fission
37.33	^{137}Cs Kβ_2 flourescence	Fission
46.54	^{210}Pb	^{238}U series, lead
72.81	Pb Kα_2 flourescence	Lead shielding
74.82	Bi Kα_2 flourescence	^{238}U series, radon progeny
77.11	Bi Kα_1 flourescence	^{238}U series, radon progeny
84.94	Pb Kβ_1 flourescence	Lead shielding
89.8	Bi Kβ_2 flourescence	^{238}U series, radon progeny
92.58	^{234}Th	^{238}U series - doublet
186.21	^{226}Ra	^{238}U series
238.63	^{212}Pb	^{232}Th series
242.00	^{214}Pb	^{238}U series, radon progeny
295.22	^{214}Pb	^{238}U series, radon progeny
351.93	^{214}Pb	^{238}U series, radon progeny
511.00	Annihalation	Cosmic radiation, high energy gamma emitters
583.19	^{208}Tl	^{232}Th series, thoron progeny
609.31	^{214}Bi	^{238}U series, radon progeny
661.66	^{137}Cs	Fission
768.36	^{214}Bi	^{238}U series, radon progeny
911.20	^{228}Ac	^{232}Th series
934.06	^{214}Bi	^{238}U series
968.97	^{228}Ac	^{232}Th series
1120.29	^{214}Bi	^{238}U series, radon progeny
1238.11	^{214}Bi	^{238}U series, radon progeny
1377.70	^{214}Bi	^{238}U series, radon progeny
1460.82	^{40}K	Primordial
1588.20	^{228}Ac	^{232}Th series
1729.60	^{214}Bi	^{238}U series, radon progeny
1764.49	^{214}Bi	^{238}U series, radon progeny

2.2 Calibration phantoms

2.2.1 USTUR case 102

The United States Transuranium and Uranium Registries (USTUR, U.S.A) case 102 phantom represents a whole body phantom with movable parts, containing a human skeleton with a natural metabolic ^{241}Am activity incorporation in the bone matrix. The skeleton belonged to a doctoral student who was accidently exposed by internal ^{241}Am contamination between 1952 and 1954, possibly during the handling of an unsealed ^{241}Am source (no information concerning the chemical compound available). The contamination was only found in 1958 at the occasion of a urinary excretion measurement. It is believed that the primary contamination was through a wound in his left hand, based on postmortem analyses. The total ^{241}Am uptake was between 7400 Bq and 40700 Bq, depending on the models and calibration factors used. No chelation therapy was applied to reduce the ^{241}Am activity incorporated (Breitenstein, Newton et al. 1985).

In 1979 case 102 became the first whole-body donation to the USTUR (Breitenstein, Newton et al. 1985). The cause of death was a metastatic malignant melanoma which involved all the soft tissues and organs (Breitenstein, Newton et al. 1985).

Gamma spectrometry revealed a symmetrical distribution between the left and right side of the body, and using a method developed by Cohen, Spitz et al. (1977) to estimate the total ^{241}Am skeleton content from *in-vivo* measurements in the head, good agreement between the gamma measurements and radiochemistry results, 3700 Bq and 4406.7 Bq, respectively, was found (Breitenstein, Newton et al. 1985, Palmer, Spitz et al. 1985).

Postmortem the skeleton was sagittaly divided and the left side was analyzed with radiochemical techniques. The previous weighted results together with radiochemical analyses of the soft tissues revealed a total activity of 5.4 kBq of ^{241}Am, distributed as follows: 80% in bones and teeth; 6.3% in liver; 1.9% in soft tissues of the left hand; 1.5% in respiratory track tissues; 0.9% in other organs, and 8.6% in structural soft tissues (Breitenstein, Newton et al. 1985). This data together with the weights of bones was then used to develop a new biokinetic model for the ^{241}Am metabolism, which in 1979 became a reference for the ICRP (Breitenstein, Newton et al. 1985).

The right side of the skeleton was used to build calibration phantoms for skull, torso, arm and leg for *in-vivo* counting systems (Hickman and Cohen 1988). To obtain a complete human skull phantom the USTUR case 102 half skull was paired with a non-contaminated half skull, see Figure 2.3. Both parts were attached and tissue-equivalent spacers were placed on the outside surface of the skull in order to provide a realistic variation of the thickness of soft tissue covering the human skull. The two parts were placed inside of a head cast, previously constructed with the help of a volunteer subject, and finally this cast was then filled with tissue equivalent material (Hickman and Cohen 1988).

Figure 2.3: Construction of USTUR case 102 skull phantom, on the left case 102 half skull on the right non-contaminated half skull (Hickman and Cohen 1988).

During the construction of the USTUR skull phantom extensive measurements (117) were performed to the case 102 bone surface, using a small 25 mm diameter NaI(Ti) and a small lead shielding, so that only the bone surface in direct contact with the detector would be measured, see Figure 2.4 (Hickman and Cohen 1988). These "shadow shielding configuration" measurements allowed Hickman and Cohen to create a map of the counts per minute corresponding to the activity distribution pattern in the skull bone surface, see Figure 2.5.
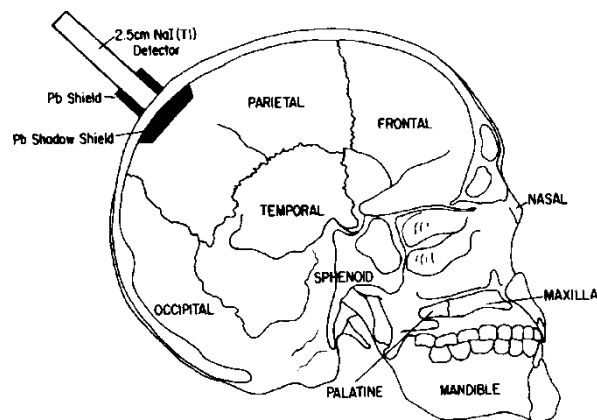
Figure 2.4: "Shadow shielding configuration" measurements on case 102 half skull surface (Hickman and Cohen 1988).
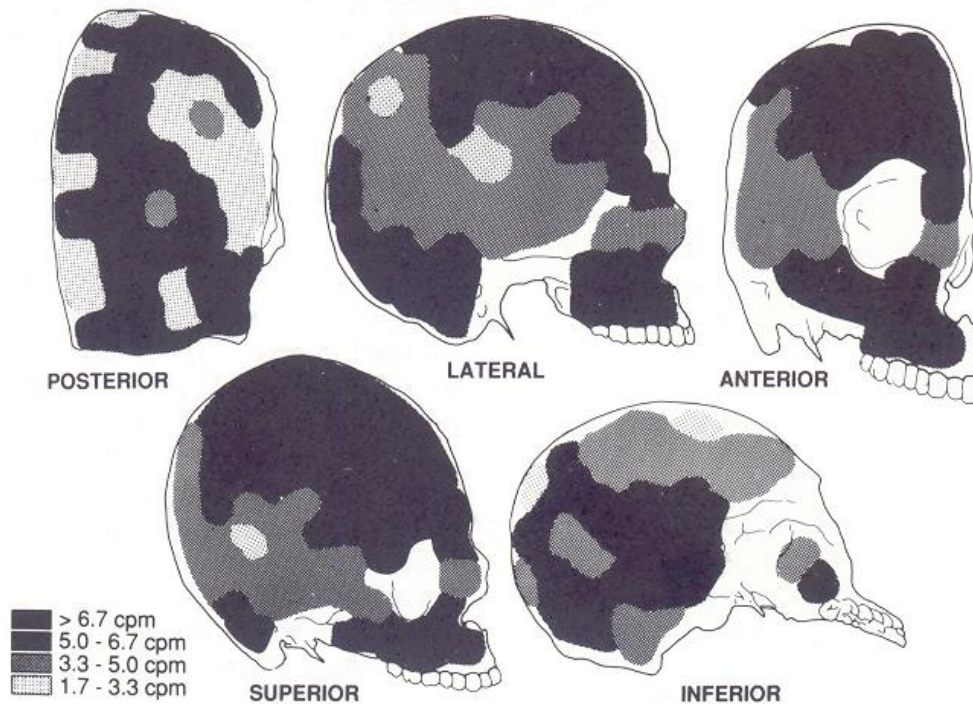
Figure 2.5: Activity distribution pattern measured in USTUR case 102 half skull by Hickman and Cohen (1988).

The radiochemical analyses performed to the left side of case 102 confirmed the existence of different activities in some of the skull bones, and as in the gamma spectrometry the highest activities were found in the facial regions, maxilla and frontal bones (McInroy, Boyd et al. 1985). Unfortunately the radiochemical results are given in terms of bones, and as a consequence it's not possible to directly compare them with the "shadow shielding" measurements, since the bone analyses will result in an averaging of the ^{241}Am distribution. This averaging explains why the difference between the parietal bone and temporal bone is inferior in the radiochemical analyses when compared with the shadow shielding measurements.

At the time of phantom construction Hickman and Cohen used a partial body counter composed of three 150 mm diameter phoswich detectors which they used for the skull measurement; the measured activity distribution, although a "particularly higher activity measured in the facial regions" was observed, was considered reasonably homogeneous for typical counting geometries (Hickman and Cohen 1988). Nowadays these types of measurements are typically performed with germanium detectors, which due to manufacture limitations have a somewhat smaller diameter, (i.e., between 50 mm and 80 mm). The influence of any activity distribution pattern in the detection efficiency for a germanium detector was studied in this work using Monte Carlo methods and the USTUR case 102 voxel phantom, see Chapter 6.

In summary the USTUR case 102 human skull phantom consists of ^{241}Am contaminated skull bones on the right side, which was completed with non-contaminated skull bones on the left side. The total skull was filled and covered with tissue-equivalent material (Hickman and Cohen 1988). A recent re-evaluation of the activity content indicates that this skull phantom contains 287.2 Bq ± 3.7 Bq of ^{241}Am at the reference date 2012-1-1 (Tolmachev 2012).

2.2.2 BfS Phantom

The BfS phantom is a skull phantom with human bone artificially contaminated with [241]Am. It was produced by the New York Medical Center, for the Federal Office of Radiation Protection (BfS, Germany).
The inside of the phantom is filled with small spheroids of soft-tissue-equivalent wax and the outside is covered with a layer of soft-tissue-equivalent wax with a constant thickness that corresponds to the average thickness of soft tissue covering the human skull of an average person (Laurer 1993). The activity was artificially put on the bone surfaces as follows: small rectangular pieces of absorbent paper filter were impregnated, via calibrated syringe, with a known amount of [241]Am solution (Laurer 1993). These activated filter papers were distributed in the bone surface as following: 3000 Bq on the outside bone surface and 2400 in the inside bone surface, resulting in a total activity of 5400 Bq $\pm$ 113.4 Bq at the reference date 1993 March 1 (Laurer 1993).

2.2.3 CSR Phantom

The CSR skull phantom is a completely artificial phantom that represents the top of a human head. This phantom is the product of a collaboration between the National Radiation Protection Institute (NRPI, Czech Republic) and the Slovak Medical University Bratislava (SZU, Slovak Republic). The bone is made of gauze and gypsum and the soft tissue of elastic polyurethane GAFORM E45. It contains 981.4 Bq $\pm$ 9.8 Bq of [241]Am at the reference date 2012-1-1, that was implanted in the gauze and gypsum in the form of drops, distributed in 418 nodes of a square net, 228 drops outside and 192 drops inside (Fojtik 2011, Vrba, Malátová et al. 2013).
Due to the geometry and shape of this phantom, only one position corresponding to the top centre of the phantom was defined for measurement.

Figure 2.6: Head phantoms used for the HMGU PBC calibration: USTUR case 102 phantom, CSR phantom and BfS phantom, from left to right.

Table 2.2: Summarization of the most important size parameters of the skull. Definition of the parameters X, Y, and Z are given in Chapter 6. NA means not applicable.

	Phantom		
Dimensions	BPAM	BfS	CSR
Skull mass (kg)	0.66	[a]0.56	NA
Perimeter (mm), over the forehead and back of the head	620	480	520
Perimeter (mm), over the top of the head and under the chin	655	485	NA
Half perimeter, top of one ear to the other one (mm)	320	265	222
Half perimeter, forehead to the back of the neck (mm)	605	355	NA
X – Head width (mm)	175	129	165
Y – Head length (mm)	208	174	161
Z – Chin to top of the head (mm)	228	186	NA

[a] − Estimation from Truckenbrodt, Rühm et al. (1999).

2.3 Minimum Detectable Activity MDA

Measurements of low activities incorporated by the human body present several challenging aspects. One of them is the need to distinguish between the measured counts resulting from an incorporated radionuclide and counts resulting from random statistical fluctuations of the natural background. For this several counting decision limits were developed, the so called decision limits. They are derived from statistical hypotheses and have been developed since more than 50 years; despite this their definition is still subject of discussion between laboratories (Lee, Jung et al. 2008). State of the art methods for the calculation of limits use Bayesian statistics. However, since their use is still matter of discussion, in this work the limits are calculated according to the currently most accept method that is based on the work of Currie (1968) and the International Organization for Standardization (ISO) ANSI N13.30 (1996).

There are five decision limits: the critical limit (L_C), the upper limit (L_U), the determination limit (L_Q), the detection limit (L_D) and the minimum detectable activity (MDA) (Gilmore 2008). From this the MDA is the most important, it can be better understood as the "minimum activity that we can be confident that we can detect" and is derived from the L_D which "is the minimum number of counts that one can be confident of detecting given a specific uncertainty " (Gilmore 2008).

The MDA is dependent on the measurement geometry, energy of interest, radionuclide source distribution, detection system efficiency, natural background and measurement time (Debertin and Helmer 1988). It can be calculated following the methods developed by Currie (1968) and ANSI N13.30 (1996) where it is defined for a 95% confidence level as:

$$MDA = \frac{L_D}{T\varepsilon\gamma} \ , \qquad L_D = 3 + 4.65 s_b \qquad\qquad 2.1$$

where s_b is the standard deviation of the number of counts for repeated measurements of a
blank, in the same region of the full energy peak FHWM,

T is the measurement time in seconds,

ε is the full energy peak efficiency (the number of counts measured divided by the
source activity the gamma emission probability and measurement time), and

γ is the emission probability of the gamma of interest (Bento, Silva et al. 2010).

The MDA for a detection system is not a straightforward definition, since it can vary
depending on choices made for its calculation: the phantom used, because different phantoms
can have different activity distributions; on the blank definition, since this can be a non-
contaminated person or a non-contaminated phantom (Bento, Silva et al. 2010).

In this work the MDA for ^{241}Am 59.54 full energy peak efficiency was determined for two
skull phantoms: the USTUR Case 102 skull phantom and the BfS phantom, and the 3
detectors configuration used in Chapter 7, see Table 2.4 and Table 2.5. The values used for
the MDA calculation are shown in Table 2.3. To obtain the background three persons
measurements were used, made on two white males and one female, see Table 2.3.

Table 2.3: Photon energy, respective probability emission, detectors FWHM and background
counts in the same region of the full energy peak FHWM for the average of three non-
contaminated persons measurements.

^{241}Am	Detector							
	2	Uncer.	3	Uncer.	4	Uncer.	6	Uncer.
E (keV)	59.54		59.54		59.54		59.54	
p (%)	35.92	0.17	35.92	0.17	35.92	0.17	35.92	0.17
FWHM (channel)	3		3		3		3	
Background (cps)($\cdot 10^{-3}$)	6.00	2.45	5.83	1.80	12.8	2.7	19.2	3.7

The MDA values obtained for detector 3 using the BfS phantom are similar to the MDA
values previously calculated by Rühm, Truckenbrodt et al. (1997) for a similar detector, in
terms of crystal size and detection efficiency, of the BfS partial body counter and also using
the BfS skull phantom.

Table 2.4: MDA calculated for ^{241}Am (59.54 keV) using USTUR case 102 skull phantom, the blank is an average of 3 persons, a 7200 s measurement time, and the three detectors measurement geometry described in Chapter 7.

USTUR phantom	Single detector								3 detectors configuration			
Time 7200 s	2	Uncer.	3*	Uncer.	4	Uncer.	6	Uncer.	2 - 3 - 4	Uncer.	3 - 4 - 6	Uncer.
Efficiency	$3.17 \cdot 10^{-3}$	$7.85 \cdot 10^{-5}$	$3.31 \cdot 10^{-3}$	$6.91 \cdot 10^{-5}$	$1.19 \cdot 10^{-2}$	$2.06 \cdot 10^{-4}$	$5.46 \cdot 10^{-3}$	$8.17 \cdot 10^{-5}$	$1.83 \cdot 10^{-2}$	$2.31 \cdot 10^{-4}$	$2.06 \cdot 10^{-2}$	$2.32 \cdot 10^{-4}$
L_D (counts)	33.56	6.85	33.14	5.11	47.60	4.96	57.63	4.91	64.90	5.33	79.69	4.83
MDA (Bq)	4.09	1.06	3.87	0.82	1.55	0.26	4.08	0.61	1.37	0.19	1.49	0.18

* - Detector 3 efficiency values corrected for complete contaminated skull, see Chapter 3.

Table 2.5: MDA calculated for ^{241}Am (59.54 keV) using the BfS skull phantom, the blank is an average of 3 persons, a 7200 s measurement time, and the three detectors measurement geometry described in Chapter 7.

BfS phantom	Single detector								3 detectors configuration			
Time 7200 s	2	Uncer.	3	Uncer.	4	Uncer.	6	Uncer.	2 – 3 - 4	Uncer.	3 - 4 - 6	Uncer.
Efficiency	$6.53 \cdot 10^{-3}$	$1.6 \cdot 10^{-4}$	$9.06 \cdot 10^{-3}$	$2.2 \cdot 10^{-4}$	$2.36 \cdot 10^{-2}$	$5.5 \cdot 10^{-4}$	-	-	$3.92 \cdot 10^{-2}$	$6.1 \cdot 10^{-4}$	-	-
L_D (counts)	33.56	6.85	33.14	5.11	47.60	4.96	57.63	4.91	64.90	5.33	-	-
MDA (Bq)	1.99	0.51	1.41	0.31	0.78	0.14	-	-	0.64	0.10	-	-

3 EURADOS Measurements Intercomparison

3.1 Motivation

The European Radiation Dosimetry Group (EURADOS) is a non-governmental European organization of institutions involved in the field of the dosimetry of ionizing radiation. This network is divided in working groups. EURADOS Work Group 7 (WG7) is acting as a network in the field of Internal Dosimetry for scientists, services, regulators, and laboratories whose main aims are harmonization, coordination of research, training, and dissemination of scientific knowledge in the field of assessments of internal exposures due to intakes of radionuclides (Lopez 2012). In the WG7 frame there have been in the past two intercomparison exercises; one used the USTUR case 102 leg phantom and a Spitz knee phantom (Lopez, Broggio et al. 2011) and was complemented in respect to Monte Carlo calculations by José M. Gómez-Ros (Gómez-Ros, de Carlan et al. 2008), while the other intercomparison was done using a Lawrence Livermore torso phantom and was coordinated by David Broggio (Broggio, Bento et al. 2012). Both intercomparison exercises were the result of a successfully join effort between EURADOS WG7 and WG6 (computational dosimetry).

In the EURADOS Annual meeting 2011 held in Prague the EURADOS WG7 task 4 proposed a new intercomparison exercise focused on the calibration of partial body counters for human skull measurements. This is the first EURADOS intercomparison for skull counting geometries, although, it is not the first international intercomparison of the kind performed, Rühm, König et al. (1998) conducted the first partial and whole body counting intercomparison, having, five laboratories as participants . In that exercise the main goal was to compare the values obtained for the assessment of the skeleton burden of a male subject that had incorporated ^{241}Am in the early 1970's. The intercomparison results obtained showed differences up to 60% between different laboratory assessments, partially due to the use of different phantoms for calibration and because measurement were carried out at different positions.

The current EURADOS skull measurements intercomparison is being coordinated by Pedro Nogueira, and the main motivations are the assessment of the measurements reproducibility between different laboratories; to provide to the participant's with the means to perform their detection system calibration for skull counting geometries, (note that before this intercomparison only 6 participating laboratories had calibrations for this geometry); to compare the assessment of the phantoms activity; to assess the number and capabilities of the partial body counters available in the frame of the EURADOS network; and to promote the use of Monte Carlo tools for calibration purposes. Three phantoms were considered for this intercomparison: the USTUR case 102 skull phantom, the BfS phantom, and the CSR Phantom, all previously described in Chapter 2. A detailed measurement protocol was provided and the measurements positions were marked in the phantoms.

Regular meetings of the WG7 held every 6 moth helped to organize, coordinate, disseminate and clarify questions from the participants. At one of these meetings it was decided to divide the intercomparison in two parts: one focused on the physical calibration of partial body bounters participating, the other dealing with the use of Monte Carlo simulations for calibration purposes. The results relative to the first task will be analysed and used in the present thesis to validate the HMGU PBC measurements.

3.2 HMGU results validation

Regarding the measurement intercomparison there were originally 14 participants: 11 from Europe – Helmholtz Centre Munich (HMGU), Federal Office for Radiation Protection (BfS), Karlsruhe Institute for Technology (KIT), National Radiation Protection Institute (NRPI), Slovak Medical University (SZU), Belgian Nuclear Research Centre (SCK·CEN), Institute for Radiological Protection and Nuclear Safety (IRSN), Centre for Energy, Environment and Technology Investigations (CIEMAT), Health Protection Agency now called Public Health England (PHE), Finnish Radiation and Nuclear Safety Authority (STUK), National Centre for Nuclear Research (NCBJ); 2 from North America – the Pacific Northwest National Laboratory (PNNL), Health Canada (HC) and 1 from Asia – the China Institute for Radiation Protection (CIRP). Unfortunately, due to the complexity of the bureaucratic process of the phantom transport to China and the risk of damage to the phantoms due to the phantoms transport at the summer season where temperatures can arise to 50 °C in the Beijing area, the CIRP was forced to quit from their participation in the measurements. SZU didn't provide results in time for the task one of the intercomparison. Because of this both the CIRP and SZU partial body counters will not be discussed in this work.

Despite the fact that most of the detectors were built by only two firms all PBC's are quite different in terms of their number of detectors, detector characteristics, main purpose, flexibility and dedicated shielding, see Figure 3.1. In Table 3.1 the PBC main characteristics are described.

Figure 3.1: Three of the partial body counters that have participated in the EURADOS intercomparison belonging to the HC, the NRPI and SCK·CEN, from left to right respectively.

Table 3.1: Partial body counters details from EURADOS Intercomparison participants that have delivered results for task 1.

Institute	Detector Number	Type	Manufacturer	Germanium Crystal Active area (mm²)	Diameter (mm)	Length (mm)	Window Material	Thickness (mm)	Used typically in the energy range (keV)	Spectrum Analyses software
SCK CEN	2	LEGE	Canberra	2922	61	20	carbon epoxy	0.5	25 - 400	Genie 2000 v3.2.1
PNNL	2	HPGe	Canberra	3848	70	20	carbon fiber	0.6	17 - 200	Abacos Plus v5.3
				3848	70	30	carbon fiber	0.6		
BfS	4	HPGe	Canberra	2003	50.5	20	carbon epoxy	0.5	15 - 1750	LVis v2.1.0.5
IRSN	2	BEGe	Canberra	5027	80	30	carbon epoxy	1.6	13 - 2000	Genie 2000 v3.1a
CIEMAT	4	LEGe	Canberra	3848	70	25	carbon epoxy	0.5	20 - 1000	Abacos/Genie 2000 v1.2
HC	4	GEM	Ortec	5675	85	30	carbon fiber	0.76	10 - 500	Ortec Renaissance v4.01
KIT	4	XtRa	Canberra	4418	75	72	carbon fiber	0.5	40 - 200	Genie 2000 v3.2
NRPI	4	LO-AX	Ortec	3848	70	30	carbon fiber	0.76	14 - 200	Genie 2000 v3.2
		LO-AX	Ortec	3848	70	30	beryllium	0.5		
		BEGe	Canberra	3848	70	25	carbon fiber	0.6		
		GEM-FX	Ortec	3848	70	27.6	carbon fiber	0.9		
PHE	4	GEM-FX	Ortec	3848	70	25	carbon fiber	0.76	15 - 1000	Genie 2000 v3.2.1
STUK	3	BEGe	Canberra	4418	75	20	carbon epoxy	Unknown	20 - 2000	STUK dedicated software
NCBJ	1	GX-4018	Canberra Packard	4536	76	Unknown	carbon fiber	0.6	40 - 2000	Genie 2000 v3.1a
HMGU	4	EGM2000	Eurisys Canberra	1963	50	10	carbon fiber	1.1	20 - 200	Gamma Vision v5.33
		EGM2000	Eurisys Canberra	1963	50	10	carbon fiber	1.1		
		Be5020	Canberra	5153	81	22	carbon epoxy	0.5		
		LOAX	EG&G Ortec	3926	70.7	29.5	carbon fiber	0.76		

The following travelling route was used taking into account the most effective way in terms of distance and global costs to transport the phantoms:

HMGU (Germany) → BfS (Germany) → KIT (Germany) → NRPI (Check Republic) → SZU (Slovakia) → SCK·CEN (Belgium) → IRSN (France) → CIEMAT (Spain) → HPA (United Kingdom) → STUK (Finland) → HMGU (Germany) → HC (Canada) → PNNL (United States of America) → National Centre for Nuclear Research (Poland), see Figure 3.2.

Transport costs were shared between the laboratories. Each participant had 3 weeks to perform the measurements and then the results were sent to and compiled by Pedro Nogueira.
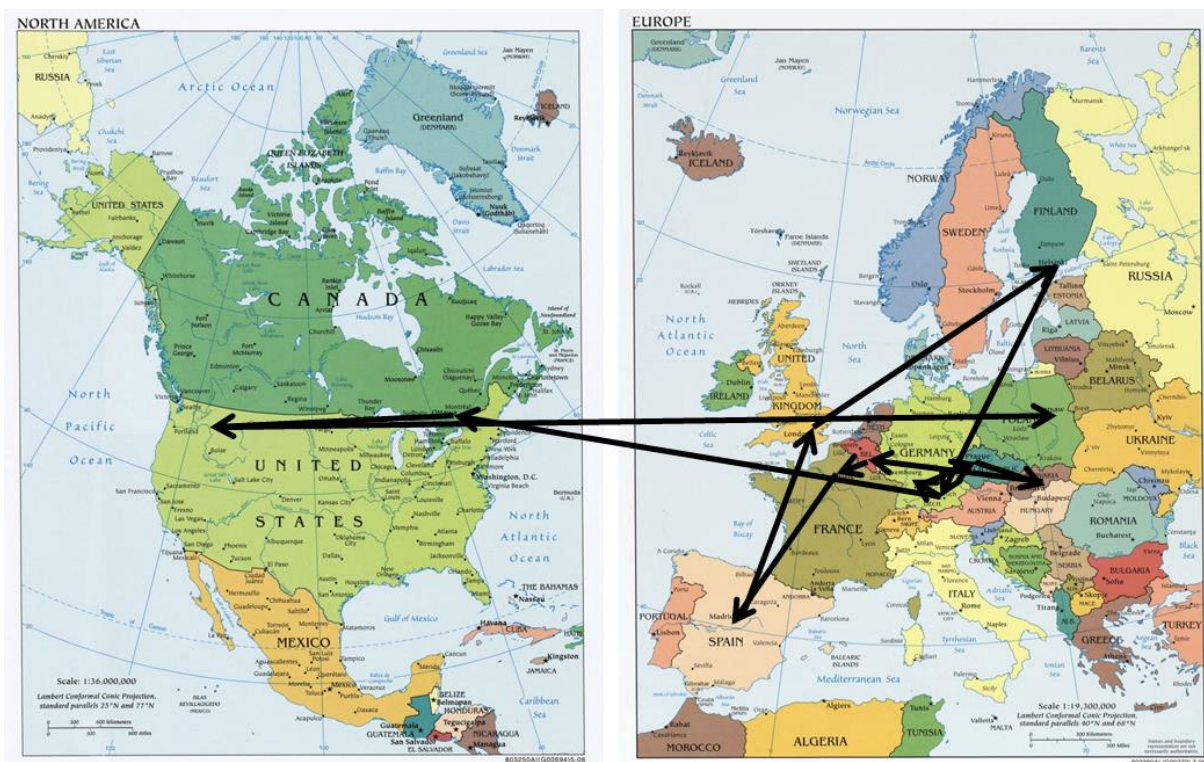
Figure 3.2: Transport route used for the phantoms travel between laboratories. Image adapted from Perry-Castañeda (2008) and Perry-Castañeda (2008a).

3.3 Measurements

All the measurements were performed at a distance of 1 cm between the phantom and the detector. For this purpose, a Plexiglas (polymethyl methacrylate) plate was provided to the participants with the phantoms, to be used as a spacer between the phantom and the detector. Each participant could decide the time of measurement; however, it was advised that the measurement uncertainty of the 59.54 keV net area peak should be below 1%.

Five positions were defined and marked in the BfS phantom based on the results obtained in a previous international intercomparison (Rühm, König et al. 1998) using this phantom, see Figure 3.3.
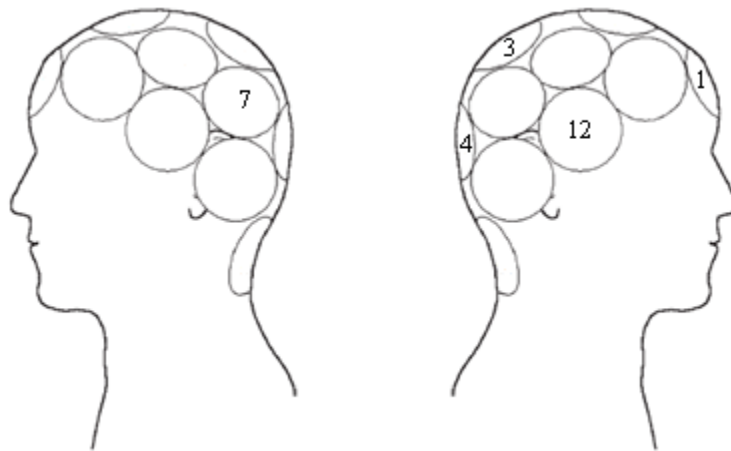
Figure 3.3: Measurement positions (1, 3, 4, 7 and 12) defined on BfS phantom on the right and left side; left and right figure respectively. Positions based on previous intercomparison (Rühm, König et al. 1998), Figure adapted from Rühm, König et al. (1998).

Measurements performed previously to the intercomparison exercise, showed that the inclination between the detector and the phantom surface, could affect the detection efficiency. Thus the inclinations used by the HMGU detector were and advised to be used by the participants, see Table 3.2 and Table 3.3.

Table 3.2: Measurements positions and respective inclination between detector and the surface of the BfS phantom used by the HMGU and advised to be used EURADOS WG7 intercomparison participants.

Measurement position	Inclination (degrees)
1	43°
3	57°
4	0°
7	0°
12	0°

For the measurement of the USTUR case 102 skull phantom, five positions were defined over the sagittaly cut and on the side that contained the case 102 contaminated bones; however, from these positions 3 and 4 were optional, see Figure 3.4. Additional optional positions, -2 and -3 were proposed for participants who desired to estimate the additional counting rate obtained on the measurements at positions 2 and 3 if the non-contaminated bone was contaminated, see Chapter 3. These positions were proposed based on typical positions used for skull measurements (Vrba 2010b), and on results obtained from an extensive set of measurements performed before the EURADOS intercomparison by Pedro Nogueira using a collimated detector in a effort to determine the positions on the skull phantom that provide higher detector counting rates.
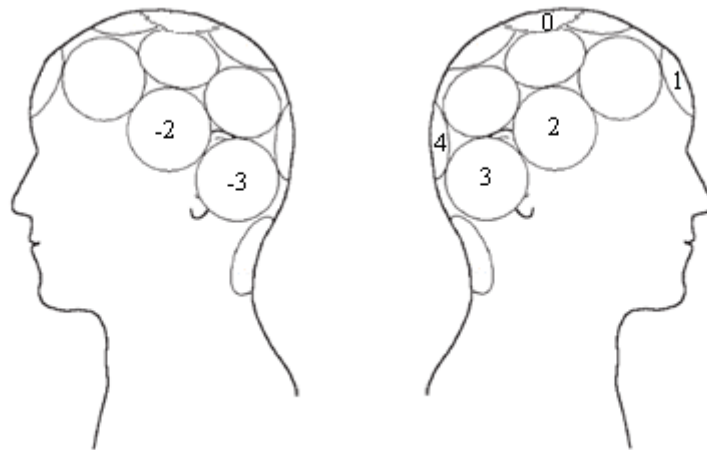
Figure 3.4: Measurements positions (-2, -3, 0, 1, 2, 3, 4) defined on USTUR case 102 skull phantom on the right side and left side; left and right figure respectively. Figure adapted from Rühm, König et al. (1998).

Table 3.3: Measurements positions and respective inclination between detector and the USTUR case 102 skull phantom used by the HMGU and advised to be used by the EURADOS WG7 intercomparison participants.

Measurement position	Inclination (degrees)
0	90°
1	34.5°
2 and -2	0°
3 and -3	-16.8°
4	26.5°

For the CSR phantom measurement, due to the geometry and shape of this phantom, only one position was defined, the detector should be placed perpendicular is a vertical position, see Figure 3.5. Since this measurement geometry is easy to reproduce the results obtained from this measurement were used to normalize the results obtained with the USTUR case 102 skull and BfS skull phantoms.
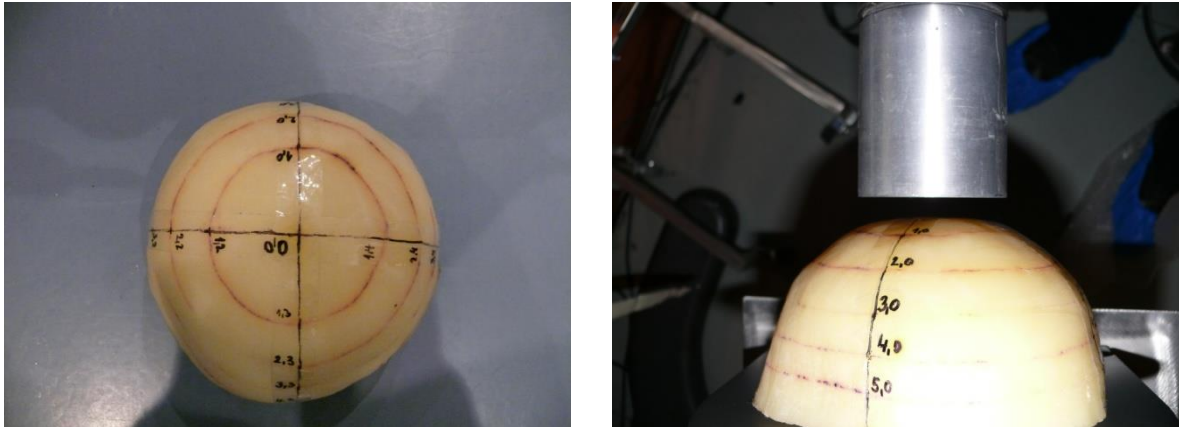
Figure 3.5: Measurement position defined on the CSR phantom, top and side view with detector in measurement position, left and right figures respectively.

3.3.1 HMGU results

Using the HMGU detector 3 the following results were obtained: for the BfS phantom the detector efficiency in the different positions is very similar, and a maximum relative difference of only 17% was found between position 3 and position 1, see Figure 3.6. This is possibly due to the use of a constant thickness of tissue equivalent wax over the skull bone (Laurer 1993) and a good distribution of the [241]Am point sources in the skull bone surfaces, and a similar and reproducible counting geometry.
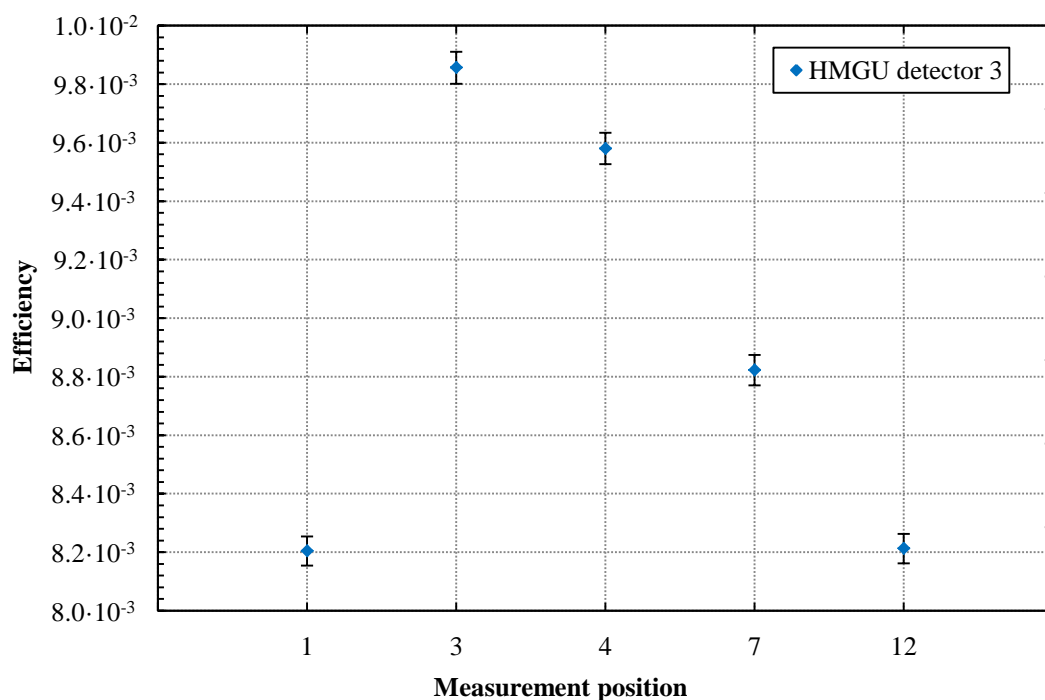
Figure 3.6: HMGU results obtained for task 1 measurement of BfS phantom. Error bars correspond to one sigma counting statistics.

During the previous intercomparison Rühm, König et al. (1998) studied the spatial distribution of the [241]Am on the BfS phantom, using a germanium detector with a led collimator. With this collimated detector variations up to 50% were found between the counting rates obtained in different positions, however, it was not clear if this was due to the activity distribution of the sources in the skull bone or to the result of the phantom geometry. For the positions measured in the current intercomparison, Rühm, König et al. (1998) found a good agreement between them with variations below 11% which is better than 20% maximum deviation found in the current intercomparison, however, this can be easily justified by the differences in the measurement procedures since in current measurements no collimator was used.

The results of the USTUR case 102 skull phantom results are very different from those obtained with the BfS phantom. In Figure 3.7, one can see that the efficiencies for the side positions 2 and 3 are very similar with a relative difference of only 4%. The positions -2 and -3, both at the non-contaminated side, have a relative difference of 50%, which is possibly due to a construction defect that led to incomplete filing of this phantom, and that can be observed in Figure 5.4 from the voxel phantom constructed by Vrba (2010a) based in Computer Tomography images of the USTUR case 102 phantom (Tabatadze, Brey et al. 2008), where considerable region corresponding to the brain is visible that is filled with air. Taking into account this problem the results show that if the non-contaminated bone was contaminated, the results obtained for measurement in position 2 and 3 would be approximately 22% and 11% higher, respectively. Note that the problem with the filling is specific to this phantom only.

Concerning the measurements performed over the sagittal cut, the detection efficiency obtained for positions 1 and 4 show an excellent agreement with a relative difference below 1%. Position 0 should be similar but the relative difference between this position and position 1 is approximately 35%. This is possibly due to the irregular alignment between the skull sagittal cut and the soft tissue equivalent material: note that it can be observed in the Figure 5.4 from the USTUR case 102 voxel phantom that at the top of the head significantly more than half of the bone belongs to the case 102 contaminated bone.

Despite the missing contribution from the opposite side in position 2 and 3 measurements; in the calculation of the efficiency for these two measurements there is an overestimation of the detection efficiency, because the [241]Am is only in one half of the skull and is not distributed in the complete skull as in a real [241]Am bone contamination or calibration phantom. To hypothetically correct the detection efficiency for these two positions for a complete contaminated skull, the USTUR case 102 phantom [241]Am activity needs to be doubled and the missing contribution from the non-contaminated side needs to be added.

No overestimation occurs in positions 1 and 4. Because, they are along the sagittal cut they measure only half of the counts they would if the complete skull bone was contaminated. This effect compensates for the need to double the USTUR case 102 phantom [241]Am activity in the detection efficiency calculation for these positions.

Hypothetically taking into account the previous corrections a good agreement can be found for the positions 1 and 4 when comparing with those of 2 and 3 (after doubling the activity value and adding the counting contribution of the non-contaminated side — positions -2 and -3); a relative difference of approximately 14% was found for both position 1 and 4 comparing with position 2, for both position 1 and 4 comparing with position 3 a relative difference of approximately 6% was found.
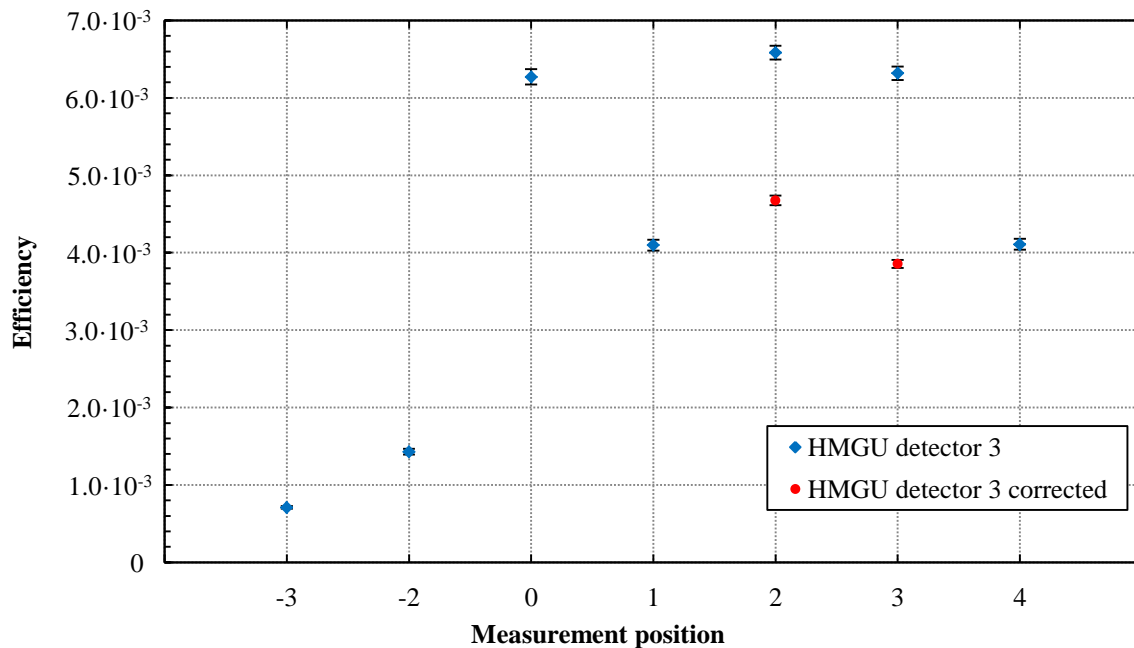
Figure 3.7: HMGU results obtained for task 1 measurement of USTUR case 102 phantom and results for position 2 and 3 after correction. Error bars correspond to one sigma counting statistics.

3.3.2 HMGU validation

As different detectors have different characteristics such as the germanium crystal diameter and thickness, or material and thickness of the end cap, each detector has a unique detection efficiency. As a consequence, a direct comparison between the participant's results was not possible. However, this comparison can be achieved through the normalization of the results. In this work this normalization was done dividing the USTUR case 102 and BfS phantom results by the CSR phantom result for each participant, so that the detector specific characteristics such as the dead layer thickness, end-cap window material and thickness, charge collection, which are responsible for the detector intrinsic efficiency, are cancelled out. The participant's normalized results for the full energy peak efficiency at 59.54 keV were then compared with HMGU normalized results. In order to estimate the accuracy of the results the statistical measurement uncertainty was taken into account.

In Figure 3.8, the BfS phantom average of the relative differences between the participant's results and the HMGU detector 3 normalized is shown. Excellent agreement was found with a relative deviation below 5 %. The best results were obtained for the positions 1, 3 and 4 where the average of the relative deviation is below 1%.

The results obtained with USTUR case 102 skull phantom are shown in a similar way in Figure 3.9. There is a general good agreement, with the average of the relative deviations being below 11% for all positions. The best results were obtained for positions -2, 3 and 4 where the average of the relative deviation is below 4%; the largest difference was obtained for the measurement of position -3, which is possibly due to difficulties in phantom positioning, since this position is not typically used in routine measurements.
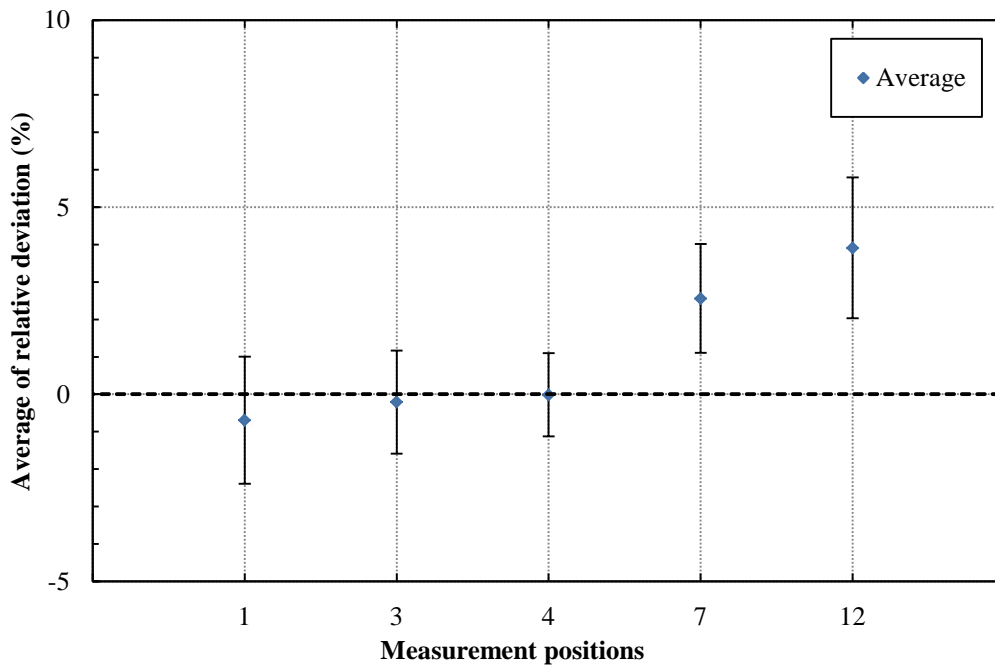
Figure 3.8: Relative deviation between the results obtained by the EURADOS Intercomparison participants and those obtained with HMGU detector 3, for BfS phantom. All results are normalized with the results obtained using the CSR phantom. Error bars correspond to a one sigma statistical uncertainty.
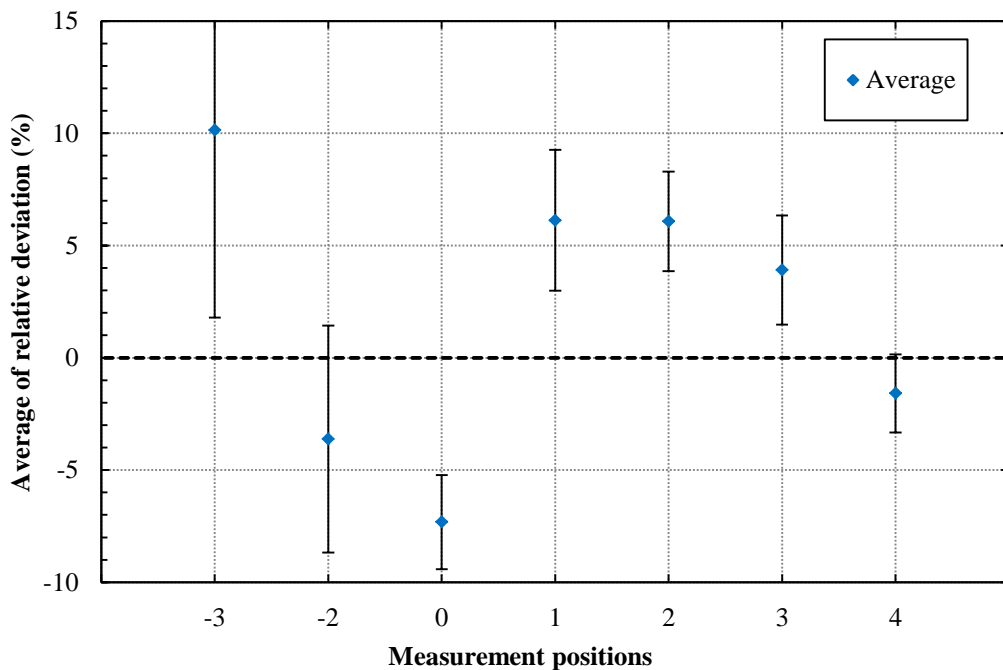
Figure 3.9: Relative deviation between the results obtained by the EURADOS Intercomparison participants and those obtained with HMGU detector 3, for USTUR case 102 skull phantom. All results are normalized with the results obtained using the CSR phantom. Error bars correspond to a one sigma statistical uncertainty.

3.4 Discussion and Conclusion

The relative deviations obtained for the USTUR case 102 phantom are in general superior to the values obtained with and the BfS phantom. This is possibly due to several factors including the sagittal division of the USTUR BPAM phantom that will increase the positioning uncertainty since for the positions 0, 1 and 4 the detector, as already mentioned, only measures approximately half of the contaminated bone. Additionally the sagittaly cut is not perfectly aligned with the head soft tissue: in the CT images of this phantom it can be observed that the top of the head contains significantly more contaminated bone than non-contaminated bone.

In addition, the USTUR Case 102 phantom has variation on the thickness of the soft tissue equivalent material that covers the skull bone, however, due to bone remodelling, calcification and resorption the ^{241}Am is not homogenously distributed in the bone surface. While in the BfS phantom a constant thickness of tissue equivalent wax was used over the skull bone and a homogeneous distribution of the ^{241}Am point sources in the bone surfaces was achieved.

Finally the size of the USTUR phantom is significantly bigger than that of the BfS phantom which can result in additional difficulties in the positioning of this phantom.

In general an excellent agreement was found between the results obtained from the participants in the EURADOS intercomparison and the results obtained at the HMGU partial body counter, with relative deviations below 5% for BfS phantom and below 10% for the USTUR case 102 phantom. These results validate the HMGU PBC measurements.

4 Monte Carlo Simulations

4.1 Motivation

In Partial Body Counting, the estimation of any incorporated activity is intrinsically dependent on the calibration of the detection system with an anatomical phantom containing a known activity of the radionuclide of interest, so that it simulates the characteristics of an individual who as been internally contaminated with that radionuclide. The availability of the proper phantom and calibration source represents one of the main limitations of this method. Additionally due to the morphological variability among individuals, it is necessary to conduct several calibration procedures to better estimate the incorporated activity (Kramer, Burns et al. 2002). These procedures are expensive not only because they require the use of several phantoms, but also because they represent a time-consuming processes (Carinou, Koukouliou et al. 2007). These disadvantages make computational methods like Monte Carlo very attractive for modelling such systems.

4.2 Monte Carlo method

The Monte Carlo method is a popular tool since it allows solving complex problems, through the use of pseudo-random numbers. There are several reports on the application of this method in the human history; however the official birthday was only in 1949 with the publication of a paper titled "The Monte Carlo Method" by Metropolis and Ulam (Metropolis and Ulam 1949, Dimov 2000).

This method is particularly useful in Boltzmann radiation transport problems, due to their stochastic nature and is currently the only method able to calculate the integral of the Boltzmann equation in a human body model, taking in to account all possible interactions (Xu and Eckerman 2010). In this method, the transport of a particle through matter is performed with the generation of a pseudo-random number and the knowledge of the interaction probability between the particle and matter. With these two values the distance which the particle travels is calculated, a new position for this particle is defined and depending on the interaction an amount of energy is deposited of the interaction site. This process is repeated until the deposition of all energy from the simulated particle, or until the particle energy value is below a predefined threshold (cut-off), or until the particle exits from the simulated world region of interest.

Due to the statistical nature of the Monte Carlo method, the final result represents an approximate solution of the problem. By repeating the transport process several times always using different pseudo-random numbers and combining the results, the accuracy of this approximation can be improved. This repetition process will increase the computational time necessary proportionally to the number of repetitions. However, in special circumstances their number can be reduced significantly through the use of variance-reduction techniques that increase the rate of convergence of the Monte Carlo algorithm (Dimov 2000).

In the last 25 years the use of Monte Carlo methods and their complexity have significantly increased due to several factors. The first one is the increase of computational power and the decrease of monetary cost. The second is the great effort made in the measurement and dissemination of cross-section data, which is fundamental for the simulated particles transport. The third is that major international exercises have validated, benchmarked and

ultimately improved the physical models used by the Monte Carlo codes (Vaz 2010). The most recent contribution is the dissemination of powerful software that provide a user-friendly environment interface with the underlying Monte Carlo code, e.g. GATE (Strulab, Santin et al. 2003) and Voxel2MCNP (Hegenbart, Polz et al. 2012).

There are currently several Monte Carlo codes available that were developed for the radiation dosimetry field. From this the most used are the codes Monte Carlo N-Particle (MCNP), Monte Carlo N-Particle eXtended (MCNPX), Geometry ANd Tracking (GEANT4), PENetration and Energy LOss of Positrons and Electrons (PENELOPE), FLUktuierende KAskade (FLUKA), Electron and Gamma Shower (EGS), and Particle and Heavy Ion Transport code System (PHITS). Most of these codes have been originally designed and developed for nuclear and high energy physics and as a consequence some of them include severe limitations in handling high resolution voxel phantoms, e.g. MCNPX (Xu and Eckerman 2010).

In this work the Monte Carlo codes MCNPX and GEANT4 were used. Both codes are significantly different in their philosophy, advantages and disadvantages.

The MCNPX advantages are: a) it is ready to be used; b) the script language is easy to learn; c) it's the number one code used in Radiation Protection and thus as a big supporting community; d) it contains powerful variance reduction tools and e) it's easy to install. The MCNPX main disadvantages are: a) limitation on the maximum number of voxels it's a limiting step for the use of high resolution voxels phantoms; b) currently it is not free; c) the source code is written in an old functional-oriented Fortan90 programming language and d) there is a limited access to the source code, so the user ends up using a "black box".

The GEANT4 advantages are: a) it is flexible and customizable, i.e. it allows the user to develop his one code and optimize it for his specific problem; b) it offers a great variety of physical models for low and high energy; c) the code is regularly debugged and improved; d) the code is written in the modern object-oriented C++ programming language; e) it's free and an Open source code; f) it allows a easy set of complex geometries by direct conversion of Computer-aided design and g) there is a big supporting community. The GEANT4 main disadvantages are: a) it demands a good knowledge on C++ programming language and object-oriented programming; b) the user needs to have a complete knowledge of the problem physics in order to be able to set the necessary or more accurate models for the simulation, and thus it requires to be validated has it was done in this work by comparison with the MCNPX calculations; c) the installation requires basic knowledge about necessary parts of GEANT4 which the user needs and d) the GEANT4 manual is written for programmers.

In the present work, all Monte Carlo calculations were performed using an Intel(R) Core (TM) i3 CPU. However, the MCNXP calculations were performed in a Microsoft Windows XP operating system and the GEANT4 calculations were performed in a GNU/Linux UBUNTO operating system. No variance reduction method was used, so in order to reduce the relative statistical uncertainty to levels below 1%, it was in general necessary to simulate 10^8 particles histories. In MCNPX this calculation required 130 min and 210 min of CPU time for the simulation of a point source and a voxel phantom respectively. In contrast for the GEANT4 this calculation required 60 min and 420 min of CPU time for the simulation of a point source and for the simulation of a Voxel phantom, respectively.

This means that for the identical calculations GEANT4 required approximately half of the CPU time for the simulation of a point source, however, it needed 2 times more CPU time

than MCNPX for the simulation of the voxel phantom. Accordingly to the values presented by Kim, Jeong et al. (2011) at this energy range the CPU time needed for the particle transport simulation in a voxel phantom should be approximately the same for both codes. The additional time required by in GEANT4 calculations is possibly due to a user-defined code developed for the voxel phantom implementation that decreases the performance of this code.

4.2.1 Geant4

The Geometry ANd Tracking (GEANT4) it is not a code but a toolkit for Monte Carlo simulations (Agostinelli, Allison et al. 2003). It was been design with a modular structure that allows the user to customize the processes and models used for the particle transport simulation. It allows the simulation of electromagnetic, hadronic and optical processes in the energy range from 250 eV to TeV (Agostinelli, Allison et al. 2003). In this work it was been used the GEANT4 version 9.3.

For the simulation of the electromagnetic physics three models are available: Standard, Livermore and Penelope. In this work it as used the Penelope model due to the observed improvement in the agreement between the calculation and measurement results.

The GEANT4 9.3 version Penelope model is based on the Penelope Monte Carlo code version 2001 (Salvat and Agency 2001), since it was originally written in the FORTRAN77 programming language was necessary to covert and adapt it to the GEANT4 C++ programming language (Amako, Guatelli et al. 2005). The GEANT4 Penelope allows the transport of photons, electron and positions from 250 eV to 1 GeV and contains the majority of physical processes available in the original Penelope code: photoelectric effect, Compton scattering, Rayleigh scattering, Pair production (Gamma conversion), Annihilation, Bremsstrahlung, ionizing interaction and atomic relaxation after photoelectric effect (Poon and Verhaegen 2005). However, the transport mechanisms from the Penelope such as the mixed simulation of electrons/positrons and the "random hinge" algorithm were not implemented in GEANT4 (Salvat, Fernandez-Varea et al. 2001, Poon and Verhaegen 2005). Has consequence the electron transport in GEANT4 9.3 is different from the original Penelope, which is a mixed between "condensed history" and "detailed history" multiple scattering algorithms (Gavaldà, Varea et al. 2009).

The electrons transport in GEANT4 is performed through the "condensed history" method developed by Berger (Berger 1963) and implemented through a class II scheme: in this scheme the primary and secondary particles are always correlated, in opposition to the class I, used by MCNPX, were the primary and secondary particles are treated independently. Because the cross-section to use needs to be calculated during the transport it's difficult to use the Goudsmit and Saunderson (1940) multiple scattering theory. Thus in alternative the Lewis (1950) multiple scattering theory is used. This algorithm as the advantage of not producing calculation artefacts and don't required interpolations from a predetermine energy grid (Kawrakow 2000).

To limit the computational time, cut-offs for the particles transports were set. Accordingly to the GEANT4 philosophy these cut-offs are made in terms of range (range cut) has it provides a more coherent set between the simulation of different particles transport (Agostinelli, Allison et al. 2003). The range cut was set to 1 μm for both photons and electrons, which can

be translated to 2.84 keV for electrons and below 0.99 keV for photons when the particles transport is performed in the Germanium crystal.

The Livermore evaluated photon data library (EPDL 89) cross section was used for the photons and the Livermore evaluated electron data library (EEDL) was used for the electrons.

All calculation used the HepJamesRandom algorithm from the HEPRandom module of the CLHEP library (Collaboration 2009). This pseudo random number generator is a modification of an algorithm develop by James (James 1990) and it allows the use of a seed (in this case time) for the generation of a new pseudo-random number sequence for different simulations.

The detector geometry has set using Constructive Solid Geometry (CSR) representations. The voxel geometry as implement using the G4PhantomParameterization, as demonstrated by Garny (2009), this requires more computer memory in comparisons with another implementation, but allows faster calculations thanks to its simplified navigation.

To simulate the energy broadening observed in a radiation detector an algorithm in C++ was developed to perform the Gaussian energy broadening of the pulse-height response or spectrum using as input values the Full Width at Half Maximum (FWHM) from the measurement results. The end result is a realist spectrum that can be directly compared with the measurement spectrum.

4.2.2 MCNPX

The Monte Carlo N-Particle eXtended (MCNPX), is a Monte Carlo from the MCNP family design for general purpose radiation transport simulations. In this work it was used the MCNPX, version 2.6 (Pelowitz 2008) with the main purpose of confirming the GEANT4 results.

The computation of the energy deposition in the detector sensible volume was performed using a surface crossing estimator that computes the energy of the particles leaving the region of interest and subtracts it from the energy of the particles entering the region of interest ("F8 tally"), thus allowing the calculation of the energy distribution of pulses created in a detector by radiation (Pelowitz 2008).

Coupled photon:electron transport was used in all calculations and the following interaction models were available: photoelectric effect, Compton scattering, coherent (Tompson) scattering, incoherent scattering, pair production, Annihilation and Bremsstrahlung (Hendricks 2000).

The electrons transport in MCNPX is performed through the "condensed history" method developed by Berger (Berger 1963) and implemented through a class I scheme: meaning that the cross sections that determine the energy loss rate and the multiple scattering angles are calculated on a fixed predetermined energy loss grid (Kawrakow 2000, Reynaert, Palmans et al. 2002). This scheme presents the advantage that it can use the Goudsmit and Saunderson (1940) multiple scattering theory, which can provide a more accurate treatment of multiple elastic scattering (Kawrakow 2000). However there are disadvantages such as the lack of correlation between the transport of the primary and knock on electron, which can result in calculation artefacts (Seltzer 1991), and the necessity of interpolation when the electron step

doesn't match the energy grid (Kawrakow 2000, Nogueira, Zankl et al. 2011). The MCNPX provides two methods for the interpolation: the default electron energy indexing algorithm, so-called "bin-centred" treatment (Pelowitz 2008), uses the cross section at the upper boundary of the energy group in which the electron starts the step; alternatively the MCNPX provides the possibility of using the so-called Integrated Tiger Series (Halbleib, Kensek et al. 1992) electron energy indexing algorithm also known as "nearest group boundary" treatment (Pelowitz 2008). In this case, the cross section of that energy group is selected from the boundary of which is closest to the energy of the electron at the beginning of the step. Jeraj, Keall et al. (1999) found that results obtained with the bin-centred treatment can deviate from experimental values by approximately 10% for the maximum energy deposition for electron depth dose distributions, whereas the results derived with the nearest group boundary treatment show a better agreement with the experimental values. In view of the superiority of the ITS-style electron energy indexing algorithm (Jeraj, Keall et al. 1999, Chibani and Li 2002) it was used in all calculations.

To limit the computational time, the energy cut cut-off was set to 10 keV for electrons and 1 keV for photons. Also for the electrons transport the number of electron sub-steps per energy step (ESTEP) used was 3 (MCNPX default) for the calculations.

The default MCNPX cross section libraries Monte Carlo photon library (MCPLIB04) that is derived from the ENDF/B-VI.8, that by its turn was partially based on the EPDL97, was used for photons and the electron library (EL03) was used for electrons (Pelowitz 2008).

The native Gaussian energy broadening (GEB) from the MCNPX scorer ("F8 tally") was used. This feature allows the physical detector energy broadening simulation using as input values the Full Width at Half Maximum (FWHM) from the measurement results.
The detector geometry was implemented through the use of surfaces boundaries and Boolean operators and the voxel models were set through the use of the MCNPX repeated structures features as demonstrated by Taranenko (2005).

4.3 Computational set-up

4.3.1 Detector model – definition and validation

The detector 3 modelling included all main structures and materials that compose the detector, except for the electronic components of the detector. The nominal dimensions of the different components were provided by the manufacturer. The germanium crystal has a 25 mm radius and 10 mm length. The front and side contacts (dead layers) (0.5 μm thickness) and the back contact (0.5 mm thickness and 12 mm radius) were also simulated. The bevel with 2.5 mm radius in the front edge of the crystal has also been implemented. The crystal is placed inside a aluminium cup and enclosed by an aluminium end cap with 35 mm radius, 1.5 mm thickness and a 25 mm radius entrance with a 1.1 mm thick carbon fibber window positioned at 5 mm distance from the crystal front dead layer.

4.3.2 Detector model optimization

Discrepancies between the computational and measurement results are usual, and typically arise from the lack of accurate knowledge of the real dimensions of the detector. The main sources of bias are the dead layer thickness which increases with time due to lithium diffusion, and depends on storage conditions (Laborie, Le Petit et al. 2000), the crystal to window distance, the crystal length, the crystal radius, and back contact thickness (Helmer, Hardy et al. 2003, Hurtado, García-León et al. 2004, Jurado Vargas and Guerra 2006).
Each of these sources has a different impact on the detection efficiency. The front dead layer will affect the efficiency for low-energies, proportionally to the gamma-ray energy absorption (Nogueira, Silva et al. 2010). The crystal to window distance will influence all spectrum energies, since it will change the solid angle between the source and the crystal. The crystal radius and side dead layer will also influence all energies, since it changes the crystal sensible volume and the solid angle between source and crystal. The crystal length and back contact will mainly influence the high-energy region since low-energy gammas will be mainly absorbed in the front section of the crystal (Luís, Bento et al. 2010, Nogueira, Silva et al. 2010). For detectors with close end coaxial crystals the hole diameter and length can be also a source of bias. However, according to Garcia-Talavera et al. (2000), the influence of the hole diameter is negligible.
Another factor that can generate discrepancies is the non-alignment of the crystal in relation with the detector end-cap, as can be seen in Johnston (1985). The easiest method to verify this alignment is through X-ray photographs from to different directions (Debertin and Helmer 1988).

As can be seen in Figure 4.2, detector 3 crystal is aligned with the end-cap, which was confirmed by an additional X-ray photograph taken from a different direction (not showed here). In this image it can also be observed that there are several additional structures in the detector crystal cup that are not represented in the manufactures sheet, besides this few additional information can be deduced concerning such as the fact that the distance between the crystal and the window should be smaller than reported by the manufacturer, see Figure 4.1 and Figure 4.2.
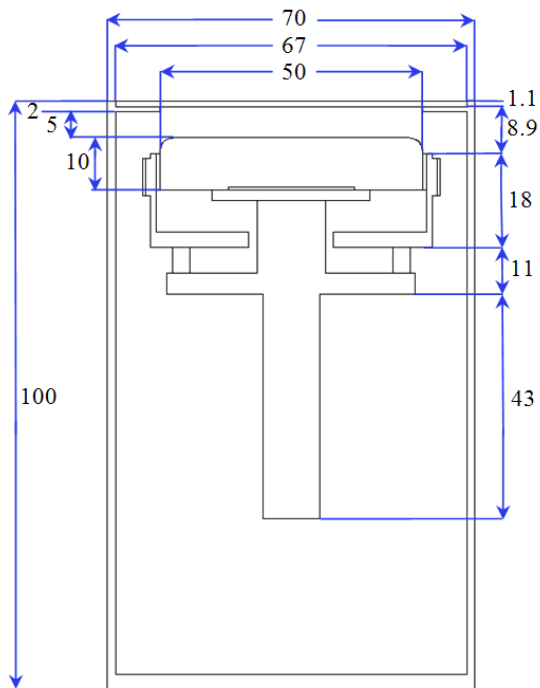
Figure 4.1: Cross section view of detector 3 geometry implemented in MCNPX and Geant4 as provided by the manufacture. Dimensions are mm.
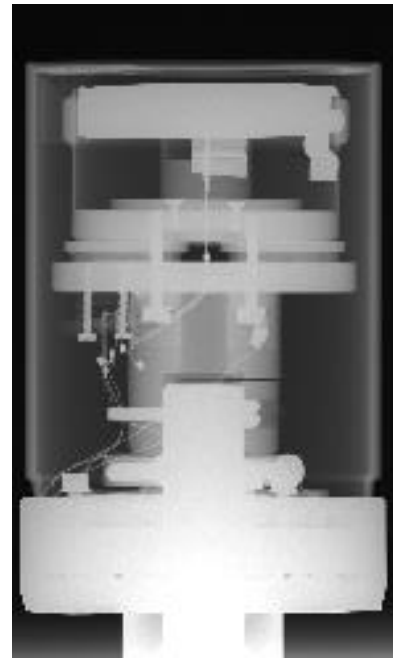
Figure 4.2: HMGU Detector 3 radiography with focus in the front of the end cap; generated with 70 kV, 32 mAs exposure.

For the optimization of the geometry used in the MCNPX and GEANT4 simulations, measurements at different distances were performed using point sources of the following radionuclide's: ^{241}Am, ^{210}Pb, ^{109}Cd, see Table 4.1. The sources were positioned in a centre position relative to the detector end cap window and measured at 1 cm and 5 cm distance, see Figure 4.3. These measurement conditions were reproduced in the computational set-up and both results were respectively compared. In a first stage all calculations were performed with MCNPX, then after the conclusion of the optimization process GEANT4 was used.

In order to estimate the accuracy of the results, uncertainty propagation using the Monte Carlo uncertainty and counting statistics uncertainty was performed. Note that no positioning uncertainty was taken in account for the Gaussian uncertainty propagation.

Figure 4.3: Detector 3 and [241]Am point source in irradiation geometry at 5 cm distance.

Table 4.1: Calibration point sources radionuclide's energies, activities and emission rate in gammas per second.

Radionuclide	Energy (keV)	Activity (Bq)	Uncertainty (Bq)	Emission rate (gps)	Uncertainty (gps)
[241]Am	26.34	4919	53	113.618	4.1
[210]Pb	46.54	3603	36	153.137	2.1
[241]Am	59.54	4919	53	1766.731	20.8
[109]Cd	88.03	158	2	5.849	0.2

In Figure 4.4, the relative deviations between the full energy peak efficiency obtained by experimental measurements and by MCNPX simulation are shown. For the nominal dimensions the MCNPX results are were general 5% to 13% lower than the measurements results except for the 26.34 keV efficiency, were an excellent agreement with a relative deviation below 2% between simulation and measurement was obtained.

Except for the 26.34 keV efficiencies, these results indicate the distance between the crystal and window should be smaller (see also Figure 4.2 and Figure 4.1). The possibility of modifying the dead layer thickness was excluded at this point, since the nominal value of the dead layer is only approximately 0.5 μm.
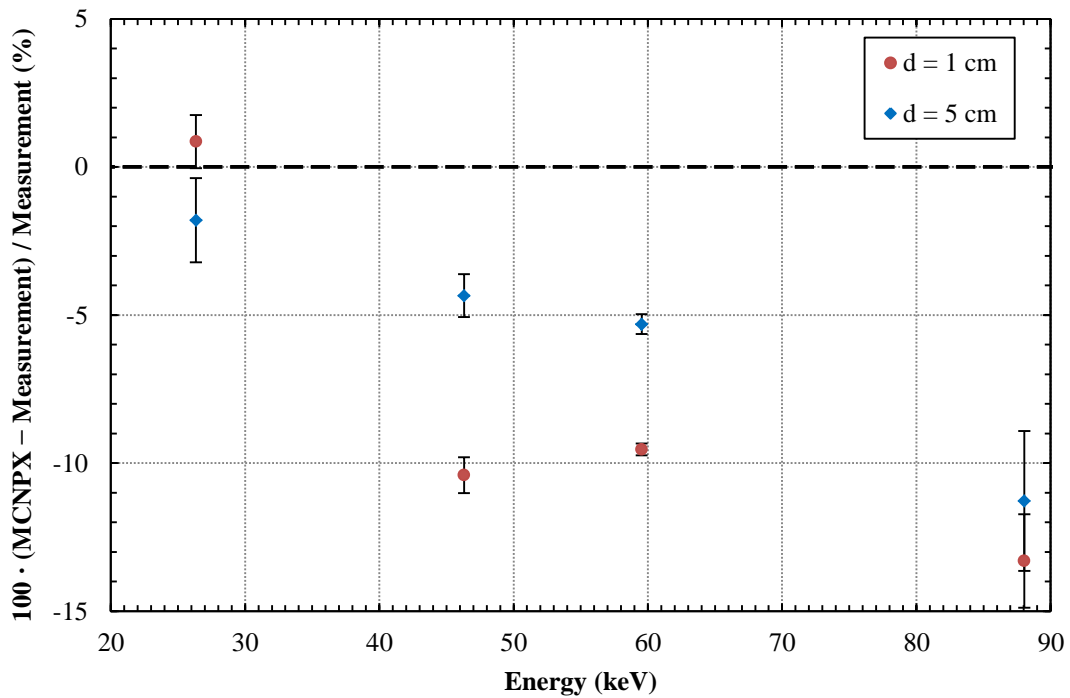
Figure 4.4: Relative deviation between measurements at 1 cm and 5 cm distance, and MCNPX calculation the full energy peak efficiency using the detector 3 nominal dimensions provided by the manufacturer (see also Figure 4.2). Error bars represent one sigma uncertainties.

For the optimization of the crystal-to-window distance, simulations were performed were this parameter was progressively reduced and at each step the results were compared with the measurement results. Through this method it was found that the distance of 3 mm, was optimal, for 59.54 keV the most relevant energy used in this work, and that the relative difference between simulated and measured efficiency for this energy is below the one-sigma uncertainty.

When this distance of 3 mm between crystal and detector window was used in the simulations, the relative deviation between simulations and measurements has improved (Figure 4.4) with a relative deviation below 2% for the efficiency at 46.53 keV and 59.54 keV, while at 89.03 keV the relative deviation as also improved and is now 3% and 6% for 1 cm and 5 cm distance respectively. However, both results have approximately 2.5% uncertainty only from the statistics. For the 26.34 keV efficiency the relative deviation is now 12% and 4% for 1 cm and 5 cm distance, respectively. This deviation is greater than in the nominal dimensions model and possibly indicates that the crystal dead layer parameter needs some minor optimization. However, taking into account the uncertainty of the measurements at low-energies such as 26.34 keV, it was decided not to perform an optimization of the crystal dead layer.
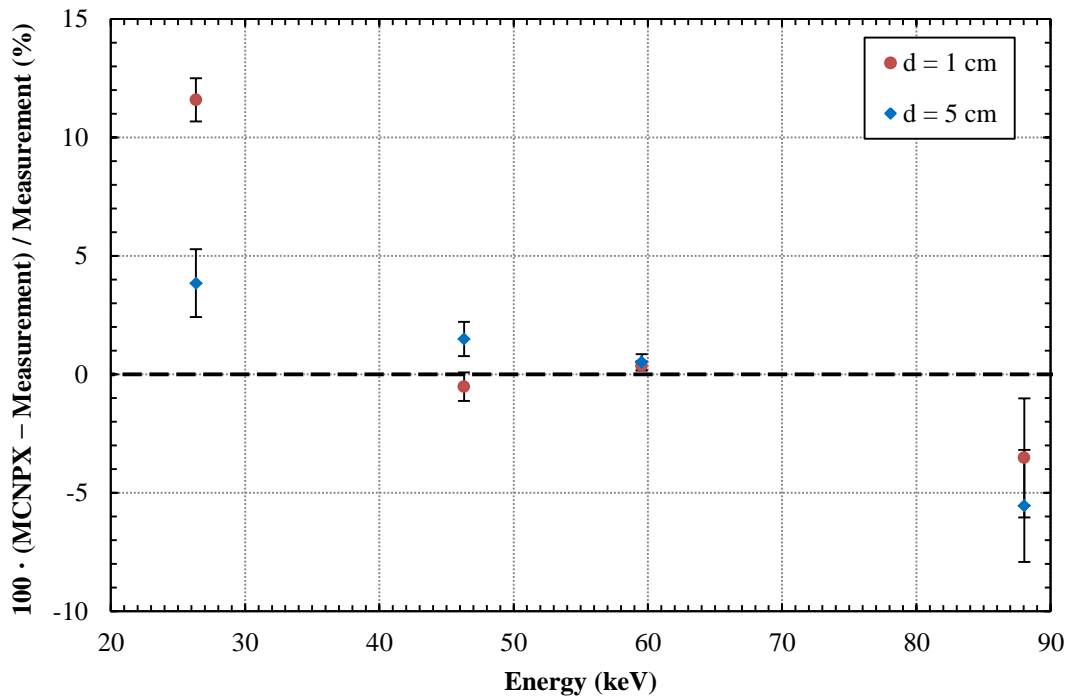
Figure 4.5: Relative deviation between measurements at 1 cm and 5 cm distance, and MCNPX calculation the full energy peak efficiency using the detector 3 optimized crystal to window distance. Error bars represent one sigma uncertainties.

4.3.3 Comparison between MCNPX and GEANT4

The detector 3 optimized model was implemented in GEANT4 and all previous calculations were reproduced with this set-up, see Figure 4.6. As in case of the MCNPX calculations there is an excellent agreement with relative discrepancies below 2% for the 46.53 keV and 59.54 keV efficiencies, while for the 89.03 keV efficiency the relative deviation is now 3% and 6% for 1 cm and 5 cm, respectively. At 26.34 keV there is a slightly improvement when compared with the MCNPX results, as the relative deviation is only 9% for 1 cm distance. This improvement its possibly due to the use of the Penelope physics list and respective cross sections and models for the electron transport, that at this low-energy will play a major role in the calculation.

In Figure 4.7 the relative deviation between GEANT4 and MCNPX is displayed. An excellent agreement was found between both codes with relative deviations around and below 1% for all energies, except for the 26.34 keV efficiency that shows a relative deviation around 2%.
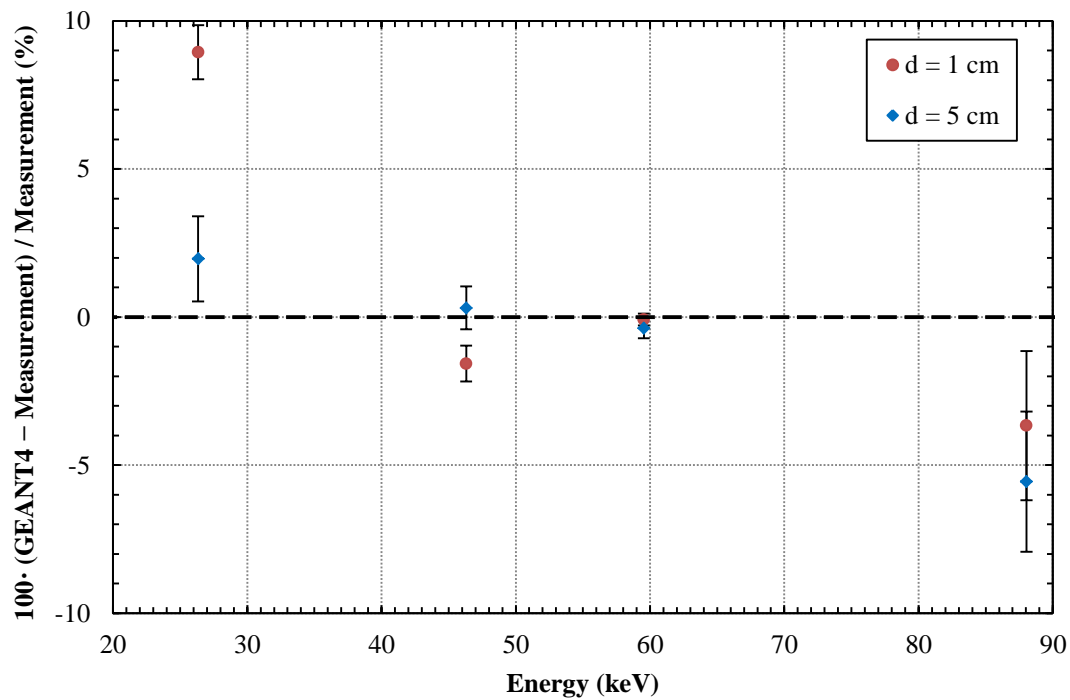
Figure 4.6: Relative deviation between measurements at 1 cm and 5 cm distances and GEANT4 calculation for full energy peak efficiency using the detector 3 optimized crystal to window distance. Error bars represent one sigma uncertainties.
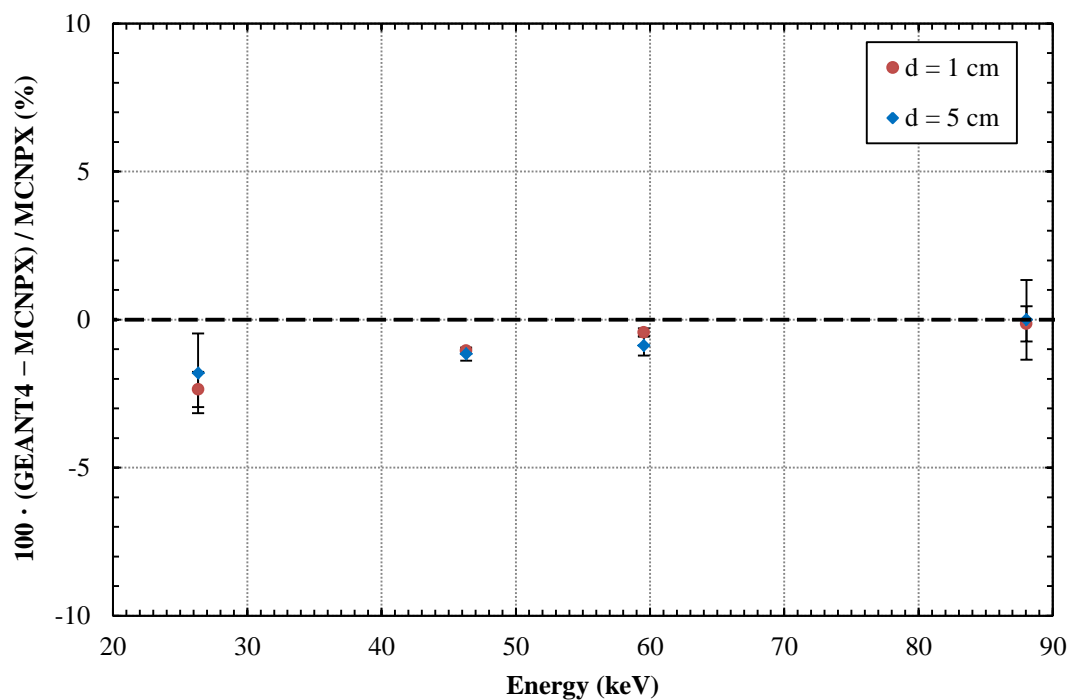
Figure 4.7: Relative deviation between GEANT4 and MCNPX calculation of full energy peak efficiency using the detector 3 optimized crystal to window distance. Error bars represent one sigma uncertainties.

4.4 Detector energy resolution – Simulation of full-energy spectra

The energy resolution is one of the most important characteristics of a detector as it is the limiting factor for the distinction between two full energy peaks with close peak energy.
In Monte Carlo simulations, gammas-rays depositing the same energy in the detector volume generate counts with the same energy. As an example, 59.54 keV gamma-rays would be detected as Dirac peak at 59.54 keV. However, analysing the experimental measurement of the same gamma-ray, it can be observed that the peak is spread in a Gaussian energy distribution, with a maximum at 59.54 keV. This spread of the counts or peak width is the result of uncertainties associated with the detection and measurements processes.

There are three main factors that contribute to the peak width: 1) the inherent statistics of the charge creation process; this is considered the most important of the three factors as it is intrinsic to the detector material and cannot be reduced; 2) the properties of the detector with respect to charge carrier collection efficiency; this is generally associated to low electrical field regions on the detector that result in an incomplete charge collection and consequently in a loss of charge carriers; 3) the sum of electrical noise from the detector and instrumentation electronics that depends mainly on the leakage current and capacitance of the detector (Debertin and Helmer 1988, Knoll 2010). The typical total peak width (W_T) created by gamma-rays of a certain energy is then the result of the quadrature of the sum of each contribution, as each of these contributions show a Gaussian distribution (Knoll 2010):

$$W_T^2 = W_D^2 + W_X^2 + W_E^2 \qquad\qquad 4.1$$

where W_T is the total peak width

 W_D is the peak width contribution from the statistics of the charge carrier creation process,

 W_X is the peak width contribution from the charge collection efficiency, and

 W_E is the peak width contribution from the electrical noise.

There is an additional contribution due to the gamma-ray energy uncertainty and respective shape, since this contribution shows a Lorentzian shape distribution while all the others discussed above show a Gaussian shape distribution. However, this contribution is negligible compared to the other contributions (Gilmore 2008).

In gamma spectrometry the energy resolution is measured in terms of the width of the full energy peak at half of the maximum value (FWHM). According to Debertin and Helmer (1988) this value can be determined by measuring a gamma-ray or X-ray source at any distance from the detector. However, the total count rate in the spectrum should not exceed 1000 counts per second, as the pulse pile-up may cause and additional broadening of the peaks. The peak should have at least 20000 counts to guarantee adequate statistics (Debertin and Helmer 1988).

Taking into account all the previous precautions as far as possible, [241]Am and [152]Eu calibration sources were measured so that the FWHM could be determined for the energy range from 26.34 keV to 1408.01 keV, see Figure 4.8.
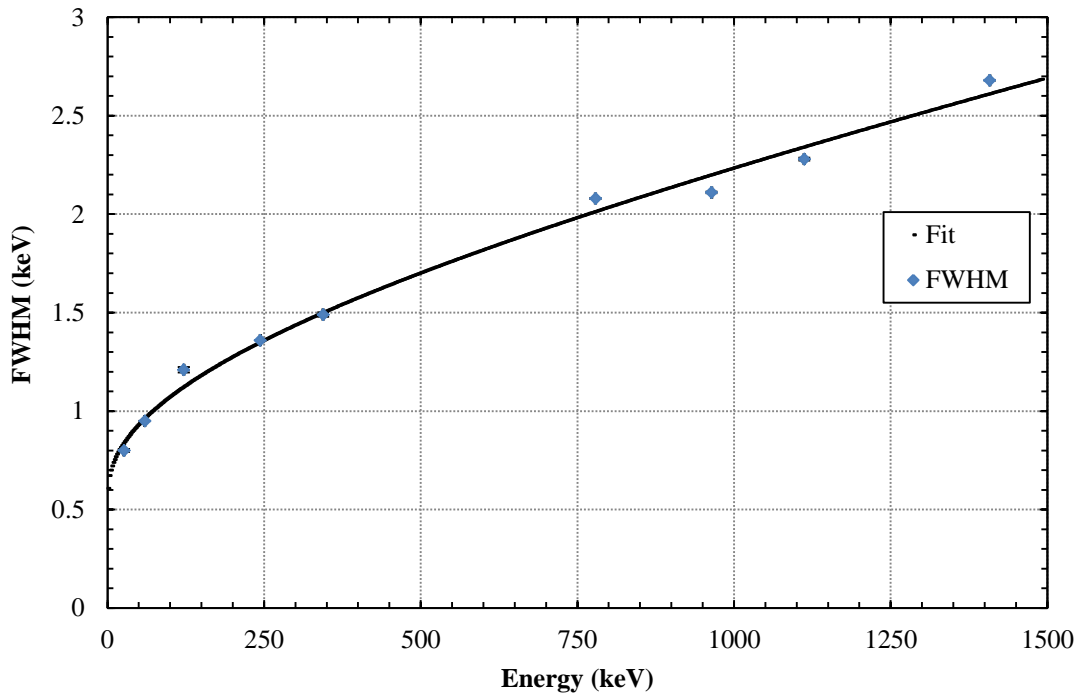
Figure 4.8: Measured FWHM of detector 3 using [241]Am and [152]Eu calibration sources, and fitted equation. Note that the one-sigma uncertainty is displayed except when the value is smaller than the symbol.

The type of fit of the FWHM values, depends greatly on the author since linear, quadratic and square root quadratic fits have all been successfully used to fit this type of data (Gilmore 2008). In this work the FWHM was fitted with the quadratic curve used by the Gaussian energy broadening option offered by the MCNPX (Pelowitz 2008) code:

$$FWHM = a + b\sqrt{E + cE^2} \qquad 4.2$$

where E is the energy of the gamma-ray, and
a, b, c are values obtained from a fit to the experimental data.

Using this equation the measured FWHM from detector 3 was fitted and the following values were obtained:

$a = 6.06 \times \cdot 10^{-1}$ keV; $b = 4.64 \times 10^{-2}$ keV$^{1/2}$; $c = 2.30 \times 10^{-4}$ 1/keV

As already mentioned, in the MCNPX and GEANT4 codes the factors that generate the energy resolution of a detector are not taken in to account. To simulate the energy resolution an algorithm in C++ was developed that uses as input the fit parameters a, b and c (Equation

4.2) from the measured FWHM and the relation between the Gaussian width (A) and the FWHM:

$$A = \frac{FWHM}{2\sqrt{ln2}} \qquad\qquad 4.3$$

With this a Gaussian broadening of the simulated GEANT4 spectra was performed using the following equation:

$$f(E) = Ce^{\left(\frac{E-E_0}{A}\right)^2} \qquad\qquad 4.4$$

where A is the Gaussian width,
     E is the broadened energy,
     E_0 is the unbroadened energy, and
     C is the normalization constant.

The final result is a realistic spectrum that can be directly compared with the measurement spectrum and the MCNPX native Gaussian broadening, see Figure 4.9.
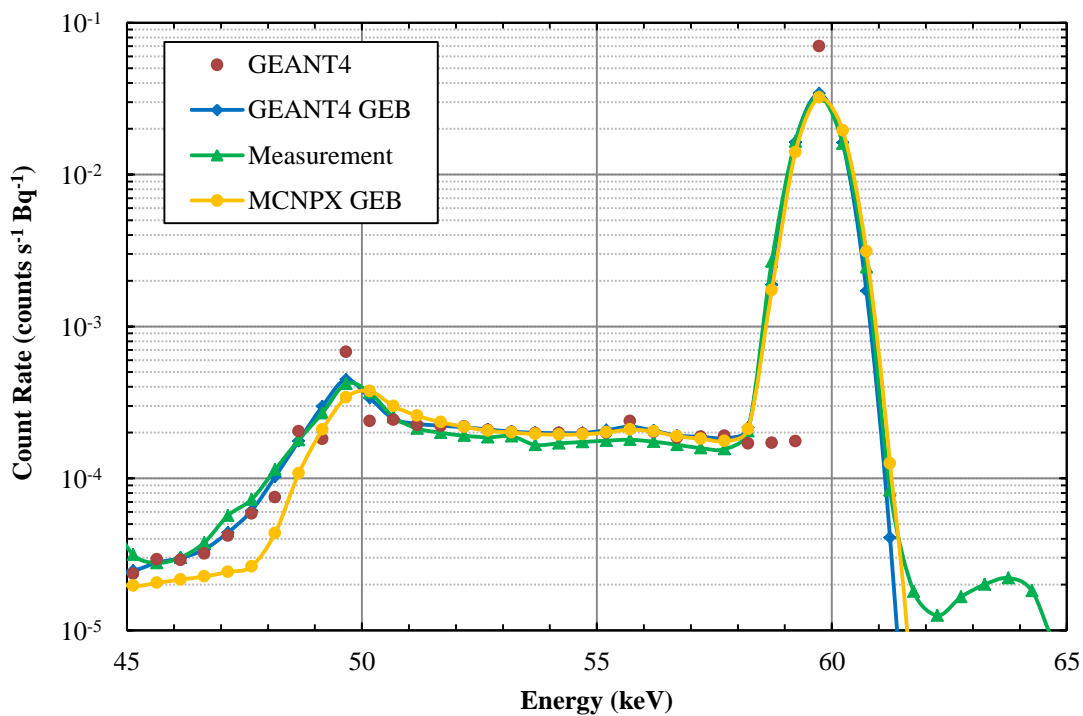
Figure 4.9: Detector 3 count rate of an ^{241}Am point source at 5 mm distance. Green symbols: measurement; red symbols: GEANT4 simulations without Gaussian energy broadening; blue symbols: GEANT4 simulation including Gaussian energy broadening using Equations 4.2 – 4.4; yellow symbols: MCNPX simulations including standard Gaussian energy broadening. Note that the one-sigma uncertainty is not displayed since the value is smaller than the symbol.

Minor differences can be observed between the MCNPX and the Gaussian energy broadening C++ algorithm for the 59.54 keV full energy peaks broadening. Since both algorithms use the same formulae this difference is possibly due to rounding differences between the FORTRAN90 and C++ code.

Comparing the GEANT4 and the MCNPX spectra one can see that in the backscatter region and lower energies (45 keV to 50 keV) they are different. This is possibly due to the use of different cross sections for the photon Compton scattering. Despite this as previously mentioned, an excellent agreement was found between the MCNPX and GEANT4 results for the full energy peak area.

Note that for energies above the 62.0 keV only the measurement counts are present. These counts are the result of an simultaneous detection of different photons and that are not recognised as separated events by the detector multiple channel analyser (Gilmore 2008). This effect is referred as pile-up, random coincidence or random summing (Gilmore 2008).

The pile-up results in the increase of the background, the production of non-existent peaks and as major consequence the lost of counts from the interest full energy peak (Gilmore 2008). The magnitude of this effect depends on the overlap between the arrival time of the different photons or the source activity, the emission probability of the photons and the detector specific parameters.

In contrast, pile-up is not observed in MCNPX and GEANT4 because both codes performed transport of only one particle per transport simulation.

5 Anthropomorphic Computational Phantoms

The difficulties associated with the development and construction of new and more realistic physical phantoms for efficiency calibration of detection systems, resulted in the development and exponential expansion of the use of anthropomorphic computational models. These models together with Monte Carlo methods allow to perfectly reproduce the calibration factors obtained by experimental methods with the advantage of being cost and time saving. Additionally, some of these models – due to their great detail – are closer to the human anatomy than the physical phantoms and consequently they allow an increasingly accurate calibration. They have also the advantage to be flexible in terms of their dimensions and composition; this allows the user to adjust the phantom to individual characteristics such as body size and mass and thus to increase the accuracy of the quantification of the incorporated activity.

5.1 Phantoms formats

During the last 50 years the complexity of the anthropomorphic models and their ability to describe the human anatomy has been significantly increasing allied to the increase of the computational power and the development of new and powerful imaging techniques such as computed tomography (CT) and magnetic resonance imaging (MRI). Anthropomorphic computational models can be divided into three groups according to their format, the stylized or mathematical phantoms, the voxel phantoms and the BREP or Hybrid phantoms.

5.1.1 Mathematical Phantoms

The first computational phantoms developed for the purpose of radiation protection represented the human body with simple geometric shapes like spheres, cylinders or parallelepipeds. It was only in the 60's that researchers from Oak Ridge National Laboratory (ORNL) developed the first anthropomorphic model at the request of the Medical Internal Radiation Dose Committee (MIRD), and thus it was baptized with the name MIRD (Snyder, Ford et al. 1969). The MIRD model divided the human body in three parts: the legs, the trunk and arms, and the head and neck. These body parts and respective organs were defined by primitives (e.g. spheres, cuboids, cylinders, cones, ellipsoids and prisms) combined with Boolean operations. Due to the limitation of the computational power available at that time this model was a hermaphrodite to restrict the calculations to just one phantom. The dimensions were based on an average Caucasian adult, the "reference man", a concept developed by ICRP-23 (1975) for radiation protection purposes. Shortly afterwards, the MIRD phantom family was developed which represented different ages and included a series of paediatric models, see Figure 5.1. In parallel to this work Kramer, Zankl et al. (1982) developed two models – "Adam" and "Eva" – which introduced the separation of the sexes.
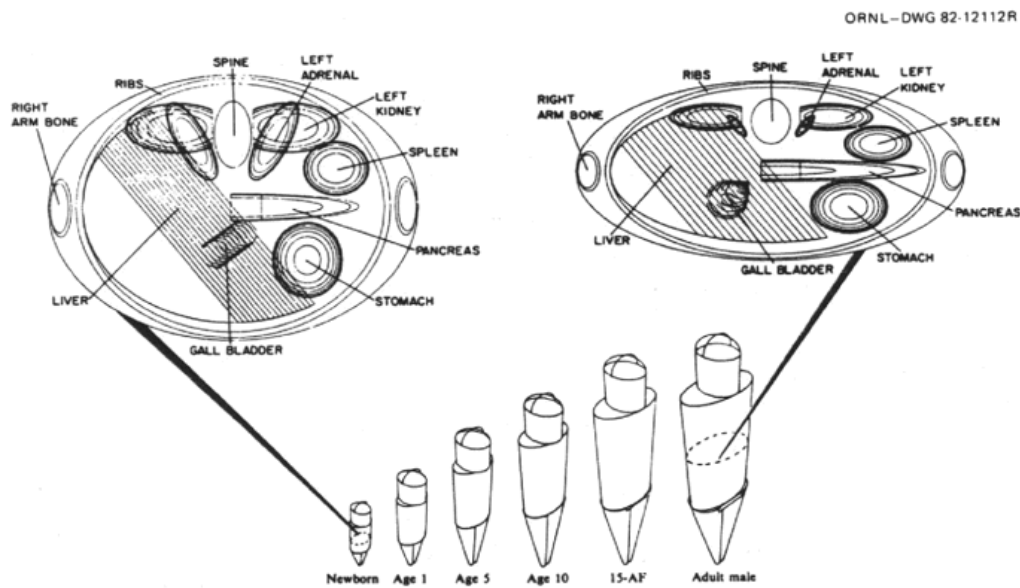
Figure 5.1: External view of the MIRD family of phantoms representing various ages that was developed by Cristy and Eckerman (1987). In addition, cross-sectional views of the newborn phantom (on the left) and the adult phantom (on the right) are shown as well.

In the past 30 years new and more detailed descriptions of the organs have been introduced in these models. However, even nowadays these phantoms are limited by the use of simple mathematical shapes to model the complex human anatomy shapes. As a consequence, these phantoms contained a series of unrealistic anatomical features on the shape and position of the organs. Despite these limitations this type of models is still being used and is in some aspects still superior to the more recent voxel phantoms such, for example, as in the modelling of the skin and the eye lens.

5.1.2 Voxel phantoms

Anthropomorphic voxel phantoms are computational human representations that take advantage of the use of an array of small cuboids (voxels) to describe the human body. They are built from anatomical cross-sectional images obtained from computed tomography, magnetic resonance imaging or photographs from cryosection cadavers, thus being able to describe all anatomical features with great detail. Recently two of these models, one for each gender, have become the ICRP reference models for dosimetry calculations (ICRP-110 2009). The development of voxel phantoms started in 1984 by Gibbs, Pujol Jr et al. (1984) and shortly after by Williams, Zankl et al. (1986). In 1994 Zubal built the VoxelMan phantom based on CT images from a human head and torso (Zubal, Harrell et al. 1994). Two years later, the first model with dimensions adjusted to reference man appeared, from MRI images with a resolution of 2 mm × 2 mm × 10 mm; this model was named NORMAN (Normalized Man) and was developed by Dimbylow (1996).

All the previous models were limited by the CT and MRI resolution that did not allow the definition of small anatomical structures. This led Xu, Chao et al. (2000) to develop a new phantom called VIP-Man, using photographs from the cryosection of a dead donor generated by the project Visible Human (VHP). This model consists of more than 3.7 billions of voxels and the image forming employed in its construction contains more than 1400 organs and

tissues. This model had such a high resolution and consequently high number of voxels that they needed to be reduced for being used with the Monte Carlo code MCNPX. Using the same images from the Visible Human project, Sachse, Werner et al. (2000) also developed a phantom to study electro-magnetic and elasto-mechanic effects.
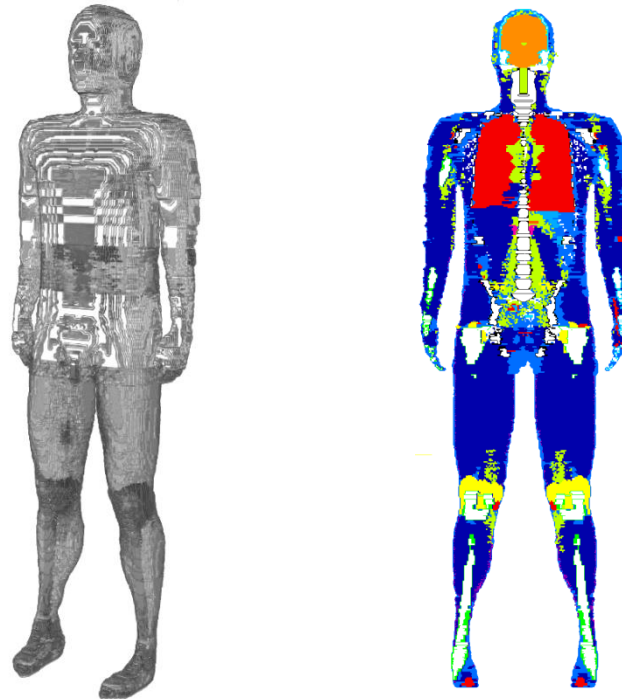
Figure 5.2: Max-06 voxel phantom perspective view of the phantom surface and coronal cut view of the phantom internal structure.

At the National Research Center for Environment and Health (GSF) the same group that developed one of the first voxels phantoms in 2002 completed a family of 10 phantoms covering ages from 8 weeks to 48 years through the use of CT imaging (Petoussi-Henss, Zankl et al. 2002). At this time it was one of the most complete groups and it followed a strategy called "PSI" (precisely segmented individuals). This strategy aimed to build phantoms of various age groups, to calculate conversion coefficients for each age group as well as to assess the variation due to individual anatomy (Petoussi-Henss, Zankl et al. 2002). From these models the Baby phantom and the Child phantoms stand out since they are the first non-adult voxel phantoms (Zankl, Veit et al. 1988). As the mathematical models from Cristy and Eckerman (1987) these models reflect the increase in medical exposure to younger members of the society and the need to assess their exposure. This concern led to the construction of other phantoms such as the 14 year old female phantom Adelaide developed by Caon, Bibbo et al. (1999) and a series of paediatric models at ages between one and fourteen years that were developed by Bolch et al. at the University of Florida (Lee, Williams et al. 2005).
Parallel to this development in the 2000's several phantoms based on Asian individual dimensions were developed by research groups in Japan, China and Korea (Zankl 2007), in contrast to the all previous mentioned phantom that were based on Caucasian individuals.

Due to the new ICRP-89 (2002) collection of data for anatomical values, many phantoms were resized to match the new reference values, such as the MAX-06 (see Figure 5.2) and FAX-06 that have been created and modified by Kramer, Khoury et al. (2006) and the new

version of NORMAN, called NORMAN 5 (Ferrari and Gualdrini 2005). However, it was the "Golem" and "Laura" phantoms both developed at the GSF by Zankl and co-workers and later modified (Zankl, Eckerman et al. 2007) that in 2009 have become the current ICRP computational reference models (ICRP 2009).

5.1.3 BREP phantoms

The Boundary Representation phantoms (BREP) or also know as Hybrid phantoms are the current state-of-the-art phantoms. These phantoms use non uniform rational B-splices equations (NURBS) or polygonal meshes to represent the surfaces limits. Despite the fact that their nature is mathematical, as the stylized phantoms, these new methods of representation allow to represent the complex human anatomical surfaces (Xu and Eckerman 2010) thanks to the great number of operation tools available such was extrusion, chamfering, blending, drafting shelling and tweaking. Note that with the mathematical phantoms only Boolean operators are used. BREP phantoms are also very flexible and suited for surface deformations; this feature allows them to be used in the 4D simulation of organ movement such as the heart motion or in the complete phantom movement (Segars 2001, Xu and Shi 2005, Segars and Tsui 2009, Xu and Eckerman 2010). For the construction dedicated software programs are used to define the NURBS or mesh surfaces from human tomography images. This allows them to have the anatomical realism of the voxel phantoms. From this combination of mathematical methods and tomography imaging, comes the hybrid definition (Bolch, Lee et al. 2010).

The BREP methods were firstly developed in the 1970's. However, only in 2001 they were applied to the development of phantoms. Pioneer work has been done by Segars (2001) in his PhD thesis: he used NURBS to develop a Cardiac-Torso phantom, called NCAT, and later introduced movement to simulate the cardiac and respiratory movements (Segars 2001, Xu and Eckerman 2010). Shortly afterwards, the NCAT was once again modified, this time to create two whole body phantoms representing a male and a female anatomy, the XCAT phantom (Segars and Tsui 2009).

This new revolution in the phantom development was followed by Xu et al. in 2005, who used the same methods as (Segars 2001) to develop a 4D chest phantom based on the VIP-man phantom that was previously developed also by this group (Xu and Shi 2005). Later Xu, Taranenko et al. (2007) used polygon meshes to develop several phantoms of pregnant women in different gestation periods, and in 2008 adult male and female phantoms (Xu, Zhang et al. 2008). Parallel to this work a new family of phantoms was developed with members raging from newborn to male and female adult, see Figure 5.3 (Bolch, Lee et al. 2010).
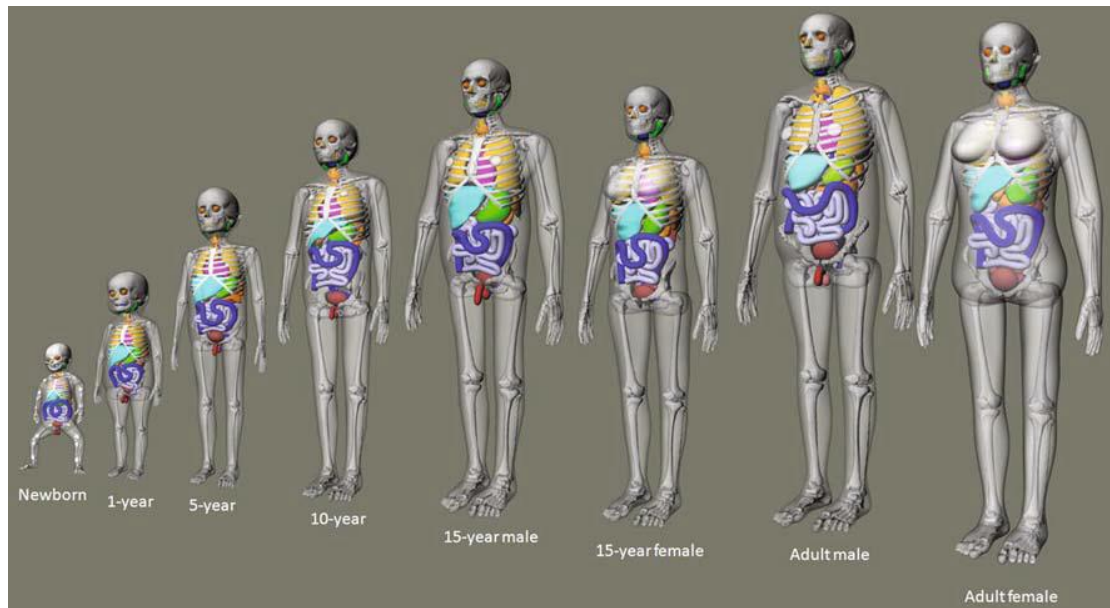
Figure 5.3: Family of BREP phantoms develop at the University of Florida by Bolch, Lee et al. (2010)

Since 2008 the use and development of this type of phantoms has significantly increased, since they present significant advantages compared to the voxel phantoms, such as the elimination of the typical stair stepped artefacts present in the voxel phantoms due to the image slice resolution thickness, the ability to model small organs and the high flexibility that allows them to be modified to patient specific dimensions or in the development of phantom libraries.

The main limitation to the use of these phantoms is in the inability to handle this new format by the majority available of the Monte Carlo codes (including the state-of-the-art MCNP6 released in 2012) and in the high computational power required to perform simulation of particle transport in these phantoms. As shown by Kim, Jeong et al. (2011) organs dose calculations using the GEANT4 Monte Carlo code and the PSRK-Man mesh phantom required 70 to 150 more time than those using the equivalent voxel phantom. Thus the usual practice is the use of a dedicated software to convert the BREP phantom to a voxel phantom. Despite the fact that the new voxel resolution can be selected arbitrarily, this generally reintroduces the voxel limitation in the definition of small structures.

Due to the previously mentioned limitations concerning the use of BREP phantoms, two voxel models were used in this work.

5.2 Phantoms used in this work

The computational models used in this work belong to the voxel phantom type. Voxel phantoms were firstly used for the calibration of body counters by Mallett, Hickman et al. (1995). Using MR images of a human subject, they constructed a torso phantom in order to develop an "individual-specific" calibration for lung counting and improve the activity estimation for gamma energies below 100 keV. Shortly after that, Ishikawa and Uchiyama (1997) developed a voxel phantom based on the BOMAB and the MIRD phantom geometries to study the impact for ^{137}Cs whole body counting of the BOMAB phantom uniform density approach and the size impact on the detection efficiency (Ishikawa and Uchiyama 1997). Since then the use has significantly increased in all types of *in-vivo* counting geometries.

Concerning skull measurements, the first use of voxels phantoms was done using the NORMAN phantom by Hunt, Malátová et al. (1999). However, only 5 years later (2004) the VOXELMAN phantom developed by Zubal, Harrell et al. (1994) was used at CIEMAT to optimize the counting geometry of their partial body counter (Moraleda, Gómez-Ros et al. 2004, Ros, Moraleda et al. 2007). Later Gualdrini, Daffara et al. (2005) developed and used the corresponding head voxel phantom to verify the activity uniformity of the Alderson ENEA skull phantom (Gualdrini, Battisti et al. 2000).

Since 2007 Vrba (2007) has developed and used three voxel phantoms of human heads: two based on CT images from the USTUR phantom and the BfS phantom, the third phantom was based on the CT images of a 38 old woman. Using these phantoms he studied the impact of several critical parameters such as the head size and the head shape on the detection efficiency, for his body counter.

Recently Vrba has coordinated a EURADOS Monte Carlo intercomparison exercise using voxel phantoms of the head used for the EURADOS skull measurements intercomparison, see Chapter 3. This exercise was divided into 3 tasks: the first consisted in the simulation of the HMGU detector 3 and the CSR voxel phantom; the second in the simulation of one of the intercomparison participant's own detector and the USTUR case 102 and BfS voxel phantoms; and the third in the simulation of several detectors in a hypothetical counting geometry and the BfS voxel phantom. The main results from this intercomparison are currently in the process of being published; the results from task one show a good agreement between the solutions of the intercomparison problem provided by the participants (Vrba, Nogueira et al. 2013).

In the present work two voxel phantoms were used: the USTUR case 102 skull voxel phantom developed by Vrba (2010a) and the Max-06 voxel phantom developed by Kramer, Khoury et al. (2006). The first phantom was used initially to validate the implementation of the voxel phantom in the Monte Carlo simulations by comparing the simulated results directly with the measurement results; additionally the unique natural activity distribution pattern in the bone surface of the Case 102 phantom was studied also using this voxel phantom.

The second phantom was used due to the limitations of the USTUR case 102 voxel model to represent a real human scalp thickness. Additionally specific features of this phantom deviate from human anatomy, e.g. an incomplete fill of the brain region and a sagittal cut on the skull bone. Since one of the purposes of using this phantom was studying the influence of the scalp thickness, a high resolution phantom was needed and unfortunately the current ICRP-110 (2009) reference model's resolution is not ideal for this studies. From the several available voxel phantoms the Max-06 showed to be the best since it has a high resolution, it was adjusted to the ICRP reference man values and its skeleton was prepared for skeleton dosimetry. In the following, details of the two phantoms are given.

5.2.1 USTUR case 102 voxel phantom

The USTUR voxel phantom used in the present work was created by Vrba (2010a), based on the data provided by a CT study previously performed (Tabatadze, Brey et al. 2008).
This phantom had originally a resolution of $204 \times 228 \times 184$ (X, Y, Z) voxels with size 0.95 mm $\times$ 0.95 mm $\times$ 1.25 mm (Vrba 2010a). However in the frame of an EURADOS intercomparison this phantom resolution was modified to $203 \times 226 \times 184$ (X, Y, Z) voxels with size 0.949218 mm $\times$ 0.949218 mm $\times$ 1.25 mm.
The segmentation was performed by threshold of the CT numbers (grey values) and manual correction (Vrba 2010a). In this process three regions of the phantom soft tissue equivalent material were distinguished in terms of density. The cortical and trabecular bone were also segmented, however the "anatomical accuracy of this distinction is limited" (Vrba 2010a).

As can be seen in Figure 5.4, the CT images of this phantom reveal several anatomical inaccuracies of the voxel phantom: the dimensions of the internal structures of the two halves do not fit well together, so that there are sharp intersections of bone and soft tissue at the boundary of the two halves; the skull sagittal between the skulls is not align with the soft tissue reconstructed head; the scalp thickness has several inconsistencies and the inside of the phantom is not completely filled and consequently there are air bobbles in the brain region.
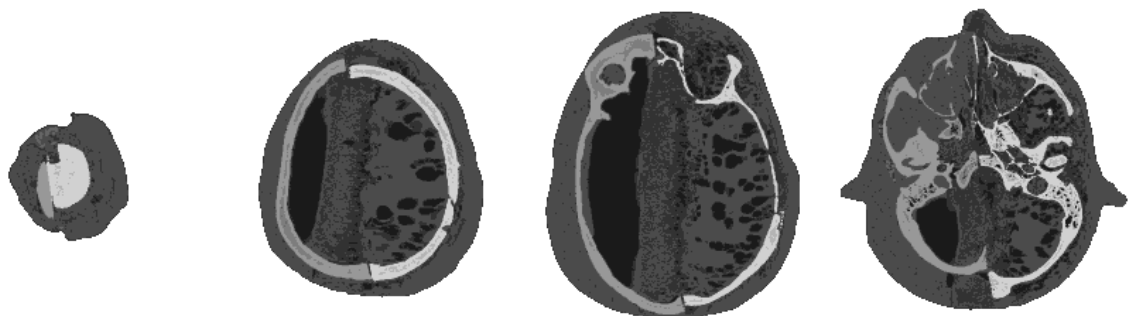
Figure 5.4: USTUR case 102 voxel phantom transverse cross-section views, from top to bottom. Note that the case 102 bone is on the right side of the head and that in black one can see the incomplete filling of the phantom inside.

5.2.2 Max-06 voxel phantom

The MAX-06 phantom is a male whole body phantom developed by Kramer, Khoury et al. (2006) based on the original CT data from the Zubal phantom (Zubal, Harrell et al. 1994). This phantom was newly segmented based on the CT numbers to include more organs and adjust the organ volumes to the ICRP 89 (ICRP-89 2002) reference man (Kramer, Khoury et al. 2006).
Kramer, Khoury et al. (2006) with the intention of using this phantom for "advance skeletal dosimetry", has segmented the cortical bone, spongiosa (trabecular and respective soft tissue), cartilage and medullar yellow bone marrow based on the original CT data, anatomical images

and cryosection images from the Visible Human Project (Spitzer, Whitlock et al. 1998, Kramer, Khoury et al. 2006). Due to this anatomical accuracy, this phantom was used to in the present work to study the influence in the detection efficiency of the ^{241}Am distribution in the cortical bone and trabecular bone, see Chapter 6.

The Max-06 phantom has a high resolution of $474 \times 222 \times 1461$ (X, Y, Z) voxels with size 1.2 mm $\times$ 1.2 mm $\times$ 1.2 mm, which makes it one of the most detailed whole body voxel phantoms available. This fine resolution also allows a good definition of the phantom skin and head scalp. Due to this reason the Max-06 phantom was used in this work to study the influence of the scalp thickness on the detection efficiency.

The Max-06 head phantom tissue compositions and densities were originally defined according to the ICRU 44 data (ICRU-44 1989). However, in the present work they were defined according to the tissue compositions of the ICRP adult reference computational model (ICRP-110 2009) which are based on ICRU-46 (1992), however have the novelty of taking into account the tissue blood content.

Finally, to optimize the computational time, the model size was reduced by the removal of the body voxels using the image processing program Image J version 1.44p, so that only the head and complete neck remained (top 212 slices). Also unnecessary voxels corresponding to the air were removed. This optimization of the Max-06 for skull calibration purposes will be referred in this work as Max-06 head phantom, see Figure 5.5.
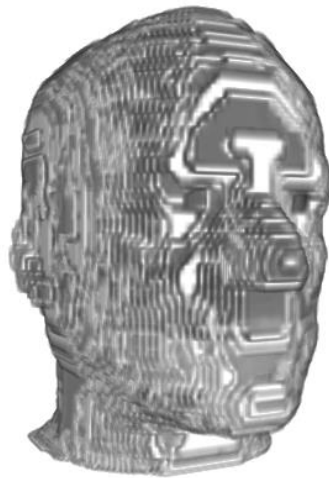
Figure 5.5: External surface of the Max-06 head phantom optimized in the present work. Visualisation with the 3D viewer plug-in of the image processing program Image-J.

5.3 Results and Validation

The USTUR case 102 voxel phantom geometry was implemented in GEANT4 using the G4PhantomParameterization, as demonstrated by Garny (2009). The voxel geometry implementation was then validated by comparison with similar MCNPX calculations and with results of measurements: Detector 3 was positioned above the USTUR case 102 phantom at 1 cm distance from the previously defined position 0, see Chapter 3.
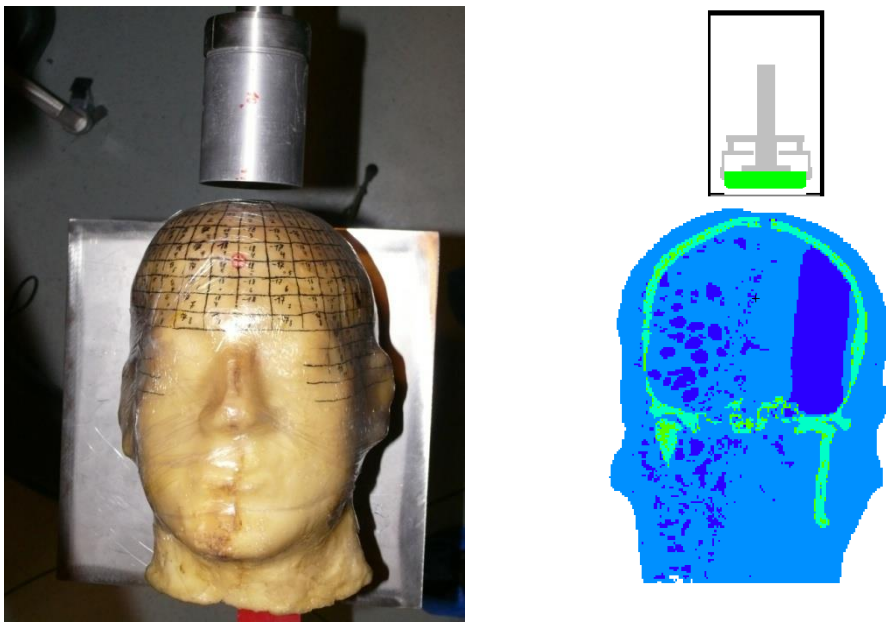
Figure 5.6: Counting geometry for USTUR case 102 phantom using detector 3, and coronal cross section view of the respective computational set-up in MCNPX and GEANT4

As can be seen in Figure 5.7 there is a good agreement between the measured and simulated spectra. For the 59.54 keV full energy peak there is a relative deviation of approximately 4% between simulations and measurement, for the 26.34 keV full energy peak GEANT4 has a relative deviation of 6% while MCNPX has a relative deviation of 9%. Note that the simulation full energy peak results are calculated from the values obtained before the Gaussian broadening algorithm application, see Chapter 4.

For the Compton region below 59.54 the simulations show in general more counts that the measurement. This is probably due to the fact than the elemental compositions of the phantom materials and the activity distribution are not exactly known, and assumptions of these physical parameters had to be made in the simulations.

As previously observed in the Monte Carlo simulations of a [241]Am point source (Chapter 4), for energies above 62.0 keV only measurement counts are present. This is due to the pile-up effect that is only observed in the experimental measurements, see Chapter 4.

The relative deviation between GEANT4 and MCNPX for the 26.34 keV and 59.54 keV full energy peaks is below 3% and 1%, respectively.
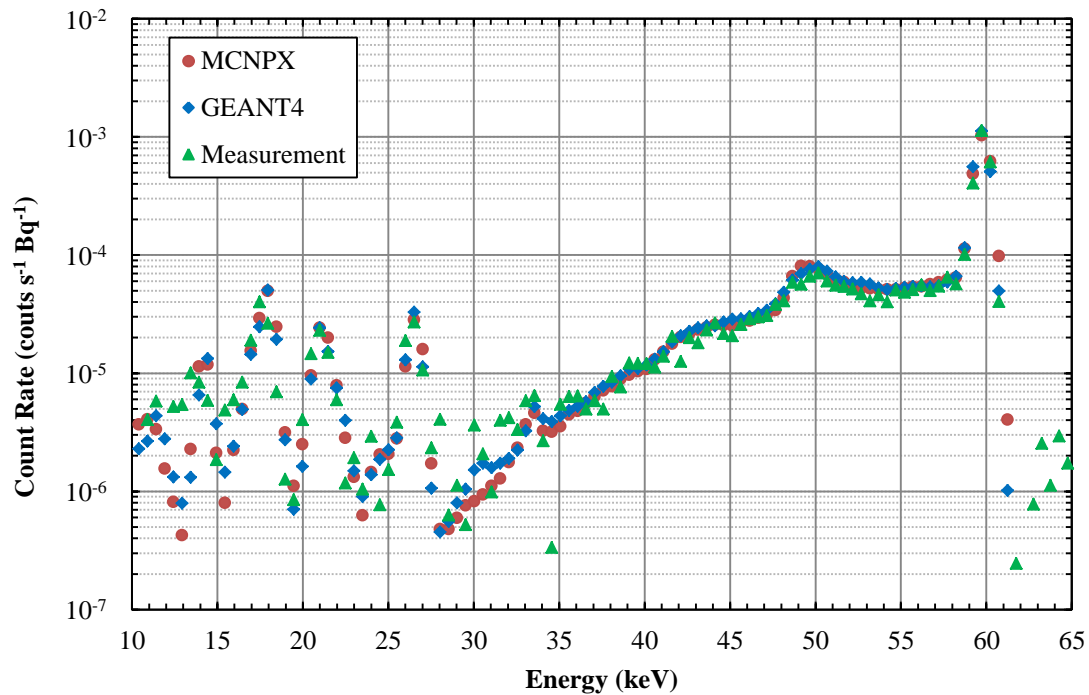
Figure 5.7: USTUR phantom detector 3, top position: results of measurement and corresponding simulation results. The uncertainty values are smaller than the symbols.

Having validated the computational set-up of the USTUR case 102 voxel phantom in both GEANT4 and MCNPX, the Max-06 head was implemented in GEANT4 and in MCNPX for further validation. Detector 3 was placed at 1 cm distance perpendicular to the right side of the phantom, see Figure 5.8.
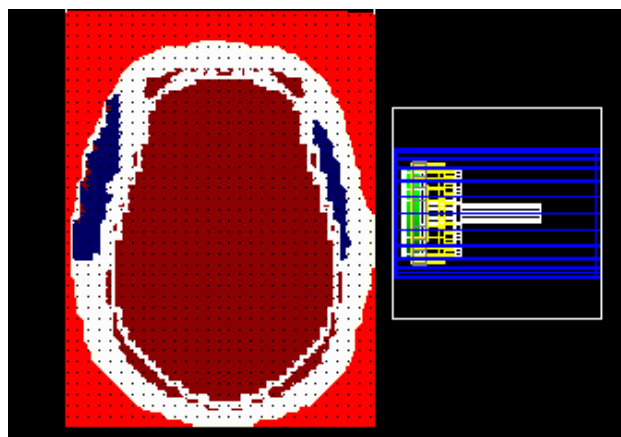
Figure 5.8: Transverse cross-section view of the HMGU detector 3 and Max-06 head voxel phantom as used in GEANT4.

In Figure 5.9, one can observe that there is again an excellent agreement between both calculations: for the 59.54 keV full energy peak, there is a relative deviation below 1% and for the 26.34 keV full energy peak, there is a relative deviation below 2%. In the Compton region, there are small deviations between the calculations which are more prominent for lower energies; this is probably due to the different cross-sections and different algorithms for the electron transport used in GEANT4 and MCNPX.
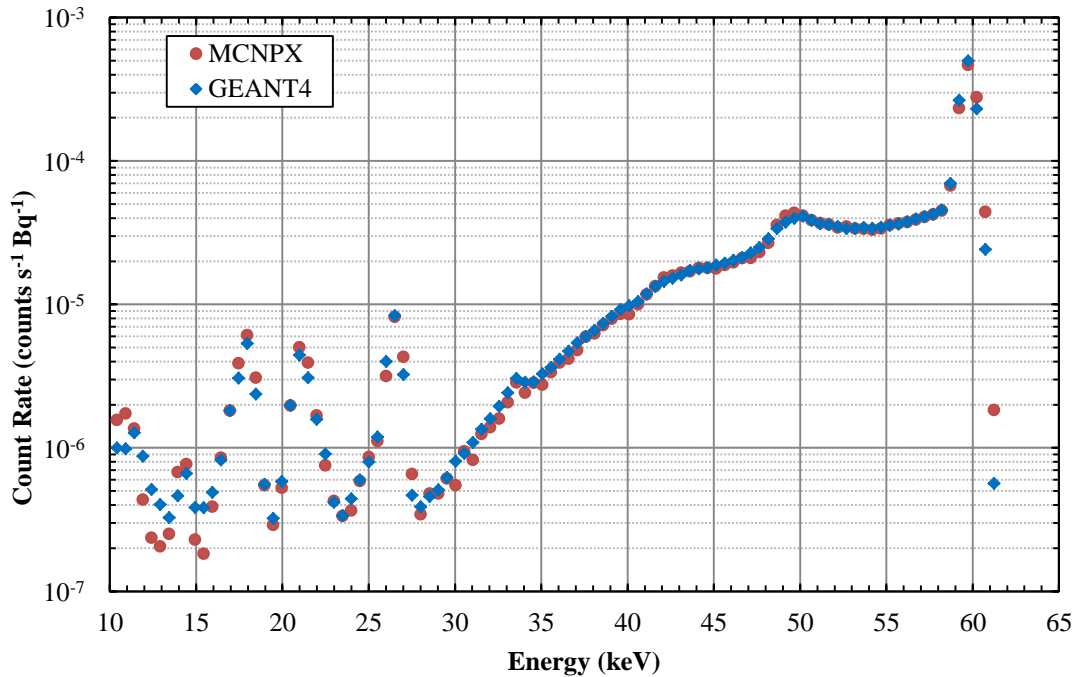
Figure 5.9: Results for detector 3 and the Max-06 skull phantom obtained with Geant4 and MCNPX.

5.4 Conclusion

In agreement with the results shown in Chapter 4, it was demonstrated that Monte Carlo methods allow to reproduce the experimental measurements results in all aspects, with exception of the pile-up effect above 62 keV. Excellent agreement with relative differences below 4% and 10% for the 59.54 keV and 26.34 keV full energy peaks was found between both Monte Carlo codes and the experimental results using the HMGU detector 3 and the USTUR case 102 phantom. Subsequently, the Max-06 phantom was also implemented in GEANT 4 using the same method. Since no experimental results are available for this phantom, the validation was performed by comparing with MCNPX calculations in identical conditions. Once again, excellent results with relative differences below 1% and 2% for the 59.54 keV and 26.34 keV were found.

6 Person-specific parameters and detection efficiency

One of the advantages of the direct measurements (*in-vivo*) of bone seeking radionuclides in the human skull is the reduced variability typical between different individuals (Cohen, Spitz et al. 1977).
Despite this advantage, in the first international intercomparison from partial and whole body counting for skull measurements, Rühm, König et al. (1998) observed differences up to 60% between different laboratories and concluded that future work should focus on the assessment of the activity when using different calibration phantoms and on the impact of characteristics such as the skull size and differences between artificial [241]Am labelling and the natural incorporation in the bone matrix.

The use of physical anthropomorphic phantoms is very limited since they are difficult and expensive to build. Also the commercially available phantoms are generally built to represent a reference human body. Despite the fact that some of these phantoms (e.g. LLNL torso phantom) provide some features to simulate different critical body characteristics, the application of these phantoms' calibration coefficients requires extrapolations and correction factors if they are to be applied to a specific individual (due to differences e.g. size), which makes the complete process extremely time-consuming.

The necessity to extrapolate correction factors increase proportionally to the decrease of the photon energy to be detected. This is particularly true for energies below 100 keV, since these photons are significantly attenuated by the human body (Mallett, Hickman et al. 1995).

Mallett, Hickman et al. (1995) revolutionized the calibration methods for *in-vivo* counting with the use of voxel models to develop an "individual-specific" calibration for lung counting. For this they used MRI to build an "individual-specific" phantom from a human subject. With this method they were not only able to represent the individual geometry but also able to include information on terms of fat and water location. Due to limitations in the computational power and on the Monte Carlo code used (MCNP4), however, the number of voxel needed to be reduced to one hundred thousand voxels at the time.

Thanks to the developments in computer technology the voxel phantoms can nowadays be composed by several millions of voxels which allows a very fine resolution and a more detailed anatomical representation than the use of physical phantoms. They have also the advantage to be flexible in terms of their dimensions, composition and shape; this allows the user to adjust the voxel phantom to the measured subject characteristics such as size, weight and shape.

Despite the voxel phantoms' flexibility compared with the new generation of computational phantoms, the BREP phantoms (Boundary Representation phantoms), they are currently considered limited and their construction and modification time consuming. The state of the art BREP phantoms provide the flexibility of the mathematical phantoms, but since they are constructed from tomography images they allow to maintain the anatomical realism of the voxel phantoms, from this comes the definition hybrid (Bolch, Lee et al. 2010). Using the appropriate software not only the external dimensions but also the shapes can be easily changed. However, such modifications require a depth knowledge of the human anatomy to maintain the anatomical realism (Hegenbart 2009).

However, even with the BREP phantom flexibility the development of "individual-specific" phantoms (a phantom that perfectly matches an individual's external and internal dimensions

and shapes), is a time consuming process and requires a good expertise on some dedicated software for their modification. Currently the best approach to this problem has been the development of phantom libraries that represent the majority of anatomical variability of critical body parameters such as body mass and shape; examples of these libraries are the GSF voxel phantom family (Petoussi-Henss, Zankl et al. 2002), the University of Florida phantom reference hybrid family (Bolch, Lee et al. 2010) and the IRSN library of female cup sizes, chest girths and organs volumes (Farah, Broggio et al. 2011). Having these phantoms available, the phantom most approximate to the measured individual, in terms of external dimensions or other parameters, is then used to provide the required calibration factor. Depending on the number of phantoms available and on the measured individual morphology, generally some additional efficiency correction factors will still be necessary to generate an "individual-specific" calibration.

The flexibility of computational phantoms can also be used to study and calculate correction factors for critical body parameters, which can be used to correct calibration factors obtained with physical computational phantoms and ultimately provide an "individual-specific" calibration. Additionally they can also be used to provide estimations on the unknown impact of certain parameters on the detection efficiency, such as the activity distribution in the bone surface.

Due to computational limitations on the simulated particles' transport in a Mesh surfaces defined geometry, currently for most of Monte Carlo codes the BREP phantoms need to be converted to equivalent voxel phantoms. Due to this limitation and the profound expertise required to handle and modify BREP phantoms, in the present work the modifications were performed directly in the voxel phantoms geometry using the image processing program ImageJ, a dedicated C++ algorithm and modification of the voxel sizes. Using these modified phantoms the activity distribution, scalp thickness, skull size and shape influence in the detection efficiency for skull measurement were studied.

6.1 Activity distribution

The activity distribution in the bone is assumed − in agreement with the general practice for radiation protection purposes − as homogeneous despite of studies that reveal that differences in the distribution exist due to bone remodeling, calcification and bone resorption (Hickman and Cohen 1988).

In the past several studies that have addressed the impact of ^{241}Am distribution in the skull bones on the detection efficiency: Malátová and Foltánová (2000) used the NRPI phantom to simulate inhomogeneous distributions by changing at specific sites the activity of the planar sources used by the NRPI phantom. Vrba (2007) used the Monte Carlo code MCNPX and a voxel phantom developed by him, based on the CT images of a 38 years old women, to study the influence of the unknown activity distribution on artificially contaminated phantoms since in these phantoms the activity is located only at the inside and outside of the bone surface, and showed that efficiencies were up to approximately 20% higher compared to the assumption of a homogeneous activity distribution in the bone volume. Later Vrba (2010a) pointed to the inhomogeneous activity distribution present in the Case 102 skull phantom, due to bone remodeling. He concluded, however that due to the uncertainty of the detectors positioning and based on radiochemical data (McInroy, Boyd et al. 1985) which is given in terms of activity per wet tissue mass of 11 bone regions of the skull, that a homogeneous activity distribution is a good approach to simulate the complex but incompletely defined activity distribution provided by the radiochemical analyses data available for the Case 102 skull bone.

In this chapter the influence of two aspects on the detection efficiency were studied: the first was the ^{241}Am distribution in the bone surface of the case 102 skull that was measured by Hickman and Cohen (1988) which provides a better picture of the activity distribution compared to the radiochemical data. The second aspect was the ^{241}Am distribution in the cortical bone and trabecular bone as a function of time that was studied based on the ICRP biokinetic model for ^{241}Am modeling and on the Max-06 phantom to take advantage of the high anatomical accuracy on the skeleton definition, see Chapter 5.

6.1.1 Case 102 activity distribution pattern

The USTUR case 102 skull phantom is a unique phantom as it is based on a real human case with an accidental natural ^{241}Am contamination of the bone matrix. As the exposure occurred 25 years before the death of the donor, it can be assumed that bone remodeling has happened since the skull bones have 1.8% mean turnover per year (ICRP-23 1975).

During the construction of the skull phantom extensive measurements were performed to the bone surface, using a small shielded NaI(Ti) detector, so that only the bone surface in direct contact with the detector would be measured (Hickman and Cohen 1988). These measurements allowed Hickman and Cohen to create a map of the counts per minute equivalent to the activity distribution pattern in the skull bone surface, see Figure 6.1. To study the influence of this activity distribution pattern in the detection efficiency a computational set-up was developed in the present work using Monte Carlo methods, the voxel phantom of the USTUR phantom (Vrba 2010a) and the real activity distribution pattern of the USTUR phantom.
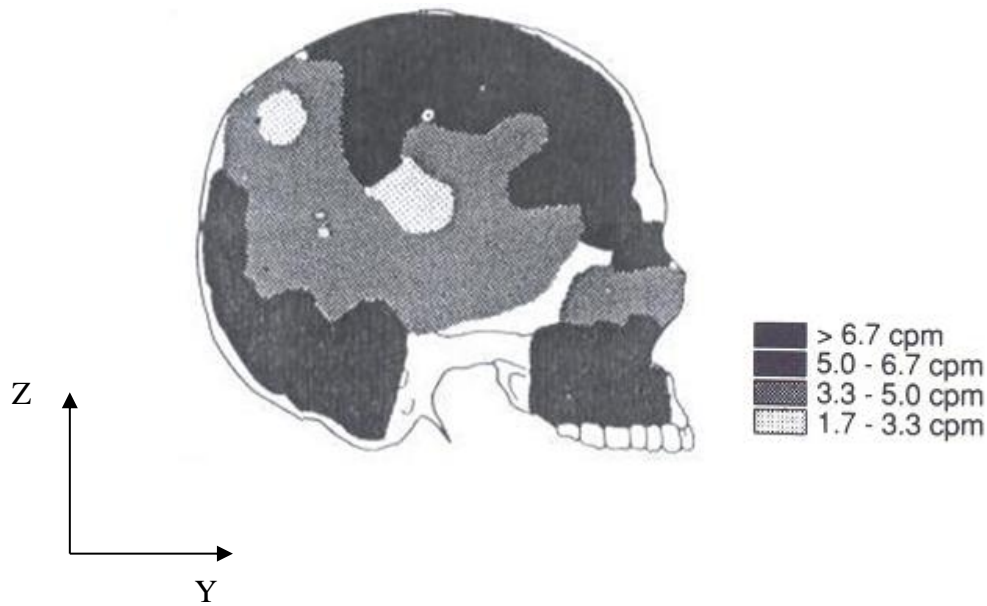
Figure 6.1: Lateral activity distribution pattern measured in the skull of USTUR case 102 (Hickman and Cohen 1988).

To implement the activity pattern in the Monte Carlo simulations, Figure 6.1 was digitalized with a standard office scanner and the number of pixels was adjusted to the voxel phantom number of voxels in the YZ plane. In the original figure four activity concentration intervals were defined. However, because it was not possible to distinguish more than three regions, only three regions were painted over the original image, see Figure 6.2. This new image was then converted in a two dimensions matrix in which the values correspond to the image colours. A C++ algorithm was then developed to use this matrix, in order to assign the source voxels in three different regions based on their coordinates in the YZ plane.
Finally, to simulate the different concentrations of ^{241}Am the Monte Carlo source probability was modified so that voxels from regions with more ^{241}Am concentration are more probable to be the origin of a gamma emission.
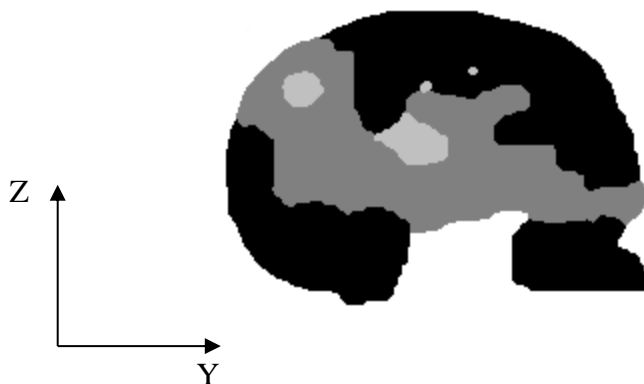
Figure 6.2: Activity distribution painted and used here for the activity distribution pattern implementation in the Monte Carlo simulations.

6.1.1.1 Results

To determine the counting geometries for which the assumption of a homogeneous activity distribution in the skull bones can provide a correct value, the following hypothesis was formulated. With the increase of the distance between detector and phantom, the phantom surface area measured increases, resulting in a smaller influence of the activity distribution pattern in the detection efficiency, see Figure 6.3.
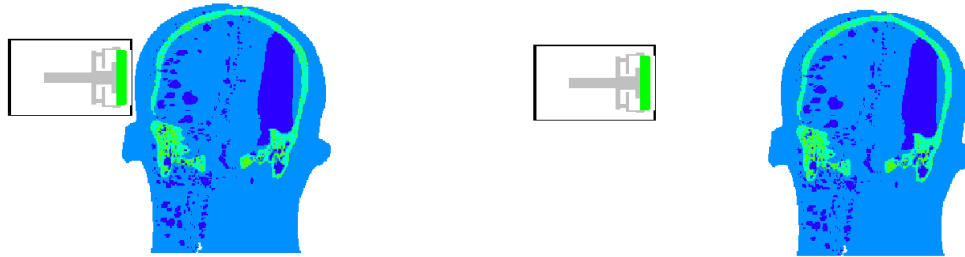
Figure 6.3: Measurement geometry for detector 3 at 0 cm and 10 cm distance from the USTUR case 102 skull phantom surface (Nogueira, Rühm et al. 2012).

Simulations were performed both for the homogeneous activity distribution and for the activity distribution shown in Figure 6.2; in both cases detector 3 was simulated at different distances from the voxel phantom surface. Comparing the efficiencies obtained at 59.54 keV in terms of the relative deviation from each other, as expected the deviation progressively decreases with increasing distance. For 0 mm distance the relative deviation is approximately 9%, while for 150 mm is approximately 3.6%, and at 600 mm it is only 1.7%, see Figure 6.4. Another effect of the distance increase is the decrease of detection efficiency due to the change in solid angle, which amounted to a decrease of approximately 1% per mm in the detection efficiency. Since in partial body counting generally very low activities are to be measured, the ideal positioning is not always viable and a compromise needs to be found between distance and the activity distribution influence.

As the activity distribution in the bone surface is generally an unknown parameter, its influence is usually taken into account in the measurement uncertainty budget. Guidelines as the European project IDEAS (Doerfel and Karlsruhe 2006) suggest a typical uncertainty of 5% for the variation of activity distribution. The present results obtained suggest that for skull measurements this uncertainty is higher for short distance measurements and reach about 9% close to the surface. However, note that this influence will also depend on the number of detectors used or positions measured and that the average or sum of the measurements result will reduce the influence of the activity distribution on counting efficiency influence.
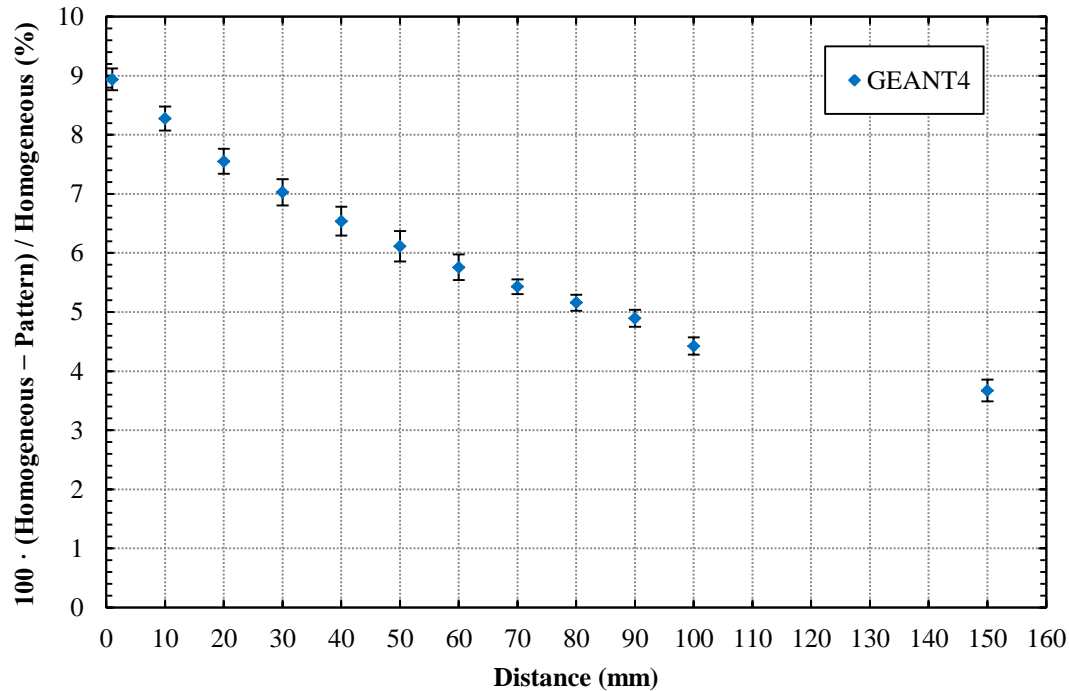
Figure 6.4: Relative deviation (%) between detector 3 efficiency at 59.5 keV calculated for a homogeneous activity distribution and USTUR case 102 activity distribution (Figure 6.2). One-sigma uncertainty calculated from the Monte Carlo statistical uncertainty is displayed.

6.1.1.2 Conclusion

The influence of the [241]Am activity distribution in the bone surface was studied, in order to determine the counting geometries for which the assumption of a homogeneous activity distribution in the skull bones can provide a correct value of the skeletal burden and thus ultimately allowing the proper use of skull voxel phantoms for the mathematical calibration of PBC detection systems. As ideal positioning is in most of the cases not possible, a compromise should be found and the influence of activity distribution on counter calibration should be taken into account in the measurement uncertainty budget.

For the distance generally used in this work, i.e. 1cm, the uncertainty obtained here is about 8%. Note that this number depends on photon energy. Thus the number of 8% obtained here is only valid for case 102 at 59.54 keV. Nevertheless it may provide an idea on the order of magnitude, an unknown activity distribution pattern will contribute to the total uncertainty.

6.1.2 Cortical bone and Trabecular bone activity distribution

Skull bones are generally composed of two types of bone: the compact or cortical bone and the trabecular bone which is the osseous tissue part from the spongiosa ("trabecular bone and its supported soft tissue") (ICRP-70 1995). Cortical bone shows only few pores and is generally found on the external surface of the bones. In contrast, the trabecular bone is found in the inside of the bone. Its structure is porous and delineates spaces that are filled with hemopoietic tissues that produce the red blood cells (Shipman, Walker et al. 1985).
In terms of mass the cortical bone represents 95% of the bone of the skull, while the trabecular bone only represents 5% (Johnson 1964). Despite this the trabecular bone and its supported soft tissue represents a big part of the bone volume. For example, in the Max 06 head phantom used in this work, from the total number of voxels representing the skull bone 45% are attributed to spongiosa.

The activity retention is also different in cortical and trabecular bones. Biokinetic modelling using the actual ICRP model (Noßke 2013) shows that in the first years after an internal contamination the cortical and trabecular bones have approximately the same activity content, see Figure 6.5. Three year after the contamination the values start to differ and at approximately six years the activity in the cortical bone is twice as high as the activity in the trabecular bone, see Figure 6.6. These values were calculated for the ingestion of one Becquerel of [241]Am, however, in the case of an inhalation of [241]Am a similar behaviour is expected (Noßke 2013).

Figure 6.5: Retention curves for cortical bone and trabecular bone calculated according to ICRP model for the ingestion of one Becquerel of [241]Am (Noßke 2013).

Figure 6.6: Ratio of cortical to trabecular bone as a function of time since incorporation, based on retention curves for cortical bone and trabecular bone calculated according to the actual ICRP model for the ingestion of one Becquerel of [241]Am (Noßke 2013).

6.1.2.1 Results

To study the influence on the detector efficiency of a different activity of [241]Am in the cortical and trabecular bone, the Max-06 head phantom was used, due to two reasons: first Kramer and Hauck (2006) have prepared this phantom for skeletal dosimetry with the segmentation of the cortical bone, spongiosa, cartilage and medullar yellow bone marrow based on the original CT data, anatomical images and cryosection images from the Visible Human Project; second according to Vrba (2010a), for the USTUR case 102 voxel phantom the "anatomical accuracy" between the cortical and trabecular bone distinction is limited.

In this context, the use of voxel phantoms represents a disadvantage since, due to the limited voxel size resolution, an independent representation of the trabecular bone structure and the supported soft tissue is not possible. Therefore in this study the spongiosa voxels were considered made of trabecular bone. Two simulations were performed, one where the cortical bone and the spongiosa are equally contaminated, the other where only the cortical bone is contaminated. The head of the Max-06 phantom consists of 306796 voxels representing the cortical bone and 252475 voxels representing the spongiosa; as previously mentioned this means that the spongiosa is 45% of the voxels representing the bone.
To simulate in GEANT4 and MCNPX the same activity content in the cortical bone and trabecular bone types, it is necessary that both bones have the same number of voxels. Since the number of voxels of different bone is similar no correction was necessary to be introduced in order to simulate the same activity concentration in both bones.

As an approach to phantoms that are only contaminated in the outside and in the inside bone surface, such as the BfS phantom, a simulation was performed were only the cortical bone is contaminated. The initial results show that having only the cortical bone as source results in a 28% higher efficiency for detector 3 at 59.54 keV, see Table 6.1.

Table 6.1: GEANT4 simulation of detector full energy peak efficiency, for Max-06 phantom with different activities in the cortical bone and spongiosa.

Energy (keV)	Full energy peak efficiency			
	Cortical Bone	Uncertainty	Cortical and Trabecular Bone	Uncertainty
59.54	2.709E-3	1.354E-5	2.121E-3	1.687E-5

To study the impact on the detection efficiency due to the variation of the ratio between the cortical and trabecular bone contamination in function of time (see Figure 6.6), simulations were performed where the probability of a gamma emission in the cortical bone was increased and the probability of emission of a gamma in the trabecular bone was maintained in the same ratio as in Figure 6.6. This approach allowed the simulation of the variation of the activity variation in the cortical and trabecular bone in function of the time.

In Figure 6.7 the ratio between the results obtained in function of time and the results obtained when the [241]Am is only present in the cortical bone are shown. The results reveal that the difference between the simulations where only the cortical bone is contaminated and the cortical and trabecular bone are both contaminated decreases with the decrease of the activity in the trabecular bone, however, even after 18000 days (50 years) there is still a 4% difference between the results. From these results can be conclude that contamination of only the cortical bone will provided a reasonably good approach with a relative difference below 10% after 6000 days.
The results shown in Figure 6.7 are the correction factors to correct the BfS efficiency for skull measurements where both cortical bone and trabecular bone are contaminated

The USTUR case 102 donor was internally contaminated with [241]Am approximately 25 years before his death, taking account the ratio between cortical bone and trabecular bone activity biokinetic values and the results obtained for the respective simulation one can conclude that even after 25 years (9000 days) of bone remodelling the [241]Am activity present in the trabecular bone will still influence the detection efficiency. Since the approach that the activity in only in the cortical bone is not fully correct, correction factors were calculated for this phantom by dividing the detection efficiency results obtained in function of time by the detection efficiency obtained for the ratio between cortical and trabecular activity at 9000 days after ingestion from Figure 6.6, see Figure 6.8.

Has an example of the application of the cortical bone trabecular bone activity distribution correction factor (in the present work called K1): if a measured individual is measured 9000 days after the internal contamination the correction factor can be calculated by replacing in the respective phantom equation the X by the number of days after the contamination (for BfS and Max-06 phantom see Figure 6.7 and USTUR case 102 see Figure 6.8), for this example it would be a correction factor of 0.948 for the Max-06 and BfS phantom and a correction factor of 1 for the USTUR case 102.
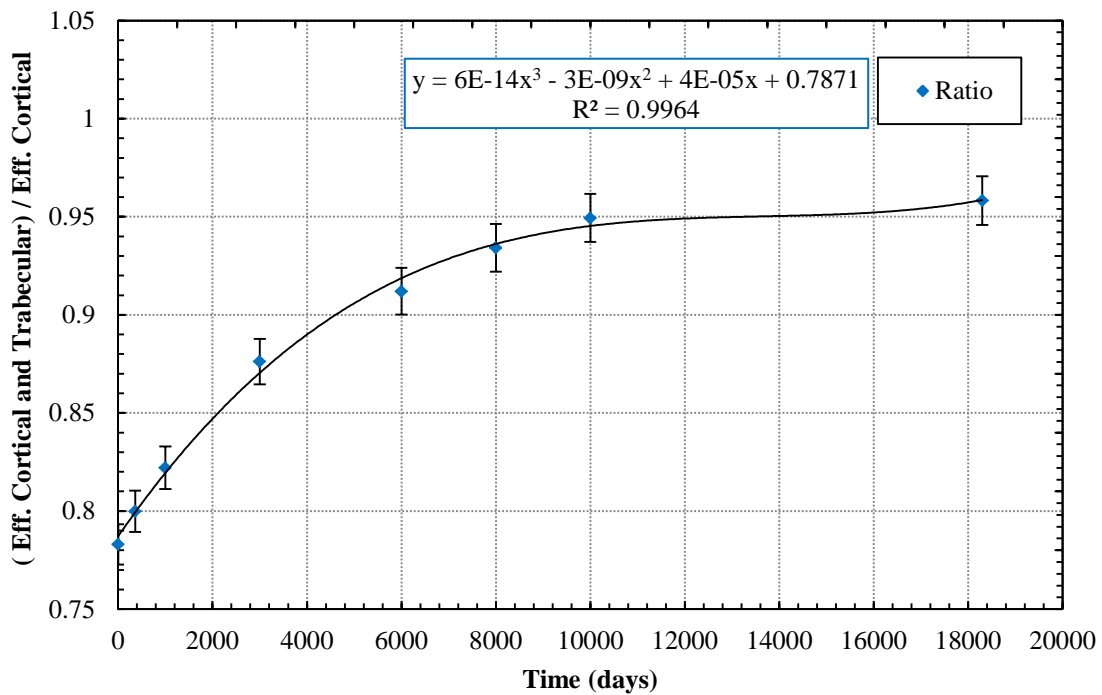
Figure 6.7: K1 correction factors for BfS phantom and Max-06 phantom. Detector 3 efficiency for variation of ratio for cortical bone and trabecular bone together in function of time (see Figure 6.6) divided by the detector efficiency when only cortical bone is contaminated.
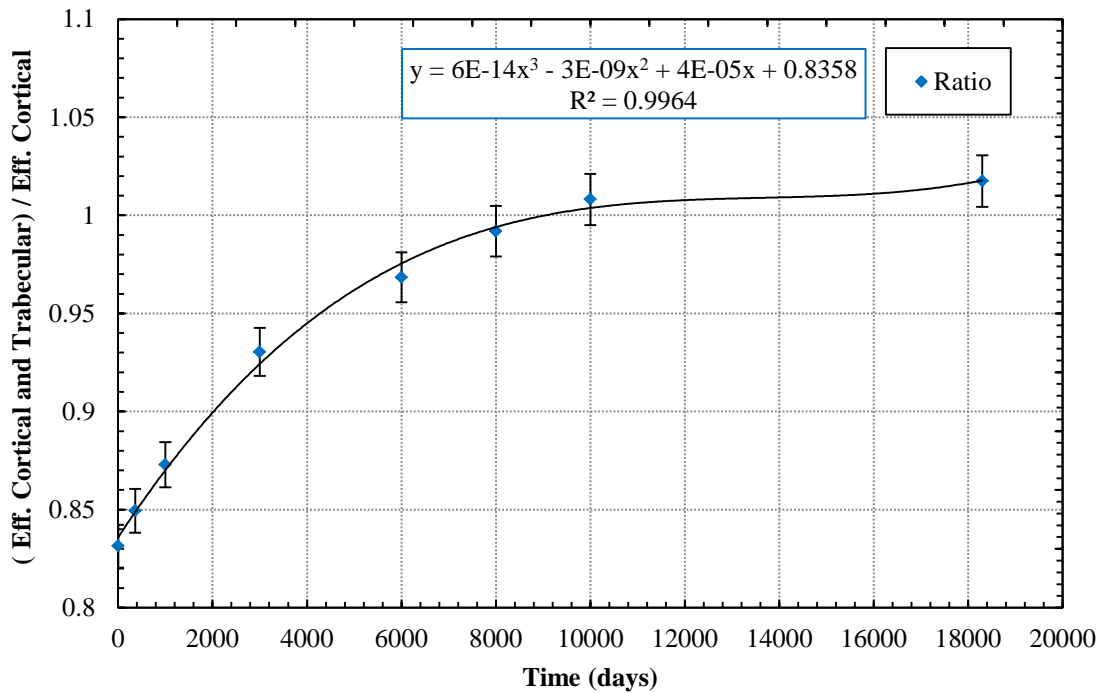
Figure 6.8: K1 correction factors for USTUR case 102 phantom. Detector 3 efficiency for variation of ratio for cortical bone and trabecular bone together in function of time (see Figure 6.6) divided by the detector efficiency for the ratio cortical trabecular after 9000 days.

6.1.2.2 Conclusion

Biokinetic data shows that in the first years after ingestion the cortical and trabecular bones have approximately the same activity content and that approximately three year after the contamination the values start to differ. Using Monte Carlo the ratio between the ^{241}Am present in the cortical bone and the trabecular bone was simulated, to determine the impact of this parameter in the detection efficiency. Based on this correction factors were calculated as a function of the time after the ingestion which can be used directly on the Max-06 phantom, the USTUR case 102, the BfS phantom, or any phantom which contains an artificial contamination of the inner and outer surface of the skull bone.

The biokinetic retention curves used in these work, were calculated by Noßke (2013) for an ingestion, however, similar retention curves would also be obtained in the case of an inhalation.

All simulations in the following work using the Max-06 phantom were performed with the ^{241}Am only present in the cortical bone voxels.

6.2 Scalp thickness

The unknown variation of overlaying soft tissue over the monitored target is one main sources of the uncertainty in *in-vivo* counting. To take into account this issue phantoms such as the Lawrence Livermore torso phantom include various layer of overlaying soft tissue with different thickness (Griffith, Anderson et al. 1978). Skull measurements have the advantage that the scalp thickness has a rather small variability. This was shown by very old different studies conducted between 1883 and 1898, where the tissue thickness over the forehead trichion and forehead middle was measured: the average results from each of the different studies varied between 3.02 mm and 4.3 mm (Shipman, Walker et al. 1985). However, no values are given on the variability within each of the study groups. A more recent study also confirms the relatively small variability of the scalp thickness for individuals from the Southern Urals, were values between 3.5 mm to 6.0 mm of individual scalp thickness were found (König, Wahl et al. 1998). However, no values were found relatively to the variation of the thickness of soft tissue covering the human skull depending on the position e.g. forehead, top of the head and side of the head.

To determine the influence of this parameter on the detection efficiency the Max-06 head phantom was used, since this phantom is based on human CT data and thus represents a realistic description of scalp thickness variation over the skull surface.

6.2.1 MAX-06 head phantom modification

Using the image processing program ImageJ version 1.44p the Max-06 phantom scalp thickness was progressively increased by the addition of a layer of voxels to the outer surface of the voxel model traverse plane. Since the increase of the scalp thickness is due to the increase of adipose tissue, this material was attributed to the new layer of voxels. Although this in not anatomically correct, for internal contamination purposes this approach was considered reasonable. By the addition of voxel layers the original scalp thickness value of the Max-06 phantom of 3.6 mm (measured on the top of the head near the forehead trichion) was increased in steps of 1.2 mm to the extreme value of 10.8 mm, see Figure 6.9.
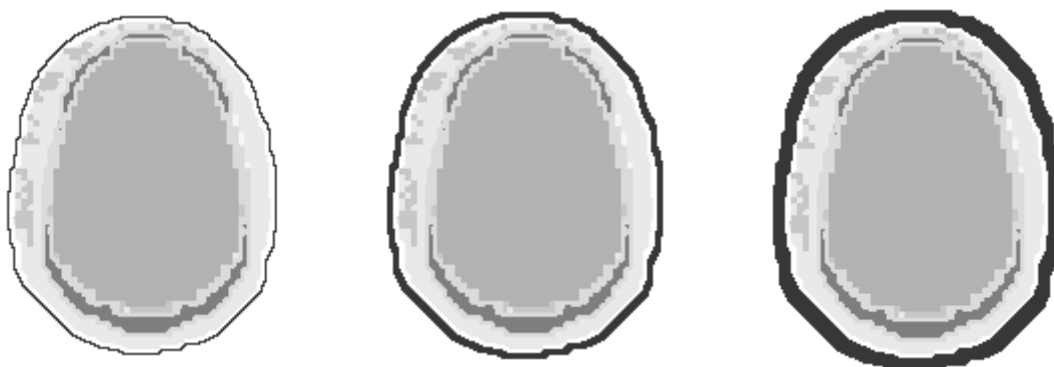
Figure 6.9: Examples of the increase of scalp thickness in Max-06 skull phantom; from left to right additional 1.2 mm, additional 3.6 mm and additional 7.2 mm.

6.2.2 Results

Two different scenarios were considered: in the first the scalp thickness increases and the detector is always positioned at 1 cm distance to the skin surface. This will result in the decrease of the efficiency due to two effects, the increase of the scalp thickness and the increase of the distance between the bone and the detector. To determine the impact of the two effects independently, a second scenario was set were the scalp thickness increases, while the detector remains at the same position which was simulated for the Max-06 phantom with the 3.6 mm original scalp thickness, so that the distance to the bone is constant, see Figure 6.10.
For the interval from 3.6 mm to 6.0 mm, that is approximately what was measured in the individuals from the Southern Urals (König, Wahl et al. 1998), the results for the constant distance show that there is a reduction of 10% in the detection efficiency. From this approximately 7% is due to the increase of the scalp thickness. Thus the increase of the distance has an impact of 3% in the interval from 3.6 mm to 6.0 mm or approximately 1% per mm. This value confirms what was observed previously in the activity distribution calculations using the USTUR voxel phantom, see Chapter 6.
Comparing the results for the worst case scenario of a thickness 10.8 mm with the original Max-06 phantom thickness value 3.6 mm, for the constant distance between the detector and the phantom there is a reduction of 25% in the detection efficiency.

Using the Beer-Lambert law and the 60 keV mass absorption coefficient of adipose tissue (Hubbell and Seltzer 2004), with a density and composition based on ICRU-44 (1989), the theoretical reduction of the number of detected counts and respective detection efficiency due to the increase of adipose thickness was calculated. In Figure 6.10, one can see that this calculation underestimates the reduction of the detection efficiency. Compared with the simulation results for the constant position, for a additional thickness of 3.6 mm and 7.2 mm there is a relative deviation of 3% and 8%, respectively.

The reason of this deviation between the Monte Carlo and the theoretical calculation is a prerequisite of the Beer-Lambert law — the radiation consists of parallel rays crossing the same thickness. In the experimental and simulated case, however, the 59.54 keV photons will not travel in parallel rays or perpendicularly to the contaminated bone surface, and thus they will cross thicknesses superior to the one considered by the Beer-Lambert law. Consequently this results in a higher reduction of the detection efficiency.

As previously mentioned for the constant distance simulation, there is an additional contribution to the efficiency reduction due to the increase of distance between the source and detector. Thus the relative deviation between the Beer-Lambert law results is higher compared to the previous case, approximately 6% and 17%, for additional 3.6 mm and 7.2 mm thickness, respectively.
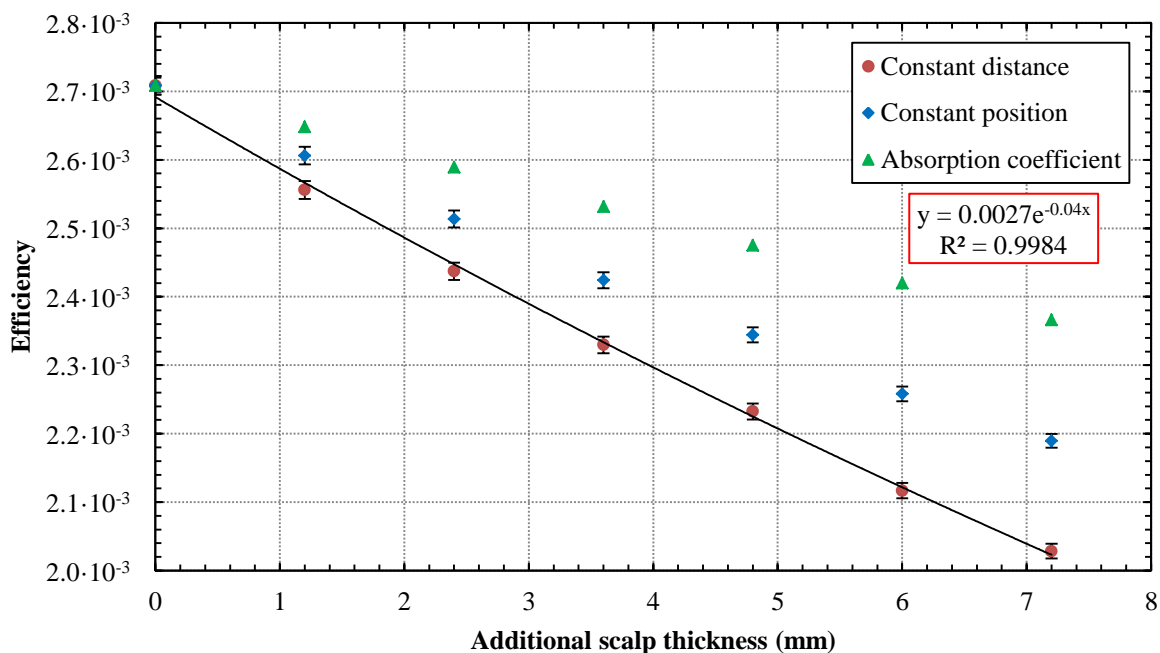
Figure 6.10: Detector 3 full energy peak efficiency at 59.54 keV obtained for different thicknesses of the Max-06 scalp. The detector is positioned perpendicular to the side surface of the phantom for two different cases: 1) in red — the distance between the phantom surface and the detector is constant; 2) in blue — the detector position is fixed. Additionally in green — are shown calculations based on the Beer-Lambert law for the mass attenuation of adipose.

To calculate correction factors for scalp thickness on the side of the head, top of the head, and forehead, the necessary data on the scalp thickness from the phantoms was determined based on Max-06 phantom and the USTUR and BfS voxel phantoms developed by Vrba (2010a), see Table 6.2.

Table 6.2: Max-06, USTUR and BfS phantoms scalp thickness based on voxel models dimensions over the skull bone at three different measurement positions typically used by the HMGU PBC.

	Thickness (mm)		
Phantom	Max-06	USTUR	BfS
Head right side	16.800	17.082	5.469
Head Forehead	7.200	16.133	7.031
Head top	3.600	2.500	6.000

In Table 6.3, one can see that for the Max-06 and USTUR phantom there is significant variability of the scalp thickness depending on the position. The variability of the USTUR phantom is due to the fact that during the construction of the USTUR case 102 tissue equivalent spacers were placed on the outside surface of the skull, in order to provide a realistic variation of the thickness of soft tissue covering the human skull (Hickman and Cohen 1988). In contrast, as can be observed from the small variation between the scalp

thicknesses at the different positions, the BfS phantom scalp was constructed with a layer of soft-tissue-equivalent wax with a constant thickness that corresponds to the average thickness of soft tissue covering the human skull of an average person (Laurer 1993). Such features influence the correction values necessary to apply depending on the measurement position.
In ideal measurement conditions the distance between the detector and the head surface remains the same independently of the scalp thickness. Thus the values obtained from the constant distance simulations (see Figure 6.10) were used to determine correction factors for the scalp thickness for the side of the head, top of the head and forehead, see Figure 6.11, Figure 6.12, and Figure 6.13.

For the application of the scalp thickness correction factor (in the present work called K2) it is necessary to determine the scalp thickness in the measurement position of the measured individual. Having this value the respective position correction factor can than be determined. Has an example if a measured individual was a forehead thickness of 5 mm, in the Figure 6.11 which corresponds to the forehead thickness correction factors one can find the correction factor that should be used for the phantom to correct for the efficiency at the forehead measurement position. In this case it would be 1.077 for the Max-06, 1.561 for the USTUR case 102, and 1.071 for the BfS phantom.
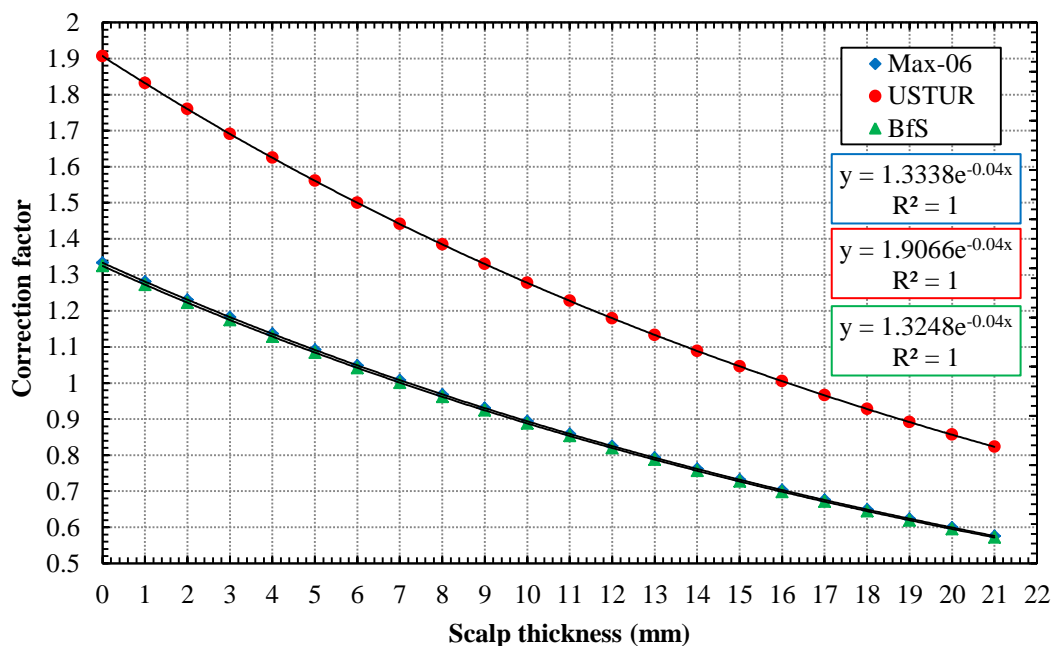
Figure 6.11: Max-06, USTUR case 102 and BfS phantoms K2 correction factors for scalp thickness for the detector 3 positioned at the forehead.
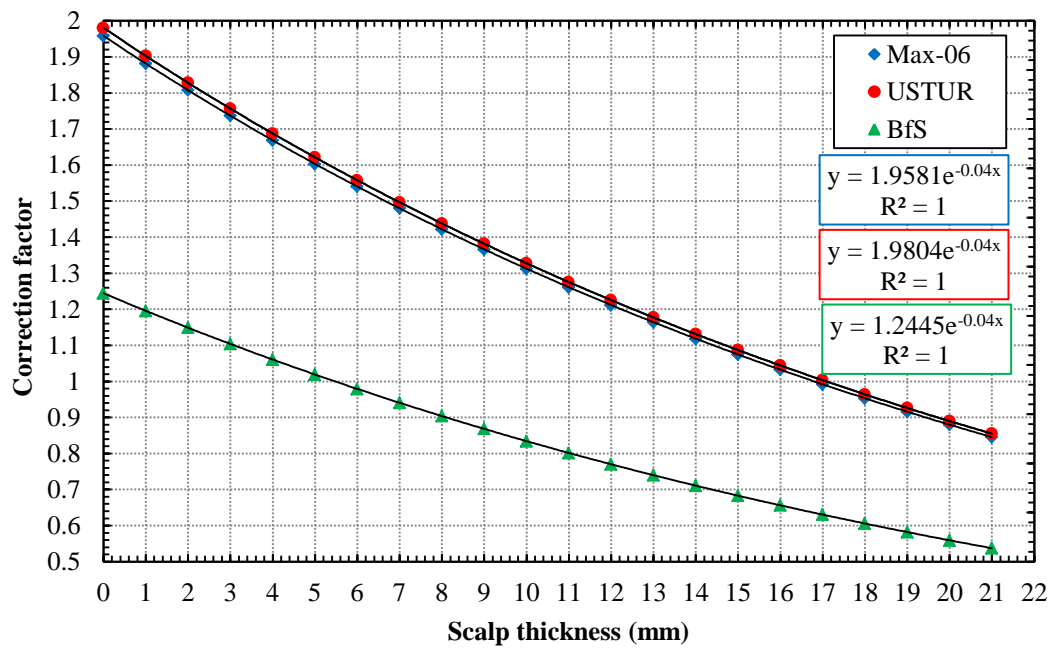
Figure 6.12: Max-06, USTUR case 102 and BfS phantoms K2 correction factors for scalp thickness for the detector 3 positioned at the right side of the head.
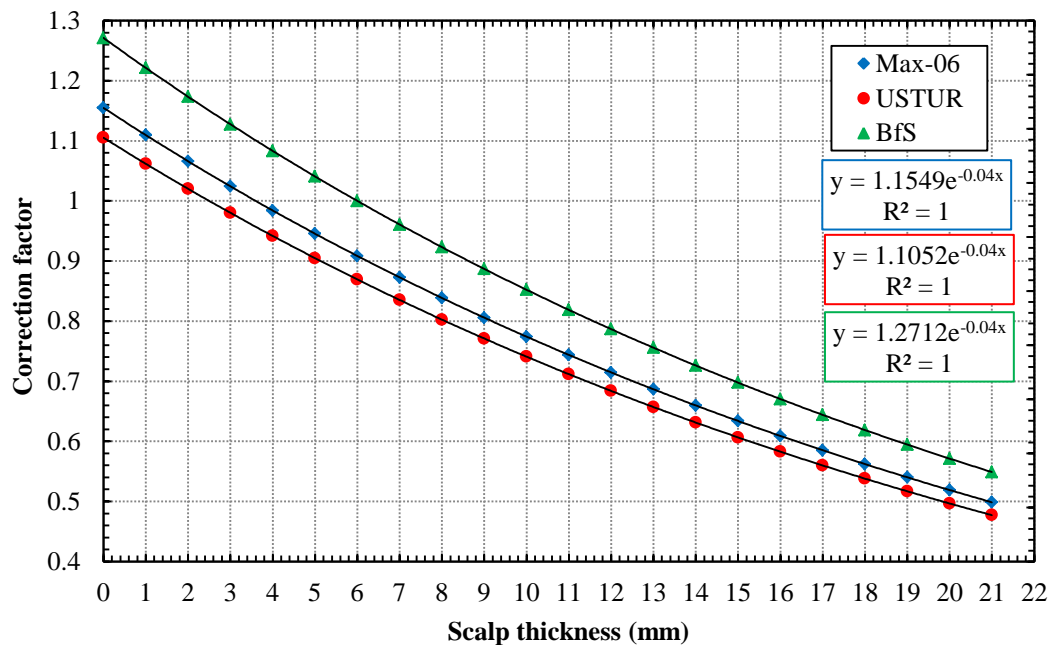
Figure 6.13: Max-06, USTUR case 102 and BfS phantoms K2 correction factors for scalp thickness for the detector 3 positioned at the top of the head.

6.2.3 Conclusion

For the range measured in individuals from the Southern Urals, scalp thickness variability has an impact of approximately 10% in the detection efficiency, which represents a rather small impact. However, as only few data is available on the variation of scalp thickness, a worst case of 10.8 mm was considered, for which an impact of 25% as observed.

Using the values obtained for a constant 1 cm distance between the detector and the head surface correction factors for scalp thickness where calculated for the MAX-06, USTUR case 102 and BfS phantoms at three different measurement positions, the right head side, the top of the head and the forehead.

6.3 Size and shape Influence

The dependence of the efficiency on size and shape is one of the main sources of uncertainty, due to the morphological variability between individuals. To improve the activity estimation after an incorporation it is necessary to use a calibration phantom that is most similar to the measured individual in terms of size and shape, or to interpolate by using different sized phantoms, such as the LLNL torso phantom (Griffith, Anderson et al. 1978) that has difference chest walls thickness available, or the St Petersburg phantom (Kovtun, Firsanov et al. 2000) that can be mounted in different configurations to represent different body masses and sizes. Unfortunately, the number of skull phantoms available world-wide is very limited and those which are available are not flexible as the other previously mentioned phantoms. Alternatively, it is possible to improve the estimation by the use of a mathematical correction, e.g. the relation between the detection efficiency and the solid angle between the detector and the measured individual.

In terms of size the skull is considered to show a relatively small variability between individuals when compared to other regions of the human body used to detect incorporated bone seeking radionuclides. In this chapter the influence of the size and shape of the head on the detection efficiency is described using Monte Carlo simulations and the voxel phantom Max-06 head.

6.3.1 Size impact on detection efficiency

One of the first estimations of impact of the skull size on the estimation of ^{241}Am from *in-vivo* measurements using Monte Carlo methods was done by Malátová and Foltánová (2000). Before, Monte Carlo calculations using voxel and mathematical phantoms (Hunt, Malátová et al. 1999, Malátová, Foltánová et al. 1999) demonstrated the detection efficiency to depend on skull size. Malátová and Foltánová (2000) used Monte Carlo results and measurements of the NRPI phantom, Case 102 head phantom and UCKSKULL 94 head phantom, to estimate the standard deviation of a activity estimation associated to the phantom size used for calibration (32% in relative units) of the NRPI detection system. However, this uncertainty could be reduced by the use of a phantom more similar in terms of dimensions to the measured individual head.

Malátová, Becková et al. (2004) have quantified critical parameters that defined the dependence of the detection efficiency on the skull size. For this they have measured the detection efficiency using 4 phantoms and measured 3 parameters to characterise these head phantoms: 1) the head perimeter, 2) the half perimeter from the top of one ear to the other one, 3) and the half perimeter from the centre of the forehead to the joint between the skull and the neck. They used these parameters to calculate a mean radius and expressed the detection efficiency as an exponential function of this radius.

Later Vrba (2007) studied this issue by means of Monte Carlo methods and a self-developed high resolution voxel phantom, which was based on the CT images of a 38 years old woman. By changing the three voxel size dimension at the same time, he scaled this phantom from 445 mm to a 667 mm head perimeter, and calculated the detection efficiency as a function of the head mean radius as previously done by Malátová, Becková et al. (2004). During this

study he also analyzed the impact of the phantoms' filling with soft tissue which was sometimes incomplete. Vrba concluded the flowing: the detection efficiency depends on the head size but not to an extend suggested by the physical phantoms; the discrepancies between the physical phantoms are due to the incomplete filling and differences in the source distribution; and the use of voxel phantoms for calibration is preferable to the use of inaccurate physical phantoms (Vrba 2010c).

The approach to determine a mean head radius suggested by (Malátová, Becková et al. 2004) is very useful but has the problem of being in some cases ambiguous, e.g. the join between the skull and the neck cannot always be accurately measured: as an example in the Case 102 skull phantom is not possible to perfectly determine this join. Additionally the dimensions cannot be straight forward measured from a voxel phantom.

In the present work the mean radius was calculated from the head width, the head length and the head height from the chin to top of the head, see Figure 6.14. Using the following equation an average value was obtained for the mean radius.

$$R = \frac{X + Y + Z}{6} \qquad\qquad 6.1$$

where R is the radius,
      X is the head width,
      Y is the head length, and
      Z is the head height from the chin to top of the head.

This approach has the advantage of being very well defined and the radius can be easily determined for a voxel phantom. However, since this approach is significantly different to that applied by Malátová, Becková et al. (2004) and Vrba (2007) to calculate a mean radius, the impact of this approach was analysed using the Case 102, BfS Phantom, HMGU Case 1 and Case 2 dimensions.
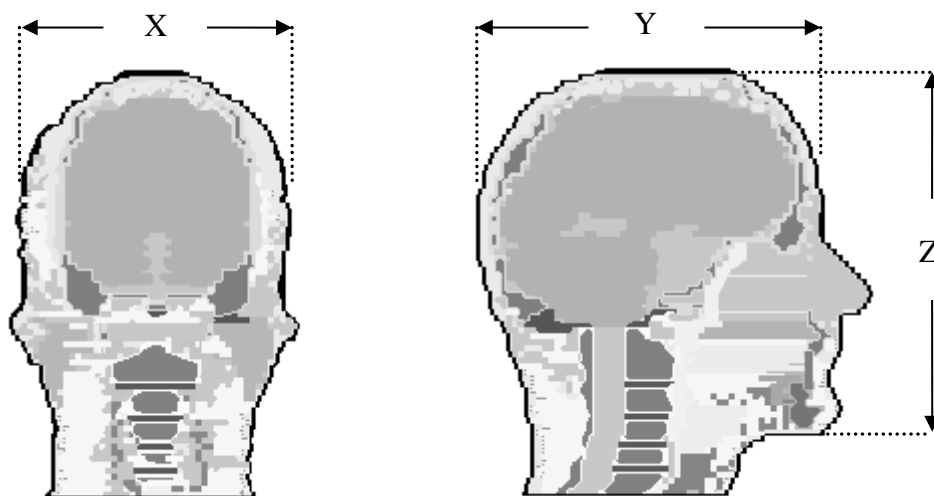
Figure 6.14: Max-06 head phantom transversal and sagittal cross-section view and reference dimensions used for the mean radius calculation. X – head width ;Y – head length   Z – chin to top of the head.

6.3.2 Results

Based on the voxel phantoms data and experimental measurements the head width (X), the head length (Y) and the distance from chin to top of the head (Z) were determined for the USTUR case 102, BfS, Max-06 and two exposure cases to [241]Am that will be discussed in Chapter 7, see Table 6.3. Using these values the mean radius was calculated. In order to verify the impact of this measurement approach the results were compared with the mean radius obtained using the Malátová et al. method. The relative differences obtained are the following: 21% for Case 102 phantom, 8% for the BfS, 7% for case 1 and 10% for case 2. In all cases the method proposed here provides lower values for the mean radius when compared with those obtained using the Malátová et al. method.

Table 6.3: Skull phantoms and Case 1 and 2 dimensions: X − head width, Y − head length and Z − chin to top of the head; and mean radius calculated using the method proposed here and the method proposed by Malátová, Becková et al. (2004).

Head	X (mm)	Y (mm)	Z (mm)	Mean radius (mm)	Mean radius (mm) Malátová et al.
USTUR	174.8	207.7	227.5	101.7	128.9
BfS	129.5	174.0	186.1	81.8	89.13
Max-06	165.6	209.0	218.9	98.9	NE
Case 1	166.0	191.0	234.0	98.5	106.1
Case 2	149.0	192.0	220.0	93.5	103.5

The ICRP-89 (2002) reference men is very accurately defined in terms of height, weight, body surface area, and organ mass and volume. However, no values are given for other parameters of the human anatomy such as the extremity lengths, body circumferences and the human head (Bolch, Lee et al. 2010). Additionally in ICRP-23 (1975) and ICRP-89 (2002) no values are given for the variability of these parameters. Thus, other sources of information are required, e.g. Bolch, Lee et al. (2010) have used the U.S. National Health and Nutrition Examination Survey values to define the height and weight dimensions to construct 25 male and 25 female phantoms

In the present work the values from a report on human engineering design guidelines from the U.S. Department of Defense Human Factors Engineering Technical Advisory Group (HFERAG 2000) were used as reference, to define the variations on the Max-06 phantom dimensions, see Table 6.4.

Table 6.4: Head mean radius calculated based on the head dimensions X – head width, Y – head length and Z – chin to top of the head, given by (HFERAG 2000)

Percentile		X (mm)	Y (mm)	Z (mm)	Mean radius (mm)
1st	Men	139	180	212	88.5
	Women	133	172	198	83.8
5th	Men	139	185	218	90.3
	Women	133	176	204	85.5
50th	Men	152	197	232	96.8
	Women	144	187	218	91.5
95th	Men	161.1	209	255	104.2
	Women	153	198	238	98.2
99th	Men	165	213	255	105.5
	Women	157	202	238	99.5

To determine the influence of the mean head radius in the detector 3 detection efficiency the dimensions of the Max-06 head phantom voxels dimensions X, Y, and Z were modified identically, to maintain the Max-06 head shape, from the original value (1.2 mm) down to 0.989924 mm and up to 1.279865 mm, so that the mean radius would be identical to those of Cases 1 and 2, the physical phantoms and reference values, see Table 6.3 and Table 6.4. The position of the detector was modified so that the distance phantom - detector remains the same independently of phantom size. The detection efficiency obtained was plotted as function of the mean head radius and as done by Malátová, Becková et al. (2004) an exponential equation was fitted to the results, see Figure 6.15.

Scaling voxel dimensions up or down has the disadvantage that together with the external dimensions of the voxel phantom the internal dimensions also change. As a consequence the scalp and the skull bone thickness will also vary with the voxel size modification; such an effect will increase or decrease the tissue absorption and result in an underestimation or overestimation of the size influence on the detection efficiency. To take the influence of scalp thickness variation into account the results were corrected using the values obtained from the calculations using different thicknesses of the Max-06 scalp maintaining the detector at the same position. No correction was used for the bone thickness variation, because according to Vrba (2007), this parameter has only a ± 5% effect on the efficiency results.

In Figure 6.15, the results for the detector 3 efficiency as a function of the mean radius of the Max-06 head phantom as given by GEANT4, with and without correction for the underestimation and overestimation of the scalp thickness, are presented. Without thickness correction the relative deviation between the original Max06 head mean radius (98.9 mm) and the maximum (105.5 mm) and minimum (81.8 mm) is 66% and -16%, respectively; also without the correction the efficiency for the smallest mean radius (81.8 mm, BfS phantom) is approximately twice as large as that for the biggest mean radius (105.5 mm, 99th percentile men). After correcting for the scalp thickness, the relative deviation between the original Max-06 head mean diameter and the maximum and minimum mean diameters, was reduced to is 49% and -13%, respectively; and of course that difference between the smallest and biggest radius was also reduced, in this case to 71% of relative difference.
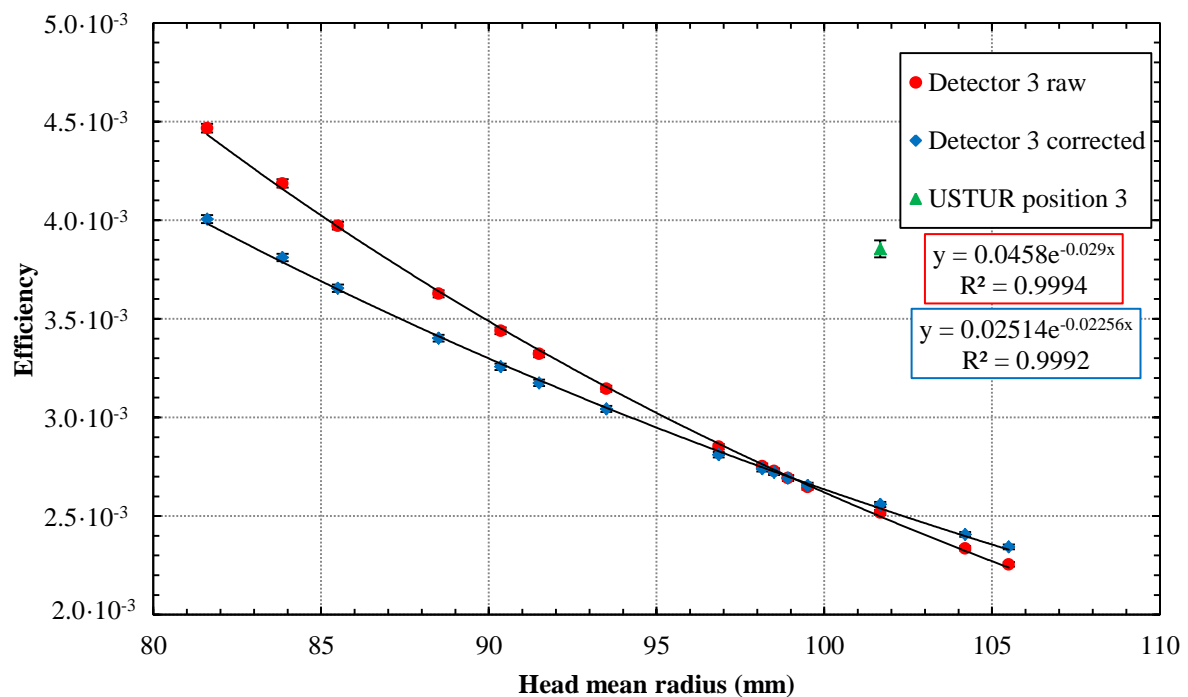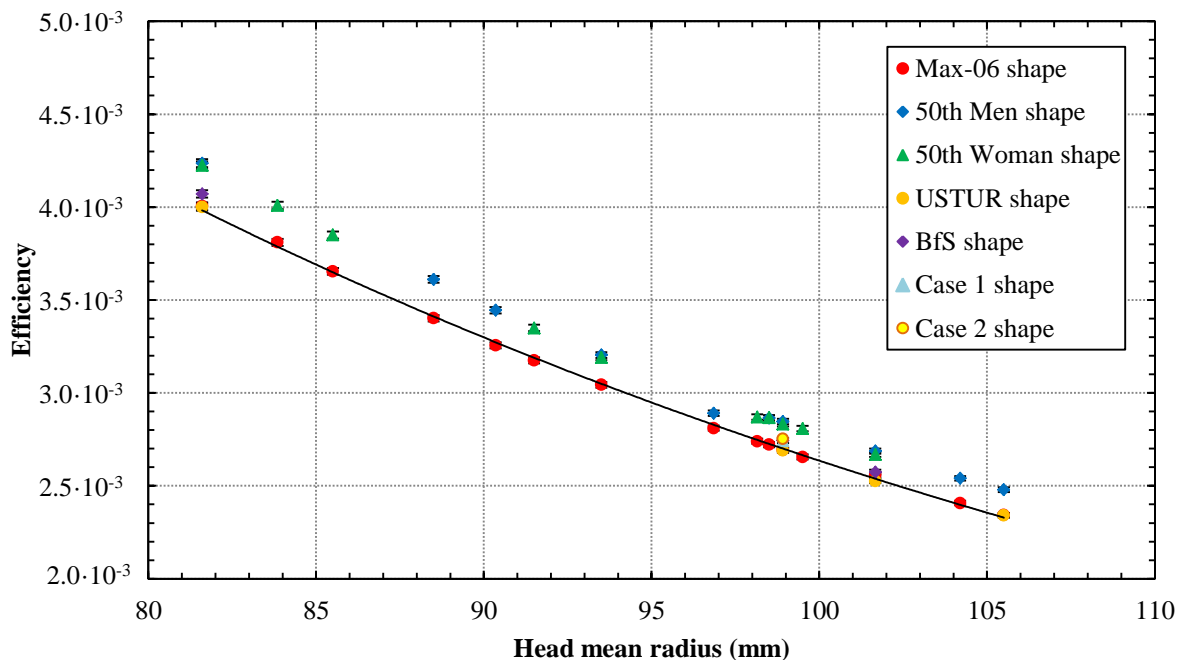
Figure 6.15: GEANT4 simulation of detector 3 at side position of Max-06 phantom: red symbols — full energy peak efficiency as a function of the mean radius when the voxels of Max-06 were scaled up and scaled down to reproduce the mean radius of Cases 1 and 2, the USTUR case 102 phantom, BfS phantom (Table 6.4) and reference values of the mean radius (Table 6.5). Blue symbols — detection efficiency after correcting for variation of scalp thickness (see text). The efficiency measured for USTUR case 102 phantom position 3 is also displayed. Error bars correspond to one sigma uncertainty and are displayed except when the value is smaller than the symbol.

These results can be compared to efficiency values measured for USTUR case 102 and BfS phantoms for the situation that the Max-06 phantom has the corresponding mean radius. For the USTUR case 102 position 3 ($3.854 \times 10^{-3} \pm 5.252 \times 10^{-5}$ efficiency corrected for an activity in the complete USTUR phantom skull bone, see Chapter 3) comparing this efficiency with the Max-06 efficiency there is a relative difference of 51%, which is possibly due to the significant differences between the phantoms such as the activity distribution in the bone surface, the incomplete filling of the USTUR case 102 phantom, the differences in the phantoms shapes and the measurement geometry positioning. In contrast, for the BfS phantom position 12 ($8.212 \times 10^{-3} \pm 5.039 \times 10^{-5}$ efficiency, see Chapter 3) a 105% relative difference was found comparing this efficiency with the Max-06 efficiency. As in the previous case the phantom individual characteristics come in to play, but the most probable reason for this large difference is the incomplete filling of the BfS phantom, due to the use of small spheroids which leave much space in between. In both cases the values observed are in agreement with the results obtained by Vrba (2007).

Using the detector 3 corrected efficiency values shown in Figure 6.11, correction factors for the mean head radius size were determined for the Max-06, the USTUR case 102 and the BfS phantom, see Figure 6.16. These correction factor were calculated by dividing the efficiency obtained for each size by the efficiency obtained for the reference phantom size, e.g. for the

BfS phantom correction factors calculation, all efficiencies were divided by the efficiency obtained when the Max-06 head phantom mean radius is the same as the BfS phantom.
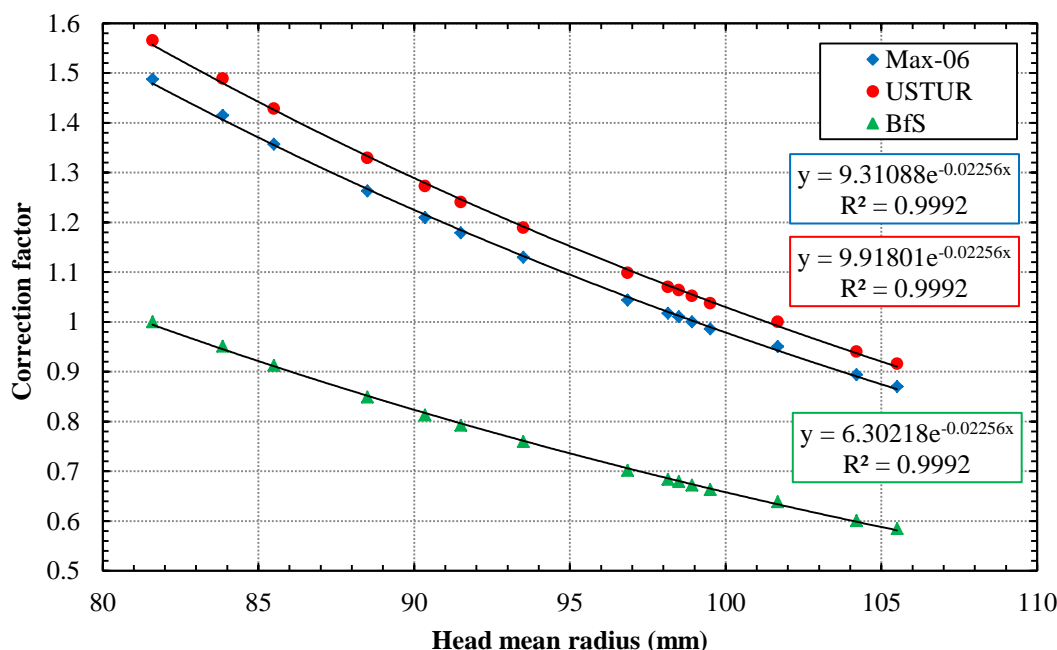
Figure 6.16: Max-06, USTUR case 102 and BfS phantom mean head radius size K3 correction factors.

Has an example of the application of the size correction factor (in the present work called K3): first it is necessary to determine the X – head width, Y – head length and Z – chin to top of the head dimensions of the measured individual. Having these values the measured individual mean head radius can be calculated using Equation 6.1. The mean radius can then be used to find in Figure 6.16 the correction factor for the respective phantom by using this value in the exponential equation adjusted to the respective phantom correction factors. Thus an individual with the head dimensions 148 mm (X), 193 mm (Y), and 222 mm (Z) would have a mean head radius of 93.83 mm, by applying this value in the BfS correction factor exponential equation, the result 0.788 is the correction factor to be used for this phantom.

6.3.3 Conclusion

Despite the fact that the skull possesses a reduced variability in terms of size between individuals, the results obtained in this work demonstrate that this variability has a significant impact on the detection efficiency. Relative differences of 71% were found here between the smallest and biggest radius. A 51 relative difference was found with the USTUR case 102 measurement results; for the BfS phantom measurements, a relative difference of 105% was found. Both discrepancies are possibly due to the incomplete filling of the phantoms, the activity distribution, the scalp thickness and the shape.
Finally using the values calculated, mean head radius size correction factors were calculated for the Max-06, USTUR case 102 and BfS phantom.

6.3.4 Shape impact in detection efficiency

The human head shape is closely related with to respective skull shape, and as one can see in Figure 6.17, there are significant differences in the skull shapes between different human races: typical Negroid individuals have lower and narrow skulls, Caucasoid have narrow skulls and Mongoloid have broader skulls (Shipman, Walker et al. 1985). Even between members of the same race there are differences in the shape especially between sex: male skulls are larger and are more angular, while female skulls are smaller and more rounded. Such shape differences have been used successfully to identify the sex and the race of skeleton remains (Shipman, Walker et al. 1985).
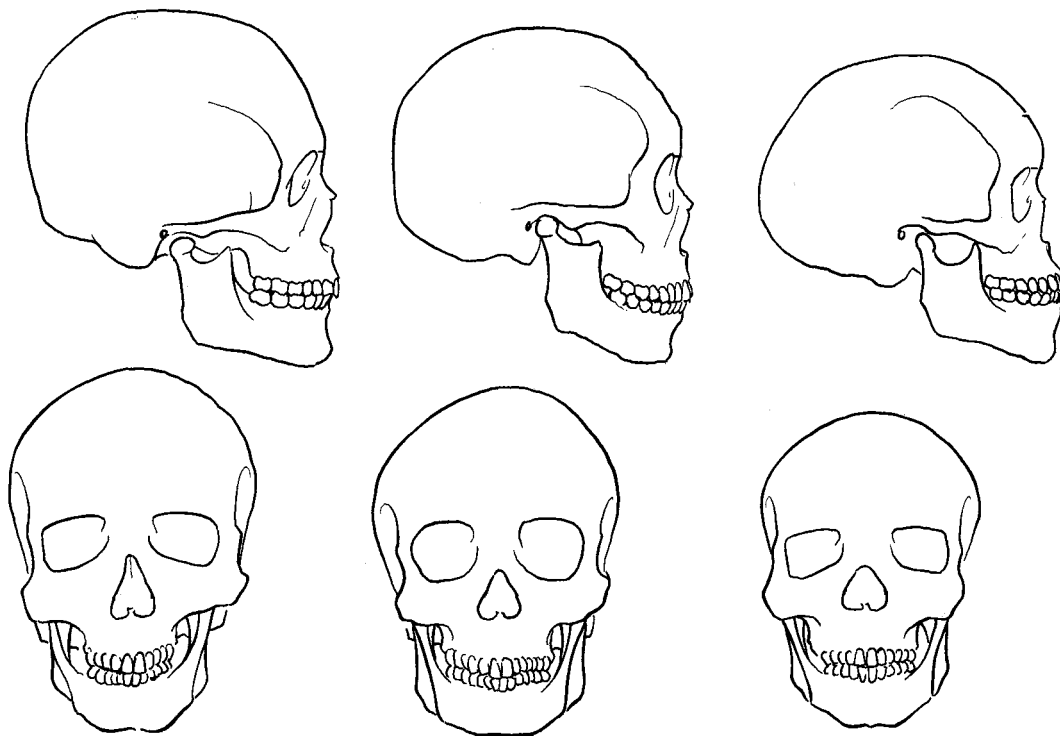
Figure 6.17: Differences between head shapes of different races, from left to right: male Mongoloid, male Caucasoid and male Negroid (Shipman, Walker et al. 1985)

The impact of the head shape on the detection efficiency has been only recently addressed. Vrba (2012) using the Linda head voxel phantom has performed a great number of Monte Carlo simulations to study the head shape influence by changing the phantom voxel X, Y, and Z dimensions in discrete steps. From the results obtained it was estimated that if no correction to this parameter is performed an uncertainty of the detection efficiency between 3.5% and 10.5% should be added to the measurement uncertainty of the NRPI PBC detection system.

In the present work the shape impact on the detection efficiency was analyzed for the Case 102 phantom, the BfS phantom, the Max-06 phantom, Case 1, Case 2, reference person's and some additional hypothetical shapes. Using these results correction factors for the head shapes were calculated.

6.3.5 Results

The Max-06 head dimensions X – head width, Y – head length and Z – chin to top of the head (see Table 6.3) were modified so that they would match the other skull phantoms, the head of Case 1, the head of Case 2 and the 50th percentile men and women head dimensions (see Table 6.3 and Table 6.4). By matching the dimension the head shape was also matched. To verify whether the shape influence on the detection efficiency is independent of the mean head radius size influence calculations were performed: simulations were performed for different mean radius dimensions by scaling the voxels' xyz dimensions in the same proportion, so that it maintained the shape (Chapter 6.3.1). As described previously the scaling up and down of the voxels will increase or decrease the tissue absorption and result in an underestimation or overestimation of the size and shape influence in the detection efficiency. To avoid this, all results were corrected using the values obtained from the calculations using different thicknesses of the Max-06 scalp. The scaling up and down also affects the bone thickness; however, no correction was used to correct for this effect.

In Figure 6.18, the results for detector 3 efficiency obtained using the Max-06 head phantom with different shapes as a function of the mean head radius and corrected for the scalp thickness increase are displayed. No correlation was found between the head shape and the head mean radius, as the results for the different shapes maintain approximately the same difference to the original Max-06 shape independently of the mean head radius. These results show also that the shape has only a small impact on the detection efficiency, since the biggest relative deviation was only the 6% obtained between the 50th percentile men shape and the Max-06 shape. Excellent agreement was found between the USTUR and the Max-06 results with a relative deviation generally below 1%, and a notable agreement was found between the 50th percentile men and women shapes, with a relative deviation generally below 0.5%.

Figure 6.18: GEANT4 simulation of detector 3 at side position of Max-06 phantom full energy peak efficiency results as a function of the mean radius for different shapes. Red symbols — Max-06 shape. Blue symbols — 50th percentile men. Green symbols — 50th percentile woman shape. Yellow symbols — USTUR case 102 phantom shape. Purple

symbols — BfS phantom shape. Light blue symbols — Case 1 phantom shape. Yellow orange symbols — Case 1 phantom shape. Error bars correspond to one sigma uncertainty and are displayed except when the value is smaller than the symbol.

To help to analyse the results for each head, the dimensions X – head width, Y – head length and Z – chin to top of the head (see Table 6.3 and Table 6.4) were normalized by dividing them by the respective mean head radius. This normalized value was then compared with the 50th percentile men dimensions, see Table 6.6 and Table 6.7. For the Case 1 and 2 the difference obtained between their dimensions and the 50th percentile men dimensions are generally below 10%. The USTUR and the Max-06 have a very similar shape which explains the excellent agreement between the detection efficiencies obtained, see Figure 6.18.

In Table 6.6, the normalized ratio obtained between the reference head dimensions given by HFERAG (2000), reveal that in fact all the values given by this reference correspond approximately to the same shape, with differences below 1%, which explains the notable agreement between the detection efficiency obtained for the men and women shape. The reason for the small variability between head shapes observed is possibly that the values are only based on the North American population, for whom there are few differences between sexes, and that the head shape variability is independent of the head size and thus this reference is not representative of the shape variability between individuals.

Table 6.5: Skull phantoms and Case 1 and 2 dimensions: X – head width, Y – head length and Z – chin to top of the head (see Table 6.3), divided by the respective mean radius value, and ratio between the dimension divided by the respective mean radius and the 50th percentile men equivalent value, see Table 6.6.

Head	Mean radius (mm)	Normalized by mean radius			Ratio to 50th percentile men		
		X	Y	Z	X	Y	Z
USTUR	101.7	1.719	2.043	2.238	1.095	1.004	0.934
BfS	81.6	1.587	2.132	2.281	1.011	1.048	0.952
Max-06	98.9	1.674	2.113	2.213	1.067	1.039	0.924
Case 1	98.5	1.685	1.939	2.376	1.074	0.953	0.992
Case 2	93.5	1.594	2.053	2.353	1.015	1.009	0.982

Table 6.6: Reference head dimensions X – head width, Y – head length and Z – chin to top of the head, given by HFERAG (2000) (see Table 6.4), divided by the respective mean radius value, and ratio between the dimension divided by the respective mean radius and the 50th percentile men equivalent value.

Head		Mean radius (mm)	Normalize by mean radius			Ratio to 50th percentile men		
Percentile			X	Y	Z	X	Y	Z
1st	Men	88.5	1.571	2.034	2.395	1.001	1.000	1.000
	Women	83.8	1.586	2.052	2.362	1.011	1.008	0.986
5th	Men	90.3	1.539	2.048	2.413	0.980	1.007	1.007
	Women	85.5	1.556	2.058	2.386	0.991	1.012	0.996
50th	Men	96.8	1.570	2.034	2.396	1.000	1.000	1.000
	Women	91.5	1.574	2.044	2.383	1.003	1.005	0.994
95th	Men	104.2	1.546	2.006	2.448	0.985	0.986	1.022
	Women	98.2	1.559	2.017	2.424	0.993	0.991	1.012
99th	Men	105.5	1.564	2.019	2.417	0.996	0.992	1.009
	Women	99.5	1.578	2.030	2.392	1.005	0.998	0.998

To further study the impact of the head shape variation in the detection efficiency, several hypothetical cases were created by independently increasing the X, Y and Z dimensions of the 50th percentile men by factors of 10% and 30% independently, but maintaining the same mean head radius, see Table 6.7. The results obtained show that a 10% increase gives at maximum 2.1% relative deviation between the efficiency results and those for the 50th percentile men head shape. For the 30% increase the results the relative difference is also not significant with a maximum of 5.4% obtained for the 30% increase on the Z dimension. Both 10% and 30% increases show the same tendency: increase of the X dimension reduces the efficiency, since the opposite side contaminated bone will contribute less to the measurement; increase of the Y dimension has little effect in the efficiency; increase of the Z dimension increases the efficiency, possibly due to the decrease of the head curvature and consequently due to a better approximation between the bone and the detector for this position; the increase of the X and Y dimensions decreases the efficiency; the increase of the X and Z dimensions as little effect in the efficiency; and the increase of the X and Y dimensions increases the efficiency, due the reduction of the X dimension, and consequently the increase of the opposite side bone contribution to the measurement.

Table 6.7: Detection efficiency obtained for detector 3 and Max-06 phantom with modified dimensions to match hypothetical shape cases created by independently changing the X, Y and Z dimensions of the 50th percentile men by 10% and 30%. Additionally the ratio between the hypothetical shape cases and the 50th percentile men are shown.

| | Ratio to 50th percentile men | | | | |
	X	Y	Z	Efficiency	Uncertainty
50th Men shape	1.000	1.000	1.000	$2.891 \cdot 10^{-3}$	$1.445 \cdot 10^{-5}$
X + 10%	1.072	0.975	0.975	$2.829 \cdot 10^{-3}$	$1.415 \cdot 10^{-5}$
Y + 10%	0.967	1.064	0.967	$2.882 \cdot 10^{-3}$	$1.441 \cdot 10^{-5}$
Z + 10%	0.962	0.962	1.058	$2.943 \cdot 10^{-3}$	$1.472 \cdot 10^{-5}$
X + 10%, Y + 10%	1.038	1.038	0.943	$2.845 \cdot 10^{-3}$	$1.423 \cdot 10^{-5}$
X + 10%, Z + 10%	1.032	0.938	1.032	$2.885 \cdot 10^{-3}$	$1.442 \cdot 10^{-5}$
Y + 10%, Z + 10%	0.931	1.024	1.024	$2.929 \cdot 10^{-3}$	$1.465 \cdot 10^{-5}$
X + 30%	1.205	0.927	0.927	$2.757 \cdot 10^{-3}$	$1.378 \cdot 10^{-5}$
Y + 30%	0.908	1.180	0.908	$2.901 \cdot 10^{-3}$	$1.450 \cdot 10^{-5}$
Z + 30%	0.893	0.893	1.161	$3.047 \cdot 10^{-3}$	$1.524 \cdot 10^{-5}$
X + 30%, Y + 30%	1.102	1.102	0.847	$2.768 \cdot 10^{-3}$	$1.384 \cdot 10^{-5}$
X + 30%, Z + 30%	1.085	0.835	1.085	$2.904 \cdot 10^{-3}$	$1.452 \cdot 10^{-5}$
Y + 30%, Z + 30%	0.819	1.064	1.064	$3.009 \cdot 10^{-3}$	$1.505 \cdot 10^{-5}$

Correction factors were calculated for the Max-06, the USTUR phantom and the BfS phantom to correct the detection efficiency for the shape of the phantoms, Case 1, Case 2, the 50th percentile men shape and the hypothetical head shapes. These factors were based on the detection efficiency of detector 3 obtained for each shape when the mean radius is identical to the 50th percentile men radius, see Table 6.8, Table 6.9 and Table 6.10.

To use the shape corrections factors for a new individual head measurement, the new head dimensions X, Y, and Z need to be divided by its own mean radius. These normalized values should then be divided by the corresponding dimensions of the calibration phantom (see Table 6.5) and the most similar ratio displayed in Table 6.8, Table 6.9, and Table 6.10 corresponding to this phantom will indicate the correction factor to be used.

As an example of the application of the size correction factor (in the present work called K4): first it is necessary to determine the X – head width, Y – head length and Z – chin to top of the head dimensions of the measured individual. With these values the measured individual mean head radius should be calculated using Equation 6.1, and divided by its own mean radius. These normalized values should then be divided by the corresponding normalized dimensions of the calibration phantom (see Table 6.5) and the most similar ratio displayed in Table 6.8, Table 6.9, and Table 6.10 corresponding to this phantom will indicate the correction factor to be used.

Thus a person with the head dimensions 148 mm (X), 193 mm (Y), and 222 mm (Z) would have a mean radius of 93.83 mm. The normalized dimensions are then 1.577 (X), 2.057 (Y), 2.36 (Z). To determine the correction factor for the BfS phantom it is necessary to divide the normalized values by the BfS normalized values in Table 6.6; the result is 0.994 (X), 0.965 (Y), and 1.037 (Z). From Table 6.11 which shows the shape correction factors based on the

BfS phantom for example, correction factors for shape one can see that the most similar ratio is the 50th percentile men shape and thus a 1.013 correction factor should be correct the BfS efficiency for this individual head shape.

Table 6.8: Correction factors K4 based on the Max-06 head phantom to correct for the head shape of the USTUR phantom, BfS phantom, Case 1, Case 2, 50th percentile men dimensions and additional hypothetical shapes created by independently changing the X, Y and Z dimensions of the 50th percentile men by 10% and 30%.

Head	Ratio to Max-06 head			Correction factor
	X	Y	Z	
MAX-06	1.000	1.000	1.000	1.000
USTUR case 102	1.027	0.967	1.011	1.000
BfS	0.948	1.009	1.031	1.015
Case 1	1.007	0.918	1.074	1.010
Case 2	0.952	0.972	1.063	1.019
50th Men shape	0.938	0.963	1.083	1.028
X + 10%	1.006	0.939	1.056	1.007
Y + 10%	0.907	1.025	1.048	1.025
Z + 10%	0.902	0.926	1.146	1.047
X + 10%, Y + 10%	0.973	1.000	1.022	1.012
X + 10%, Z + 10%	0.968	0.904	1.118	1.026
Y + 10%, Z + 10%	0.874	0.987	1.110	1.042
X + 30%	1.131	0.893	1.004	0.981
Y + 30%	0.851	1.137	0.983	1.032
Z + 30%	0.838	0.860	1.258	1.084
X + 30%, Y + 30%	1.033	1.061	0.918	0.985
X + 30%, Z + 30%	1.018	0.804	1.175	1.033
Y + 30%, Z + 30%	0.768	1.025	1.153	1.071

Table 6.9: Correction factors K4 based on the USTUR case 102 phantom to correct for the head shape of the Max-06 head phantom, BfS phantom, Case 1, Case 2, 50th percentile men dimensions and additional hypothetical shapes created by independently changing the X, Y and Z dimensions of the 50th percentile men by 10% and 30%.

Head	Ratio to USTUR case 102			Correction factor
	X	Y	Z	
MAX-06	0.974	1.034	0.989	1.000
USTUR case 102	1.000	1.000	1.000	1.000
BfS	0.923	1.044	1.019	1.015
Case 1	0.980	0.949	1.062	1.011
Case 2	0.927	1.005	1.051	1.020
50th Men shape	0.913	0.996	1.071	1.029
X + 10%	0.979	0.971	1.044	1.007
Y + 10%	0.883	1.060	1.036	1.026
Z + 10%	0.878	0.958	1.133	1.048
X + 10%, Y + 10%	0.948	1.034	1.011	1.013
X + 10%, Z + 10%	0.942	0.935	1.105	1.027
Y + 10%, Z + 10%	0.851	1.021	1.097	1.043
X + 30%	1.101	0.924	0.993	0.981
Y + 30%	0.829	1.176	0.972	1.032
Z + 30%	0.816	0.890	1.244	1.085
X + 30%, Y + 30%	1.006	1.097	0.908	0.985
X + 30%, Z + 30%	0.991	0.831	1.162	1.034
Y + 30%, Z + 30%	0.748	1.060	1.140	1.071

Table 6.10: Correction factors K4 based on the BfS phantom to correct for the head shape of the Max-06 head phantom, USTUR case 102 phantom, Case 1, Case 2, 50th percentile men dimensions and additional hypothetical shapes created by independently changing the X, Y and Z dimensions of the 50th percentile men by 10% and 30%.

| Head | Ratio to BfS Phantom | | | Correction factor |
	X	Y	Z	
MAX-06	1.055	0.991	0.970	0.985
USTUR case 102	1.083	0.958	0.981	0.985
BfS	1.000	1.000	1.000	1.000
Case 1	1.062	0.909	1.042	0.995
Case 2	1.004	0.963	1.032	1.005
50th Men shape	0.990	0.955	1.051	1.013
X + 10%	1.061	0.930	1.024	0.992
Y + 10%	0.957	1.016	1.017	1.010
Z + 10%	0.952	0.918	1.112	1.032
X + 10%, Y + 10%	1.027	0.991	0.992	0.998
X + 10%, Z + 10%	1.021	0.895	1.084	1.011
Y + 10%, Z + 10%	0.922	0.978	1.077	1.027
X + 30%	1.193	0.885	0.975	0.966
Y + 30%	0.898	1.126	0.954	1.017
Z + 30%	0.884	0.852	1.220	1.068
X + 30%, Y + 30%	1.090	1.051	0.891	0.971
X + 30%, Z + 30%	1.074	0.797	1.140	1.018
Y + 30%, Z + 30%	0.810	1.016	1.119	1.055

6.3.6 Conclusion

The results obtained show that the shape of the head has only a small influence on the detection efficiency, in agreement with the results obtained by Vrba (2012). It was also demonstrated that the influence of the head shape on the detection efficiency is independent of the head mean radius. This independency allowed the calculation of shape correction factors for one mean radius, which can be used for any other mean radius.

For the MAX-06 phantom, USTUR phantom, and BfS phantom, correction factors were calculated to correct for the head shape of the phantoms, Case 1, Case 2, 50th percentile men dimensions and additional hypothetical head shapes that were created by changing the dimensions 50th percentile men by an increase of 10% and 30% in the X, Y, and Z dimensions.

6.3.7 Alternative shape and size correction factor

All corrections factors were calculated for the HMGU detector 3 at the side position of the head, however, they can be applied to other detectors and other position such has this work positions top of the head position and forehead. Only the shape correction factor will be dependent on the measurement position because the head is not a sphere and has it was observed in simulation for extreme cases of head shapes the main contribution to the efficiency variation is the contribution of the opposite side to the measurement position. Based on this last observation a new approach was study for the shape and size correction factors. The new correction factors were determine by plotting the detection efficiency obtained for the different mean radius (see Figure 6.16), in function of the respective simulated heads X dimension, an exponential was then adjusted to this values. The correction factors for BfS phantom were obtained by dividing the detection efficiency for different X dimensions by the detection efficiency of the BfS phantom X dimension, see Figure 6.19.

The plot shows Correction factor (y-axis, 0.2 to 1) versus Dimension (mm) (x-axis, 120 to 240), with green triangle data points labeled BfS and a fitted curve:

$$y = 5.71884e^{-0.01345x}$$
$$R^2 = 0.9995$$
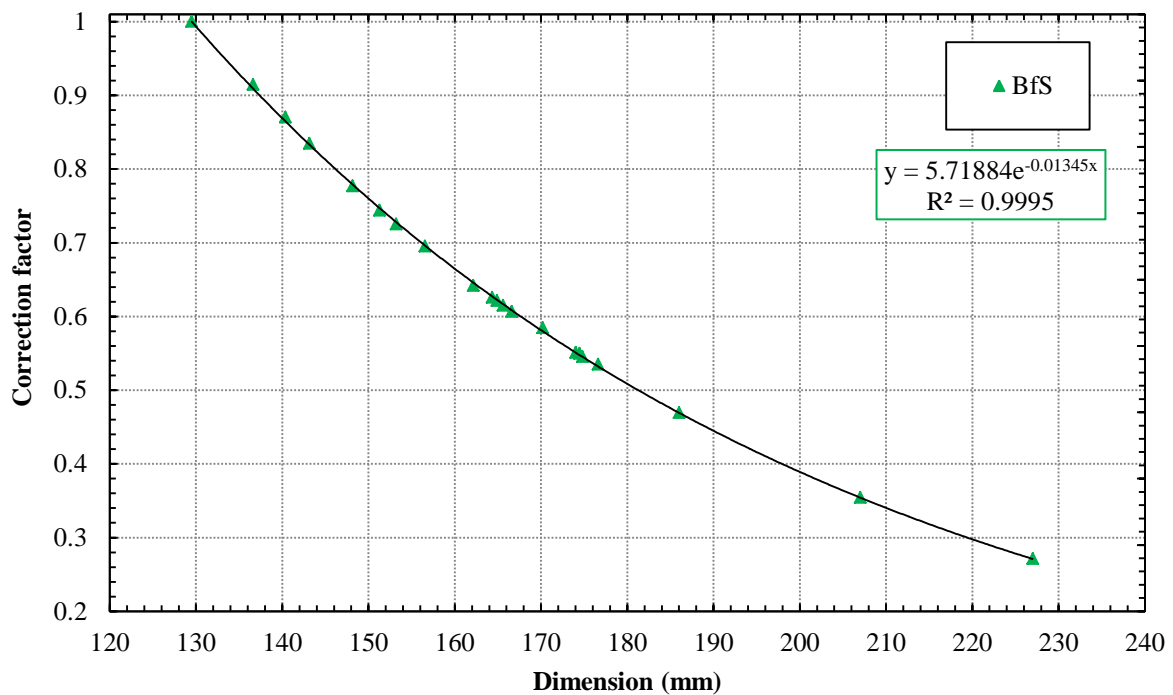
Figure 6.19: BfS phantom alternative size and shape correction factor based on the Geant4 simulation results for different sizes of the Max-06 head.

To test the new size and shape correction factor two measurements were performed: one to the BfS phantom right side and the other to the forehead, both measurements were performed using detector 3 and using the measurement geometry similar to Figure 7.4. According to the new correction factor approach the main reason of the efficiency discrepancy between both measurements positions is due to the differences in the X and Y dimensions and respective the differences in the contribution of the opposite side bone to the measurements. Thus it should be possible to correct the side position measurements efficiency to match the forehead detection efficiency.

The detection efficiency obtained for the BfS side of the head position is $9.06\times10^{-3} \pm 5\times10^{-5}$ while for the forehead position is $6.09\times10^{-3} \pm 5\times10^{-5}$. The correction factor 0.551 for the BfS Y dimension (174 mm) was determined from Figure 6.19. The side of the head efficiency after correction is $4.99\times10^{-3} \pm 3\times10^{-5}$ which comparing with the forehead position efficiency has a relative deviation of 18%. However, for measurements of the BfS phantom in the EURADOS intercomparison for position 12 and position 1 (see Figure 3.3), which are respectively located in the side of the head and forehead, the efficiency values are identical, see Figure 3.6. Thus the use of the new correction factor results on a 50% relative discrepancy, between the position 12 efficiency corrected for forehead position. The reason for the discrepancy between the two tests can be due the improper fill of the brain region of the BfS phantom and the measurement geometry: in the EURADOS intercomparison the detector 3 is parallel to the surface of the phantom forehead, while in the test measurement the detector 3 is parallel to the face of the phantom.

The use of the correction factor size and shape together demonstrate to improve detection efficiency, however, this improvement is dependent on the measurement geometry used. Since the main objective of this approach was the correction of the shape impact on the detection efficiency which is in the worst case scenario 5.4%, this approach was not used in following work.

6.4 Personalized calibration for USTUR phantom

The correction factors previously calculated were applied to the measured efficiency of the BfS phantom, to calculate the personalized efficiency for USTUR case 102 phantom, for the detector 3 at the side position. Comparison of the result with the efficiency measured for this phantom allows to get a rough idea on the reliability of the deduced correction factor. Without any correction, the efficiency measured for position 12 ($8.21\times10^{-3} \pm 5\times10^{-5}$ efficiency, see Chapter 3) is a factor 2.4 times higher than that of USTUR case 102 efficiency for position 3 both using detector 3 ($3.85\times10^{-3} \pm 5\times10^{-5}$, see Chapter 3). After application of the correction factors previously determined (Table 6.12) the BfS phantom efficiency becomes to corrected for the USTUR phantom critical head parameters: the BfS efficiency is only 21% inferior ($3.06 \times10^{-3} \pm 2\times10^{-5}$) the USTUR case 102 phantom.

To do this, for K1 a value of 0.948 is assumed, because of the biokinetic data and the calculation results for different ratios between the cortical and trabecular activities (see Figure 6.6 and Figure 6.7) and because the BfS phantom was constructed in a way that only the cortical bone surfaces was contaminated.
Because the skin thickness of the USTUR at position 3 is much larger (17.08 mm) than that of the BfS phantom at position 12 (5.47 mm) (see Table 6.2) the correction factor K2 = 0.628 was used. The K2 was calculated from the Equation 6.2 (where X is the skin thickness to correct for), which is a function adjusted to the BfS correction factors calculated for the skin thickness in Figure 6.12, green symbols,.

$$K2 = 1.2445 \times e^{-0.04\times X} \qquad\qquad 6.2$$

As for the head size, the mean head radius is 81.8 mm for the BfS phantom while it is 101.7 mm for the USTUR phantom, see Table 6.4. Thus, to adjust the efficiency of the BfS skull phantom for this difference the correction factor K3 = 0.635 was used. The K3 was calculated from the Equation 6.3 (where X is the mean radius to correct for), which is a function adjusted to the BfS correction factors calculated for the skin thickness in Figure 6.16, green symbols.

$$K3 = 6.30218 \times e^{-0.02256\times X} \qquad\qquad 6.3$$

Finally, for the specific shape of the USTUR phantom, the efficiency of the BfS phantom must be corrected by K4 = 0.985, which is taken from Table 6.10.

As a result, a total correction factor of 0.373 was used, which as previously mentioned gives a efficiency with a relative deviation of only 21% inferior comparing with the USTUR case 102 efficiency, see Table 6.11. However, based in the values determined for influence in the detection efficiency of the activity distribution pattern present of the USTUR case 102, an additional correction factor can be used assuming that the BfS activity distribution in the bone surface is homogenous. The correction factor for this is given by the ratio between the detection efficiency obtained for the activity distribution pattern and the homogenous distribution, which is 0.917. Taking in account this value the final BfS personalized efficiency it is now for the USTUR is $2.81 \times10^{-3} \pm 2\times10^{-5}$ that is still only 27% inferior to the efficiency obtained with the USTUR phantom.

The improvement on the agreement between the phantoms efficiencies validates the use of the correction factors calculated in the present work. The remaining 27% (or 21% depending on the correction factors used) difference between the phantoms efficiencies is possibly due to the difference in the fill of the phantoms, this is confirmed by Vrba (2007) that demonstrated using Monte Carlo and a voxel phantom that an incomplete fill of a phantom brain region would increase the efficiency up to a factor of 2. Since the USTUR phantom fill is in fact incomplete in the left side (see Figure 5.4), hypothetically speaking, if the USTUR phantom was completely filled the phantom detection efficiency would be inferior, which would possibly increase the agreement with the BfS phantom personalized efficiency for the USTUR phantom. Additional contributors for the discrepancy can be the materials used for the reconstruction of the soft tissue and differences between the natural and artificial contamination of the phantoms bone.

Table 6.11: Detection efficiency obtained with BfS phantom at the right side (EURADOS Intercomparison position 12, see Chapter 3) and application of the correction factors calculated for USTUR case 102 phantom.

| Detector | Position | Efficiency | | Correction factors | | | | | Efficiency | |
		Measured	Uncertainty	K1 Cortical and trabecular bone	K2 Skin thickness	K3 Head size	K4 Head shape	Ktotal	Corrected for USTUR	Uncertainty
3	Right side	$8.21 \cdot 10^{-3}$	$5 \cdot 10^{-5}$	0.948	0.628	0.635	0.985	0.373	$3.06 \cdot 10^{-3}$	$2 \cdot 10^{-5}$

7 Individual specific calibration

Recently an accidental exposure occurred during the decommissioning of an old chemistry laboratory. Two individuals were internally contaminated with ^{241}Am in the form of Americium Chloride during the handling of an old ^{241}Am source. The contamination was discovered in a routine measurement of the laboratory one week later by a radiation protection control team composed by three members. Shortly after urine *in-vitro* tests confirmed the internal contamination of all five persons.

Measurements performed at the Federal Office of Radiation Protection (BfS), Germany, showed that the internal contamination of the three members of the control team was below the detection limit of the BfS partial body counter for lung counting measurements. However, for the first two individuals exposed the results showed clearly an internal contamination with ^{241}Am. These two individuals, in this work named Case 1 and Case 2, were then measured at the HMGU partial body counter (PBC) for skull geometry; the results obtained confirmed the internal contamination.

The Case 1 is a Caucasian male with 178 cm height, and 96 kg body mass, who was 67 years old at the time of exposure. This individual was the first one to handle with the contamination source, which explains the higher values obtained for this individual. The Case 2 is a Caucasian female with 164 cm height, 66 kg body mass, who was 44 years old at the time of exposure, see Table 7.1. This individual was near by when Case 1 was exposed and also handled the contamination source. In both cases no DTPA therapy was applied. To date Case 1 and 2 were measured three times using the HMGU Partial body counter. In this chapter the results obtained are presented, and analyzed using the correction factors for the critical head parameters calculated in Chapter 6.

Table 7.1: Details on Case 1 and 2, and respective internal contamination path and data.

	Case 1	Case 2
Birthday	2-2-1947	25-09-1968
Height (mm)	1780	1640
Body mass (kg)	96	66
Contamination date	18-04-2013	18-04-2013
Contamination radionuclide	^{241}Am	^{241}Am
Contamination chemical formula	$AmCl_3$	$AmCl_3$
Probable contamination path	Inhalation and Ingestion	Inhalation and Ingestion

7.1 Methods

For partial body counting, estimation of the total ^{241}Am in the skeleton is done using a method developed by Cohen, Spitz et al. (1977), in which is assumed that the ^{241}Am is uniformly distributed in the mineral mass (bone and teeth), and that for example the head represents 15.7% of the mineral mass of the total skeleton, and that consequently it contains 15.7% of the ^{241}Am deposited in the skeleton. It is also assumed that all measured counts are from gammas originated in the fraction of bone measured. Skull measurements have the advantage that it is possible to reduce the contributions of neighboring contaminated regions of the human body to the measurement signal by proper shielding (Cohen, Spitz et al. 1977).

For Case 1 and 2, dedicated shielding was prepared made of 5 mm think lead foil and covered with isolation tape to prevent lead poisoning, see Figure 7.1. It was design and constructed to isolate the head from the body.

Figure 7.1: Lead shielding designed and constructed to shield the body from the skull; it is made of 5 mm think lead foil and covered with isolation tape to prevent lead poisoning.

To improve the measurement geometry, a new detector configuration set was used where the detectors were placed perpendicular to the head surface at the top of the head, side of the head and forehead, see Figure 7.2. Compared with the previous configuration this configuration has the advantage that the detector positioning is easier to be reproduced and implemented in the Monte Carlo computational simulations, it has also the advantage that detector 2 and 3 can be positioned closer to the head surface.

To increase the comfort of the measured person the distance between the detector window and the head surface was increased from close contact to 1 cm. To analyse the impact of the new configuration two measurements were performed to the BPAM phantom, using the detector 3,

the first measurement was at close contact using a plastic end cap protection for the carbon epoxy window; the second measurement was performed at 1 cm distance and having the plastic end cap (previously used) removed. For the first measurement it was obtained an efficiency of $5.09 \times 10^{-3} \pm 1.1 \times 10^{-4}$, while the second is $4.62 \times 10^{-3} \pm 9 \times 10^{-5}$, based on this values it can be concluded that the new geometry configuration will decrease the detection efficiency approximately 9%. Taking in account the advantage of the new configuration the efficiency lost was considered acceptable.

As mentioned in Chapter 1, factors such as the supporting structure of the detectors and the size of the shielding chamber will determine the flexibility, and the number of detectors that can be used. The new configuration has the disadvantage that only 3 detectors were used, see Figure 7.2 and Figure 7.3.

Other modifications where introduced between the first and the second measurement. In the first measurement detectors 3, 4 and, 6 were used together with an adjustable medical bed, see Figure 7.2. Because the first measurement it was observed that detector 6 presented an unusual high background below 30 keV, possibly due to a malfunction, this detector was replaced by detector 2 in the second and third measurements. An additional modification was the replacement of the adjustable medical bed by an electric adjustable medical chair, which improved the patient's comfort and allowed an easier positioning of the patient, see Figure 7.3.

Figure 7.2: HMGU PBC three detectors configuration used in the first measurement including an adjustable medical bed. On the left detector 3, in the middle detector 4, and on the top detector 6.
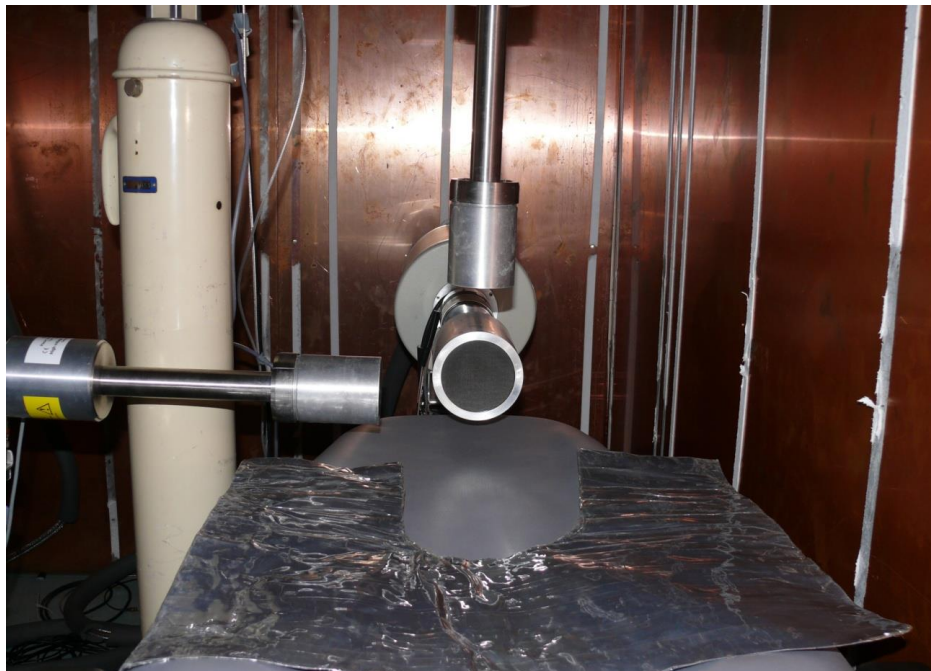
Figure 7.3: HMGU PBC three detectors configuration used in the second and third measurement, including an electric adjustable medical chair and the lead shielding also shown in Figure 7.1. On the left detector 3, in the middle detector 4, and on the top detector 2.

Before the first measurement, the head dimensions of Case 1 and Case 2 were measured with a plastic measuring tape and a big size caliper; the scalp thickness was estimated by bending the forehead skin, measuring this bend with the caliper, the dividing the results by 2, see Table 7.2.

Table 7.2: Case 1 and 2 head dimensions and scalp thickness measured on 23 May 2013.

Head Dimensions	Case 1	Case 2
Perimeter (mm), over the forehead and back of the head	600	570
Perimeter (mm), over the top of the head and under the chin	660	640
Half perimeter, top of one ear to the other one (mm)	320	310
Half perimeter, forehead to the back of the neck (mm)	400	400
X – Head width (mm)	191	192
Y – Head length (mm)	166	149
Z – Chin to top of the head (mm)	234	220
Forehead skin thickness (mm)	4	3.5

Before and after the measurements, the natural background inside the counting chamber from the adjustable medical bed or the electric adjustable medical chair and the lead body shielding was measured overnight for 50000 s, with the detectors already in the measurement configuration, see Figure 7.2 and Figure 7.3. Additionally, to validate the results obtained, the detectors efficiency was controlled using a ^{241}Am point source, while the energy calibration was verified using a ^{152}Eu point source and a ^{40}K source, this was done except in the first measurement.

Concerning the Case 1 and Case 2 measurements, as previously mentioned, the detectors were positioned at 1 cm distance from the head surface. Due to the different head sizes it was necessary to adjust the detector position for each case, see Figure 7.4 and Figure 7.5. The measurement time was defined based on the number of counts obtained in the first measurement.
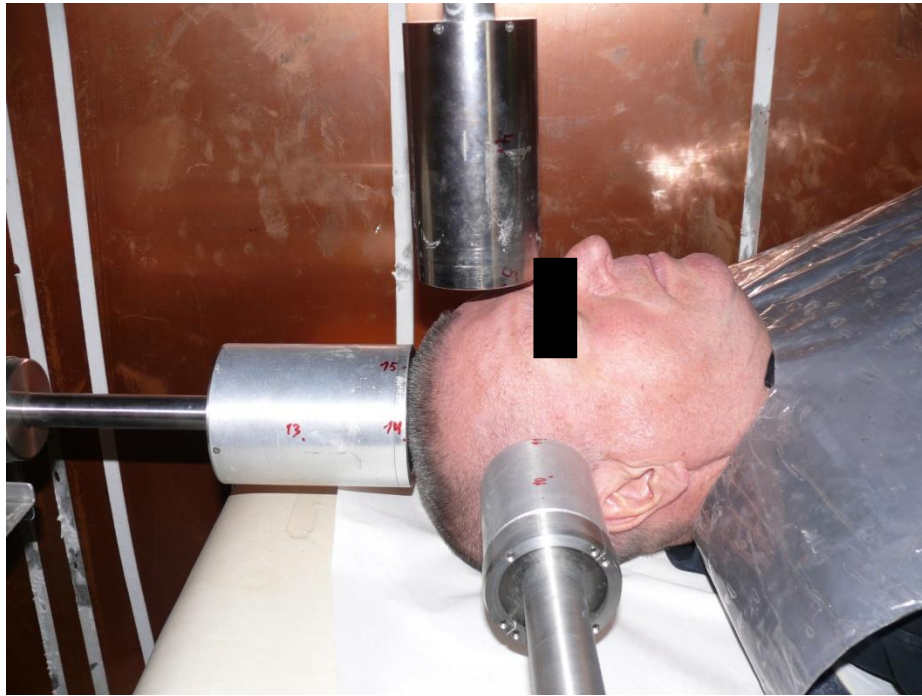
Figure 7.4: Case 1 first measurement at HMGU PBC using a three detectors configuration. On the left detector 4, on the right detector 3, and on the top detector 6.

Figure 7.5: Case 2 first measurement at HMGU PBC using a three detectors configuration. On the left detector 4, on the right detector 3, and on the top detector 6.

7.2 Results

The measurements were performed 35 days, 83 days and 151 days after the contamination date. In Figure 7.6 and Figure 7.7 the spectrum obtained in the first measurement of Case 1 head using detectors 3, 4 and 6 are shown. In all spectra the 59.54 keV full energy peak originated by the ^{241}Am is well defined with a high number of counts. However, it was not possible to distinguish the 26.34 keV full energy peak from the natural background counts, since at this energy, photons from the ^{241}Am decay are mainly absorbed by the human tissue and since the emission probability of 26.34 keV photons of ^{241}Am is low compared with that of 59.54 keV photons. Detector 6 is not shown because high background counts observed below 30 keV indicate that this detector had possibly a malfunction. The results of this detector were not used for further evaluation, after the first measurement and was replaced by detector 2 in the second and third measurements
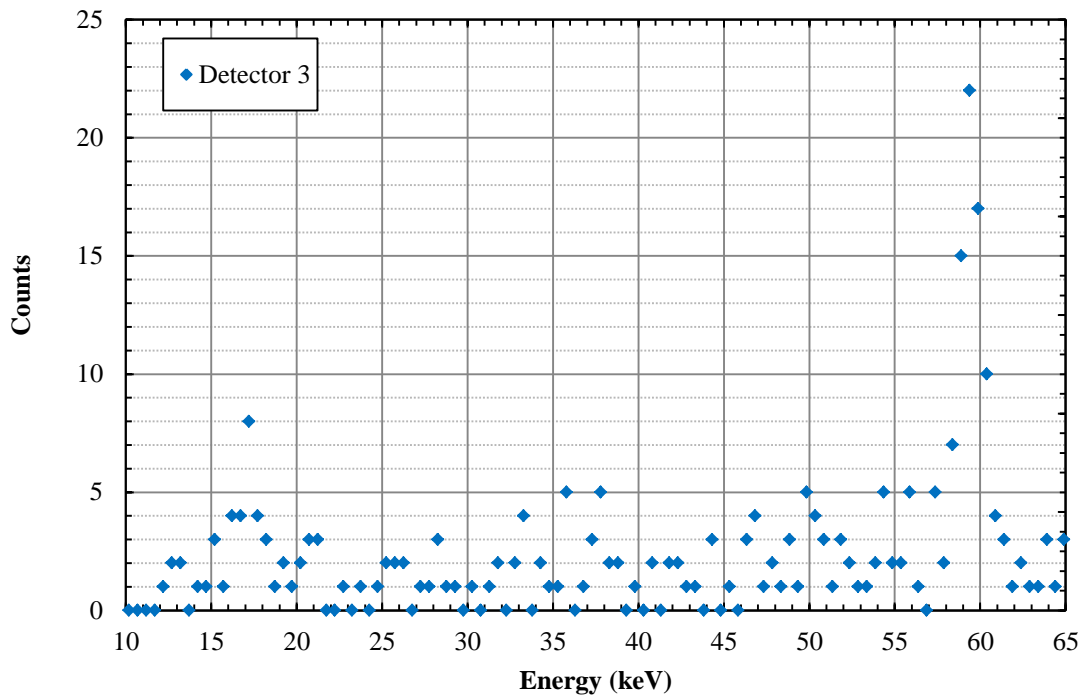
Figure 7.6: Detector 3 spectrum for a 1200 s measurement from the Case 1 head, detector positioned at the right side of the head, see Figure 7.4.
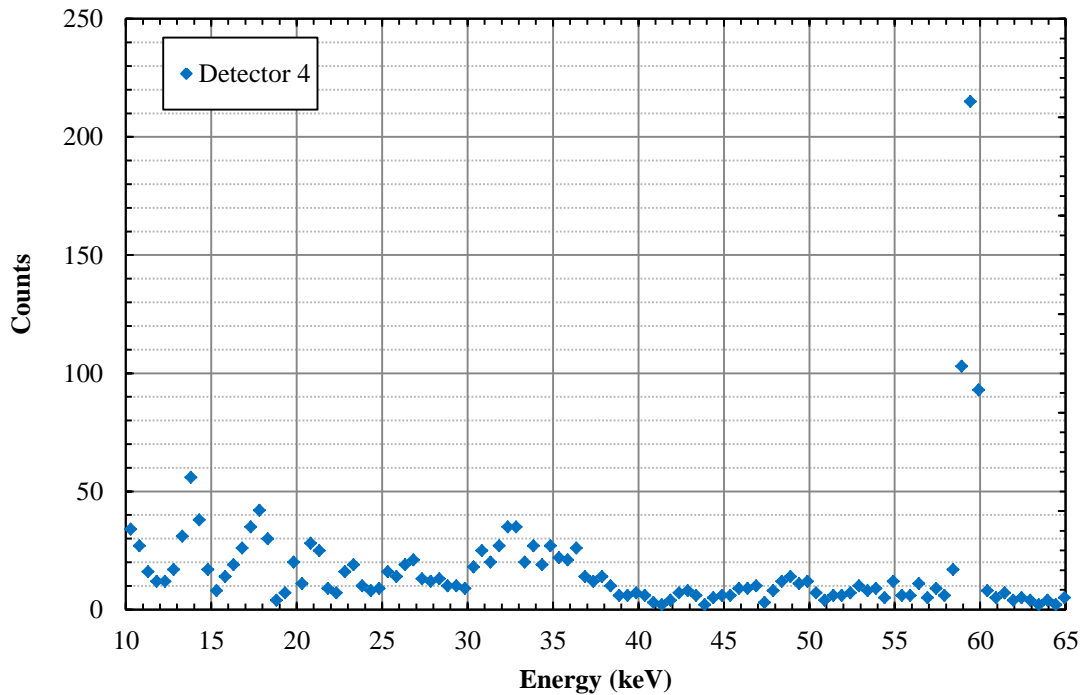
Figure 7.7: Detector 4 spectrum for a 1200 s measurement from the Case 1 skull, detector positioned at the top of the head, see Figure 7.4.

The control measurements using a ^{241}Am point source at 5 cm distance (to reduce the measurement dead time and counts pile-up) protected that the detection efficiency was the same before and after the measurements, except for the measurement on 10/7/2013 using detector 4. However the discrepancy observed was due to an unintentional displacement of the source during the control measurement.

The background values inside of the counting chamber for the second and third measurement campaigns are in agreement. However, compared with the first measurement the results detector 3 and 4 are approximately 30% and 15% higher, this is possibly due to a superior radioactive content from the construction materials such as ^{137}Cs of the electric adjustable medical chair compared with the adjustable medical bed used in the 1st measurement. This is confirmed by the increase of the number of counts from the ^{137}Cs 661 keV gamma between the first and second measurement, see Table 7.4. Relatively to the radon progeny contribution to the natural background the values measured indicates that there was no significant variation in its concentration. Note that detector 2 and 6 background measurements cannot be compared due to the different crystal sizes.

The increase of background counts in the region of interest as the consequence of increasing the MDA value (see Equation 2.1). The background increase due to the use of the electric adjustable medical chair was estimated to increase the MDA between 5% and 10%. Taking in account the advantages of the used of the chair, the small increase of the MDA was considered acceptable.

An additional validation of the measurements was obtained from the Case 1 and Case 2 measurement itself. The ^{40}K is a primordial radionuclide present in the human body and other living beings. The full energy peak counts from the ^{40}K gamma (1461 keV) can be easily seen in detector 4, however, not in detector 2 and 3, see Table 7.8 and Table 7.9. This is due to the detector 4 crystal higher thickness which increases this detector efficiency for higher energies. Based on the detector 4 spectrums it was estimated that the ^{40}K full energy peak count rate in the different measurements was approximately the same, and comparing the Case 1 and Case 2 average count rate per kg the results are similar, 3.4×10^{-4} (counts s^{-1} kg^{-1}) and 3.6×10^{-4} (counts s^{-1} kg^{-1}) respectively.

Table 7.3: Control measurements before and after the measurements, using a ^{241}Am point source to control the detection efficiency. The uncertainty is the one sigma counting statistics, and NE means no exiting value.

| | | | ^{241}Am Point source | | | |
| | | | Before | | After | |
Detector	Date	Time (s)	Counts	Uncer.	Counts	Uncer.
3	23/05/2013	250	NE	NE	NE	NE
4	23/05/2013	250	NE	NE	NE	NE
6	23/05/2013	250	NE	NE	NE	NE
3	10/07/2013	250	16491	129	16559	130
4	10/07/2013	250	31534	179	35523	190
2	10/07/2013	250	16499	130	16575	130
3	16/09/2013	250	17028	132	16929	132
4	16/09/2013	250	37280	195	36483	192
2	16/09/2013	250	16326	129	16609	130

Table 7.4: Natural Background measurement inside the chamber, in the 59.54 keV region of interest (ROI) and ^{137}Cs 661 keV full energy peak in the background measurement before and after the measurements, in both cases the measurement time was 50000 s. The uncertainty is the one sigma counting statistics and NE: means no exiting value.

| | | Background in the ROI area | | | | ^{137}Cs (661 keV) | | | |
| | | Before | | After | | Before | | After | |
Detector	Date	Counts	Uncer.	Counts	Uncer.	Counts	Uncer.	Counts	Uncer.
3	23/05/2013	303	17	270	16	22	10	18	7
4	23/05/2013	749	27	746	27	175	21	197	17
6	23/05/2013	881	30	925	30	NE	NE	NE	NE
3	10/07/2013	NE	NE	388	20	NE	NE	37	8
4	10/07/2013	NE	NE	900	30	NE	NE	319	22
2	10/07/2013	NE	NE	419	20	NE	NE	43	9
3	16/09/2013	404	20	387	20	35	9	35	8
4	16/09/2013	897	30	849	29	333	22	322	23
2	16/09/2013	390	20	368	19	45	9	50	11

7.3 Activity estimation

The activity content in the skull of Case 1 and Case 2 was estimated using the BfS phantom calibration factors. In Table 7.8 and Table 7.9 the measurement results obtained for Case 1 and Case 2 are shown, the activity was calculated using BfS phantom the calibration factors as measured without any correction except for the adding of 8% to the activity estimation uncertainty, due to the unknown [241]Am activity distribution in the bone present in Case 1 and Case 2, and taking in account the values of the USTUR case 102 phantom real activity distribution simulation, see Chapter 6.

In Figure 7.8 and Figure 7.9 the measured activity in the skulls of Case 1 and Case 2 is given as a function of time: for Case 1 there is an excellent agreement between the results obtained using different detectors with all values differences below a 2 sigma uncertainty, except for the first measurement results; for Case 2 there is also an excellent agreement between the measurements with all values differences below a 2 sigma uncertainty, the values obtained for this case are lower compared with previous possibly due to the fact it was the second to be contaminated. In both cases there is a reduction of the activity measured in function of the time.

The MDA was calculated for [241]Am (59.54 keV) using the Formula 2.1 (see Chapter 2) for the same measurements conditions of Case 1 and Case 2, using the BfS phantom for calibration and the average of three non-contaminated person's measurements, see Table 7.5, Table 7.6 and Table 7.7. For Case 1, with exception for detector 2 results, all values measured and the sums of all measurements positions are above the respective MDA. For Case 2, the all third measurement values and second measurement detector 4 and detector 2 results are below detection system MDA, which means that the activity present is not sufficiently large to generate a number of counts that we can be confident to detect taking in account a 95% confidence level (Gilmore 2008). However, because the MDA (minimum detectable activity) is not the minimum activity detectable it is possible to measure an activity below this decision limit (Gilmore 2008). In this case it is required to calculate the detection system critical limit (L_C), which determines if the observed counts are statistical significant. This decision limit can be calculated following the methods developed by Currie (1968) where it is defined for a 95% confidence level as:

$$L_c = 2.33 s_b \qquad\qquad 7.1$$

where s_b is the standard deviation of the number of counts for repeated measurements of a blank, in the same region of the full energy peak FHWM (Currie 1968).

The L_C values calculated for the same measurements conditions of Case 2, using the average of three non-contaminated person's measurements (see Table 7.7), show that the number of net counts obtained for Case 2 second measurement using detector 4 and detector 2 are above the L_C; for the third measurement only the detector 4 results are above the L_C, however, the sum of detectors 2, 3 and 4 spectrums is above the L_C, see Table 7.9.

Table 7.5: Photon energy, respective probability emission, detectors FWHM and background counts in the same region of the full energy peak FWHM for the average of three non-contaminated persons measurements.

^{241}Am	Detector							
	2	Uncer.	3	Uncer.	4	Uncer.	6	Uncer.
Energy (keV)	59.54		59.54		59.54		59.54	
p (%)	35.92	0.17	35.92	0.17	35.92	0.17	35.92	0.17
FWHM (channel)	3		4		3		3	
Background (cps)($\cdot 10^{-3}$)	6.00	2.45	8.19	2.13	12.8	2.7	19.2	3.3

Table 7.6: MDA and L_D calculated with Formula 2.1 (see Chapter 2) for ^{241}Am (59.54 keV) using BfS skull phantom, the blank is an average of 3 persons, a 1200 s measurement time, and the three detectors measurement geometry.

BfS Phantom	Single detector								Multiple detectors configuration			
Time 1200 s	2	Uncer.	3	Uncer.	4	Uncer.	6	Uncer.	2 - 3 - 4	Uncer.	3 - 4	Uncer.
Efficiency	$6.53 \cdot 10^{-3}$	$1.6 \cdot 10^{-4}$	$9.06 \cdot 10^{-3}$	$2.2 \cdot 10^{-4}$	$2.36 \cdot 10^{-2}$	$5.5 \cdot 10^{-4}$	-	-	$3.92 \cdot 10^{-2}$	$6.1 \cdot 10^{-4}$	$3.27 \cdot 10^{-2}$	$5.9 \cdot 10^{-4}$
L_D (counts)	15.48	3.16	17.58	2.29	21.21	2.21	-	-	29.45	2.29	26.33	2.14
MDA (Bq)	5.50	1.42	4.50	0.91	2.08	0.38	-	-	1.74	0.26	1.87	0.29

Table 7.7: MDA and L_D calculated with Formula 2.1 (see Chapter 2) and L_C calculated with Formula 7.1, for ^{241}Am (59.54 keV) using BfS case 102 skull phantom, the blank is an average of 3 persons, a 3000 s measurement time, and the three detectors measurement geometry.

BfS Phantom	Single detector								Multiple detectors configuration			
Time 3000 s	2	Uncer.	3	Uncer.	4	Uncer.	6	Uncer.	2 - 3 - 4	Uncer.	3 - 4	Uncer.
Efficiency	$6.53 \cdot 10^{-3}$	$1.6 \cdot 10^{-4}$	$9.06 \cdot 10^{-3}$	$2.2 \cdot 10^{-4}$	$2.36 \cdot 10^{-2}$	$5.5 \cdot 10^{-4}$	-	-	$3.92 \cdot 10^{-2}$	$6.1 \cdot 10^{-4}$	$3.27 \cdot 10^{-2}$	$5.9 \cdot 10^{-4}$
L_D (counts)	22.73	4.64	26.06	3.39	31.79	3.31	-	-	44.83	3.49	39.88	3.25
MDA (Bq)	3.23	0.83	2.67	0.54	1.25	0.23	-	-	1.06	0.16	1.13	0.18
L_C (counts)	9.89	2.02	11.55	1.50	14.43	1.50	-	-	20.96	1.63	18.48	1.50

Table 7.8: Case 1 measurement results obtained with HMGU PBC in the 3 detectors configuration (see Figure 7.4), and activity estimation using BfS phantom for calibration. Counts uncertainty is the statistical count uncertainty; the detection efficiency uncertainty corresponds to the Gaussian propagation of the counts uncertainty, the emission probability uncertainty, and the phantom activity uncertainty. The activity estimation uncertainty corresponds to the Gaussian propagation of the counts uncertainty, the detection efficiency uncertainty and 8% uncertainty due to the activity distribution in the skull surface.

		Case 1 59.54 keV full energy peak results				BfS phantom		Case 1 skull activity estimation (Bq)		^{40}K (1461 keV)	
Detector	Date	Time (s)	Counts Brut	Counts Net	Counts Net uncertainty	Detection efficiency	Uncertainty	Activity (Bq)	Uncertainty	Counts Net	Counts uncertainty
3	23/05/2013	1200	89	65	11	$9.06 \cdot 10^{-3}$	$2.2 \cdot 10^{-4}$	16.6	3.0	0	NA
4	23/05/2013	1200	481	409	24	$2.36 \cdot 10^{-2}$	$5.5 \cdot 10^{-4}$	40.1	2.7	44	7
6	23/05/2013	1200	-	-	-	-	-	-	-	NE	NE
Sum 3 4	23/05/2013	1200	570	474	26	$3.27 \cdot 10^{-2}$	$5.9 \cdot 10^{-4}$	33.6	2.1	-	-
3	10/07/2013	1200	68	35	10	$9.06 \cdot 10^{-3}$	$2.2 \cdot 10^{-4}$	9.0	2.8	5	2
4	10/07/2013	1200	77	27	11	$2.36 \cdot 10^{-2}$	$5.5 \cdot 10^{-4}$	2.7	1.2	41	6
2	10/07/2013	1200	26	4	7	$6.53 \cdot 10^{-3}$	$1.6 \cdot 10^{-4}$	1.4	2.7	0	NA
Sum 2 3 4	10/07/2013	1200	171	66	17	$3.92 \cdot 10^{-2}$	$6.1 \cdot 10^{-4}$	3.9	1.1	-	-
3	16/09/2013	3000	112	42	13	$9.06 \cdot 10^{-3}$	$2.2 \cdot 10^{-4}$	4.3	1.5	11	3
4	16/09/2013	3000	215	63	19	$2.36 \cdot 10^{-2}$	$5.5 \cdot 10^{-4}$	2.5	0.8	88	9
2	16/09/2013	3000	71	11	11	$6.53 \cdot 10^{-3}$	$1.6 \cdot 10^{-4}$	1.6	1.8	4	3
Sum 2 3 4	16/09/2013	3000	398	116	26	$3.92 \cdot 10^{-2}$	$6.1 \cdot 10^{-4}$	2.7	0.7	-	-

Table 7.9: Case 2 measurement results obtained with HMGU PBC in the 3 detectors configuration (see Figure 7.5), and activity estimation using BfS phantom for calibration. Counts uncertainty is the statistical count uncertainty; the detection efficiency uncertainty corresponds to the Gaussian propagation of the counts uncertainty, the emission probability uncertainty, and the phantom activity uncertainty. The activity estimation uncertainty corresponds to the Gaussian propagation of the counts uncertainty, the detection efficiency uncertainty and 8% uncertainty due to the activity distribution in the skull surface.

		Case 2 59.54 keV full energy peak results				BfS phantom		Case 2 skull activity estimation (Bq)		^{40}K (1461 keV)	
Detector	Date	Time (s)	Counts Brut	Counts Net	Counts Net uncertainty	Detection efficiency	Uncertainty	Activity (Bq)	Uncertainty	Counts Net	Counts uncertainty
3	23/05/2013	3000	130	65	14	$9.06 \cdot 10^{-3}$	$2.2 \cdot 10^{-4}$	6.7	1.6	13	3
4	23/05/2013	3000	212	99	18	$2.36 \cdot 10^{-2}$	$5.5 \cdot 10^{-4}$	3.9	0.8	73	8
6	23/05/2013	3000	-	-	-	-	-	-	-	-	-
Sum 3 4	23/05/2013	3000	342	164	23	$3.27 \cdot 10^{-2}$	$5.9 \cdot 10^{-4}$	4.7	0.7	-	-
3	10/07/2013	3000	74	33	11	$9.06 \cdot 10^{-3}$	$2.2 \cdot 10^{-4}$	3.4	1.2	12	3
4	10/07/2013	3000	123	15	15	$2.36 \cdot 10^{-2}$	$5.5 \cdot 10^{-4}$	0.6	0.6	67	8
2	10/07/2013	3000	46	11	9	$6.53 \cdot 10^{-3}$	$1.6 \cdot 10^{-4}$	1.6	1.4	9	3
Sum 2 3 4	10/07/2013	3000	243	59	21	$3.92 \cdot 10^{-2}$	$6.1 \cdot 10^{-4}$	1.4	0.5	-	-
3	16/09/2013	3000	85	7	13	$9.06 \cdot 10^{-3}$	$2.2 \cdot 10^{-4}$	0.7	1.4	9	4
4	16/09/2013	3000	134	15	16	$2.36 \cdot 10^{-2}$	$5.5 \cdot 10^{-4}$	0.6	0.7	81	9
2	16/09/2013	3000	58	3	11	$6.53 \cdot 10^{-3}$	$1.6 \cdot 10^{-4}$	0.4	1.6	0	NA
Sum 2 3 4	16/09/2013	3000	277	25	23	$3.92 \cdot 10^{-2}$	$6.1 \cdot 10^{-4}$	0.6	0.6	-	-
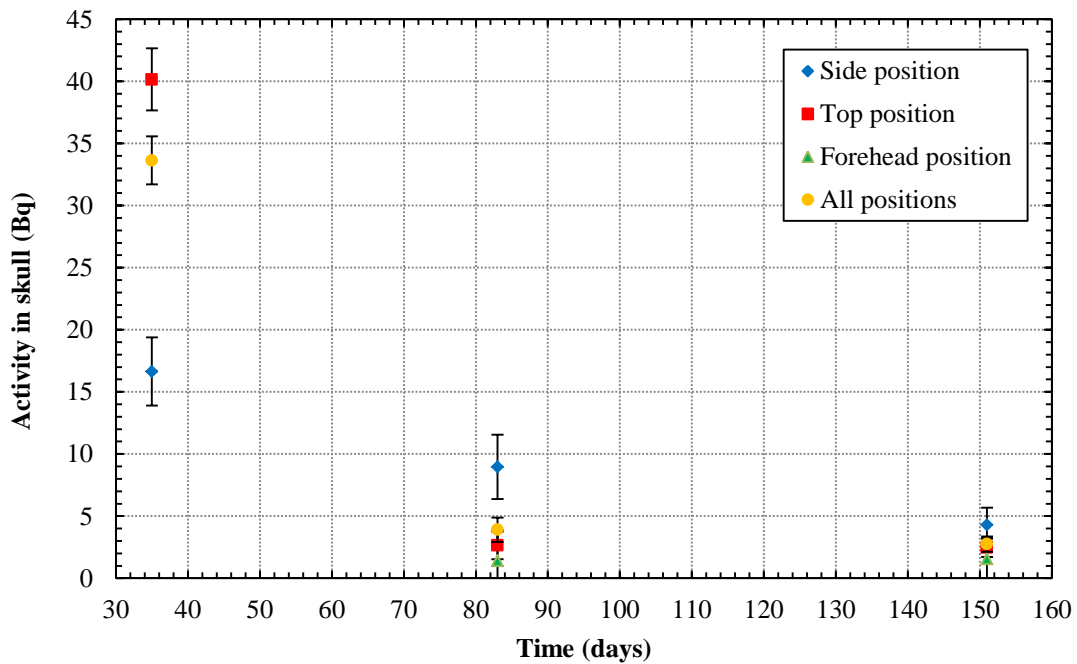
Figure 7.8: Case 1 activity measured in the skull function of the time after the contamination using the BfS phantom calibration. The error bars correspond to the one sigma uncertainty obtained from the Gaussian propagation of the statistical count uncertainty, the emission probability uncertainty, the BfS phantom activity uncertainty, and the activity distribution uncertainty.
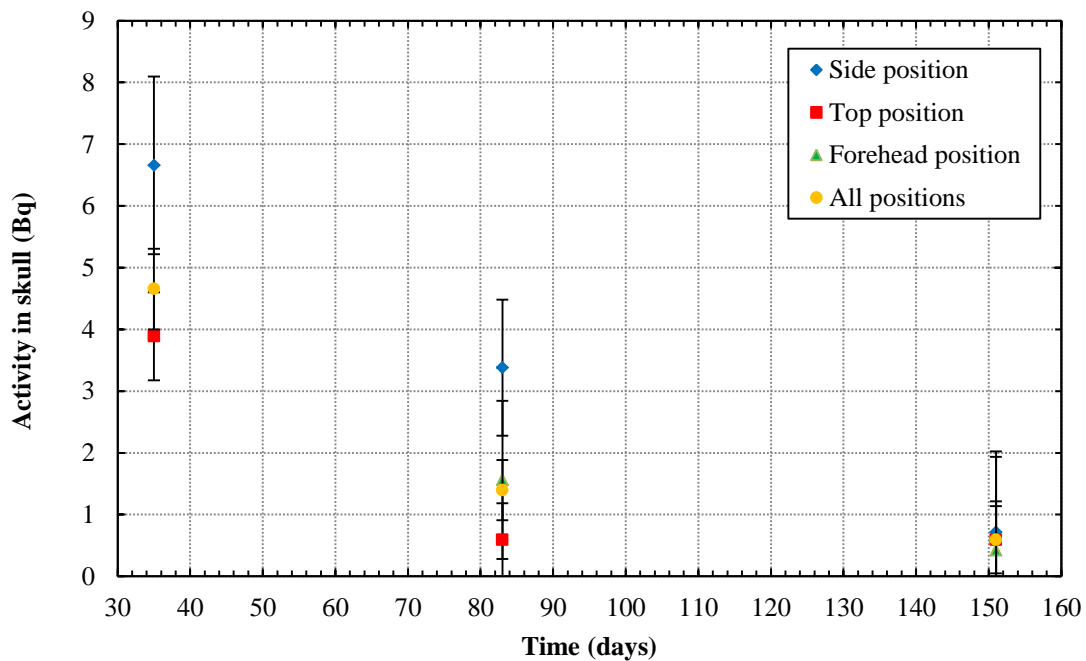
Figure 7.9: Case 2 activity measured in the skull function of the time after the contamination using the BfS phantom calibration. The error bars correspond to the one sigma uncertainty obtained from the Gaussian propagation of the statistical count uncertainty, the emission probability uncertainty, the BfS phantom activity uncertainty, and the activity distribution uncertainty.

7.4 Correction factors

The correction factors for critical head parameters calculated using the Max-06 voxel phantom and Monte Carlo methods (see Chapter 6) were applied to personalize the BfS phantom and the Max-06 phantom efficiency calibration for Case 1 and Case 2 head parameters.

Assuming that the influence on the detection efficiency from the head dimensions is independent of the detector crystal size the correction factors previously calculated for detector 3 at the side position of the head can be applied to all other detectors with exception for the shape correction factor, see Table 7.10 and Table 7.11. This assumption is possible because the scalp correction factor depends mainly on the thickness of absorption material over the skull bone; the cortical to trabecular bone correction factor depends only on the time after exposition, this assuming that the ratio between trabecular bone and cortical bone quantity is constant in different bones of the skull; also the size correction factor being base on an average radius of the X Y and Z dimension of the head will also not be dependent on the measurement position. Only the shape correction factor will be dependent on the measurement position because the head is not a sphere and has it was observed in simulation for extreme cases of head shapes the main contribution to the efficiency variation is the contribution of the opposite side to the measurement position.

Concerning the scalp correction factors since no values of scalp thickness are available for the side and top of the head of Case 1 and Case 2, the Max-06 phantom scalp thickness values were used to calculate the correction factors at these positions, see Table 6.2.

Table 7.10: Detection efficiency obtained with BfS phantom and application of the correction factors calculated in Chapter 6 for Case 1. The detection efficiency uncertainty corresponds to the Gaussian propagation of the counts uncertainty, the emission probability uncertainty, and the phantom activity uncertainty. The activity estimation uncertainty corresponds to the Gaussian propagation of the counts uncertainty, the detection efficiency uncertainty, and 8% uncertainty due to the activity distribution in skull surface.

№	Position	Time after exposure	Efficiency measured	Uncer.	K1 Cortical and trabecular bone	K2 Skin thickness	K3 Head size	K4 Head shape	Ktotal	Efficiency corrected for Case 1	Uncer.	Activity (Bq)	Uncer.
	Detector		BfS Phantom		Correction factors					BfS Phantom		Case 1 skull activity estimation (Bq)	
3	Right side	35	$9.06 \cdot 10^{-3}$	$2.2 \cdot 10^{-4}$	0.788	0.636 [a]	0.683	0.995	0.341	$3.09 \cdot 10^{-3}$	$7.4 \cdot 10^{-5}$	48.9	8.7
4	Top	35	$2.36 \cdot 10^{-2}$	$5.5 \cdot 10^{-4}$	0.788	1.101 [a]	0.683	-	0.593	$1.40 \cdot 10^{-2}$	$3.2 \cdot 10^{-4}$	67.7	4.5
6	Forehead	35	-	-	0.788	1.129	0.683	-	0.608	-	-	-	-
	Sum 3 4	35	$3.27 \cdot 10^{-2}$	$5.9 \cdot 10^{-4}$	-	-	-	-	-	$1.71 \cdot 10^{-2}$	$3.3 \cdot 10^{-4}$	64.3	4.0
3	Right side	83	$9.06 \cdot 10^{-3}$	$2.2 \cdot 10^{-4}$	0.790	0.636 [a]	0.683	0.995	0.341	$3.09 \cdot 10^{-3}$	$7.4 \cdot 10^{-5}$	26.2	8.2
4	Top	83	$2.36 \cdot 10^{-2}$	$5.5 \cdot 10^{-4}$	0.790	1.101 [a]	0.683	-	0.594	$1.40 \cdot 10^{-2}$	$3.2 \cdot 10^{-4}$	4.5	2.0
2	Forehead	83	$6.53 \cdot 10^{-3}$	$1.6 \cdot 10^{-4}$	0.790	1.129	0.683	-	0.609	$3.98 \cdot 10^{-3}$	$9.8 \cdot 10^{-5}$	2.3	4.4
	Sum 2 3 4	83	$3.92 \cdot 10^{-2}$	$6.1 \cdot 10^{-4}$	-	-	-	-	-	$2.11 \cdot 10^{-2}$	$3.5 \cdot 10^{-4}$	7.3	2.0
3	Right side	151	$9.06 \cdot 10^{-3}$	$2.2 \cdot 10^{-4}$	0.793	0.636 [a]	0.683	0.995	0.343	$3.10 \cdot 10^{-3}$	$7.4 \cdot 10^{-5}$	12.6	4.4
4	Top	151	$2.36 \cdot 10^{-2}$	$5.5 \cdot 10^{-4}$	0.793	1.101 [a]	0.683	-	0.596	$1.41 \cdot 10^{-2}$	$3.3 \cdot 10^{-4}$	4.1	1.4
2	Forehead	151	$6.53 \cdot 10^{-3}$	$1.6 \cdot 10^{-4}$	0.793	1.129	0.683	-	0.611	$3.99 \cdot 10^{-3}$	$9.8 \cdot 10^{-5}$	2.6	2.9
	Sum 2 3 4	151	$3.92 \cdot 10^{-2}$	$6.1 \cdot 10^{-4}$	-	-	-	-	-	$2.12 \cdot 10^{-2}$	$3.5 \cdot 10^{-4}$	5.1	1.2

[a] – Correction factor for skin based on the thickness values from the BfS phantom: 16.8 mm on the right side and 3.6 mm on the head top.

Table 7.11: Detection efficiency obtained with BfS phantom and application of the correction factors calculated in Chapter 6 for Case 2. The detection efficiency uncertainty corresponds to the Gaussian propagation of the counts uncertainty, the emission probability uncertainty, and the phantom activity uncertainty. The activity estimation uncertainty corresponds to the Gaussian propagation of the counts uncertainty, the detection efficiency uncertainty, and 8% uncertainty due to the activity distribution in skull surface.

| Detector | | | BfS Phantom | | Correction factors | | | | | BfS Phantom | | Case 2 skull activity estimation (Bq) | |
№	Position	Time after exposure	Efficiency measured	Uncer.	K1 Cortical and trabecular bone	K2 Skin thickness	K3 Head size	K4 Head shape	Ktotal	Efficiency corrected for Case 2	Uncer.	Activity (Bq)	Uncer.
3	Right side	35	$9.06 \cdot 10^{-3}$	$2.2 \cdot 10^{-4}$	0.788	0.636 [a]	0.765	1.005	0.385	$3.49 \cdot 10^{-3}$	$8.4 \cdot 10^{-5}$	17.3	4.0
4	Top	35	$2.36 \cdot 10^{-2}$	$5.5 \cdot 10^{-4}$	0.788	1.101 [a]	0.765	-	0.664	$1.57 \cdot 10^{-2}$	$3.6 \cdot 10^{-4}$	5.9	1.2
6	Forehead	35	-	-	0.788	1.152	0.765	-	0.694	-	-	-	-
	Sum 3 4	35	$3.27 \cdot 10^{-2}$	$5.9 \cdot 10^{-4}$	-	-	-	-	-	$1.92 \cdot 10^{-2}$	$3.7 \cdot 10^{-4}$	7.9	1.2
3	Right side	83	$9.06 \cdot 10^{-3}$	$2.2 \cdot 10^{-4}$	0.790	0.636 [a]	0.765	1.005	0.386	$3.50 \cdot 10^{-3}$	$8.4 \cdot 10^{-5}$	8.8	3.1
4	Top	83	$2.36 \cdot 10^{-2}$	$5.5 \cdot 10^{-4}$	0.790	1.101 [a]	0.765	-	0.665	$1.57 \cdot 10^{-2}$	$3.6 \cdot 10^{-4}$	0.9	1.0
2	Forehead	83	$6.53 \cdot 10^{-3}$	$1.6 \cdot 10^{-4}$	0.790	1.152	0.765	-	0.696	$4.55 \cdot 10^{-3}$	$1.1 \cdot 10^{-4}$	2.2	2.0
	Sum 2 3 4	83	$3.92 \cdot 10^{-2}$	$6.1 \cdot 10^{-4}$	-	-	-	-	-	$2.38 \cdot 10^{-2}$	$3.9 \cdot 10^{-4}$	2.3	0.9
3	Right side	151	$9.06 \cdot 10^{-3}$	$2.2 \cdot 10^{-4}$	0.793	0.636 [a]	0.765	1.005	0.387	$3.51 \cdot 10^{-3}$	$8.4 \cdot 10^{-5}$	1.9	3.6
4	Top	151	$2.36 \cdot 10^{-2}$	$5.5 \cdot 10^{-4}$	0.793	1.101 [a]	0.765	-	0.667	$1.58 \cdot 10^{-2}$	$3.6 \cdot 10^{-4}$	0.9	1.0
2	Forehead	151	$6.53 \cdot 10^{-3}$	$1.6 \cdot 10^{-4}$	0.793	1.152	0.765	-	0.698	$4.56 \cdot 10^{-3}$	$1.1 \cdot 10^{-4}$	0.6	2.3
	Sum 2 3 4	151	$3.92 \cdot 10^{-2}$	$6.1 \cdot 10^{-4}$	-	-	-	-	-	$2.38 \cdot 10^{-2}$	$3.9 \cdot 10^{-4}$	1.0	1.0

[a] – Correction factor for skin based on the thickness values from the BfS phantom: 16.8 mm on the right side and 3.6 mm on the head top.
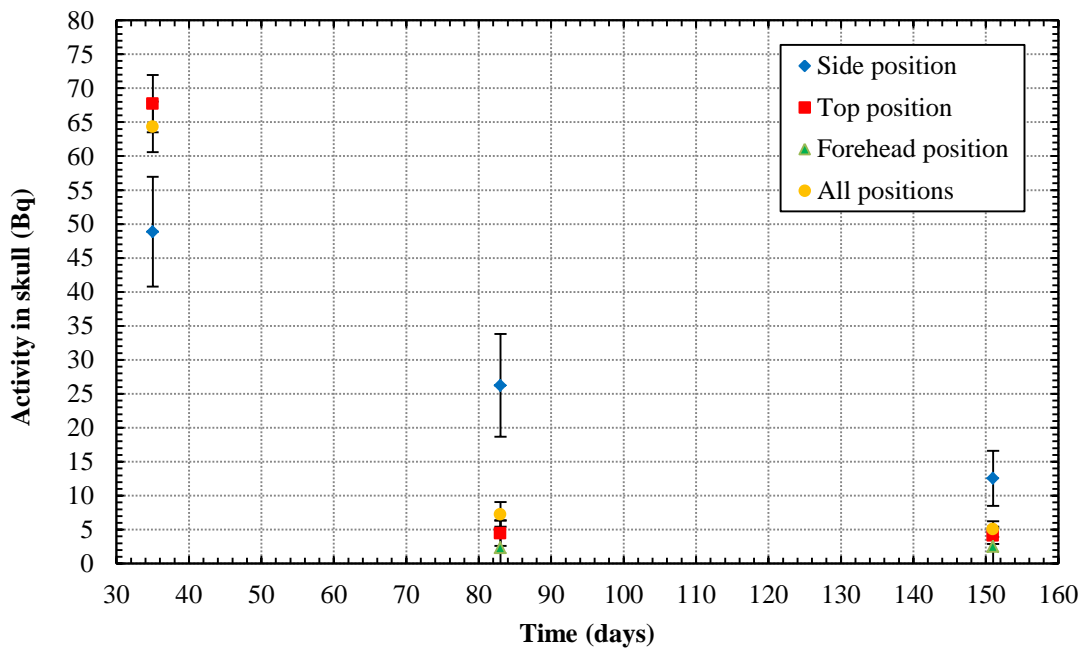
Figure 7.10: Case 1 activity measured in the skull function of the time after the contamination using the BfS phantom calibration together with correction factors for the critical head parameter from Case 1. The error bars correspond to the one sigma uncertainty obtained from the Gaussian propagation of the statistical count uncertainty, the emission probability uncertainty, the BfS phantom activity uncertainty, and the activity distribution uncertainty.
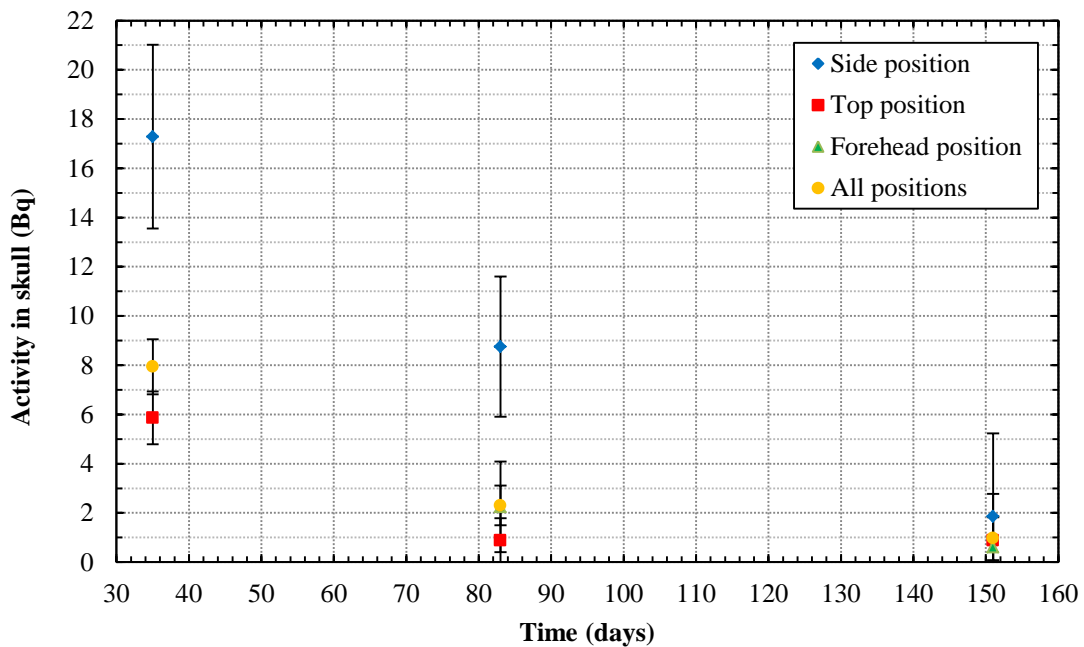
Figure 7.11: Case 2 activity measured in the skull function of the time after the contamination using BfS phantom calibration together with correction factors for the critical head parameter from Case 2. The error bars correspond to the one sigma uncertainty obtained from the Gaussian propagation of the statistical count uncertainty, the emission probability uncertainty, the BfS phantom activity uncertainty, and the activity distribution uncertainty.

7.5 Estimation of Dose

The total ^{241}Am skeleton content can then be estimated through the method developed by Cohen, Spitz et al. (1977), in which it is assumed that the ^{241}Am is uniformly distributed in the mineral mass (bone and teeth), and since the head represents 15.7% (ICRP-89 2002) of the mineral mass and it consequently contains 15.7% of the ^{241}Am deposited in the skeleton. The activity content values were calculated for the detectors spectra sum after applying the correction factors for the personalized calibration, see Table 7.12 and Table 7.14 .

For the estimation of the Case 1 and Case 2 activity intake and effective dose, the use of biokinetic models is required. At BfS, based on lung measurements, whole body measurements, and *in vitro* assays of urine samples, it was found that the biokinetic model for an inhalation absorption type S, AMAD 1 μm, following an acute intake, is the biokinetic model that fits best with the experimental results (Giussani 2013), see Figure 7.12. Below the retention curve for the skeleton calculated by Klaus Karcher using the BfS software DOSAGE (Noßke and Karcher 2014), which is used for quality assurance of the ICRP models, was used to estimate the ^{241}Am intake. The effective dose was also calculated using this model the dose coefficient for 50 years of 1.47×10^{-5} Sv Bq^{-1} and the dose coefficient for the first year of 5.36×10^{-6} Sv Bq^{-1} (Giussani 2013), see Table 7.13 and Table 7.15.
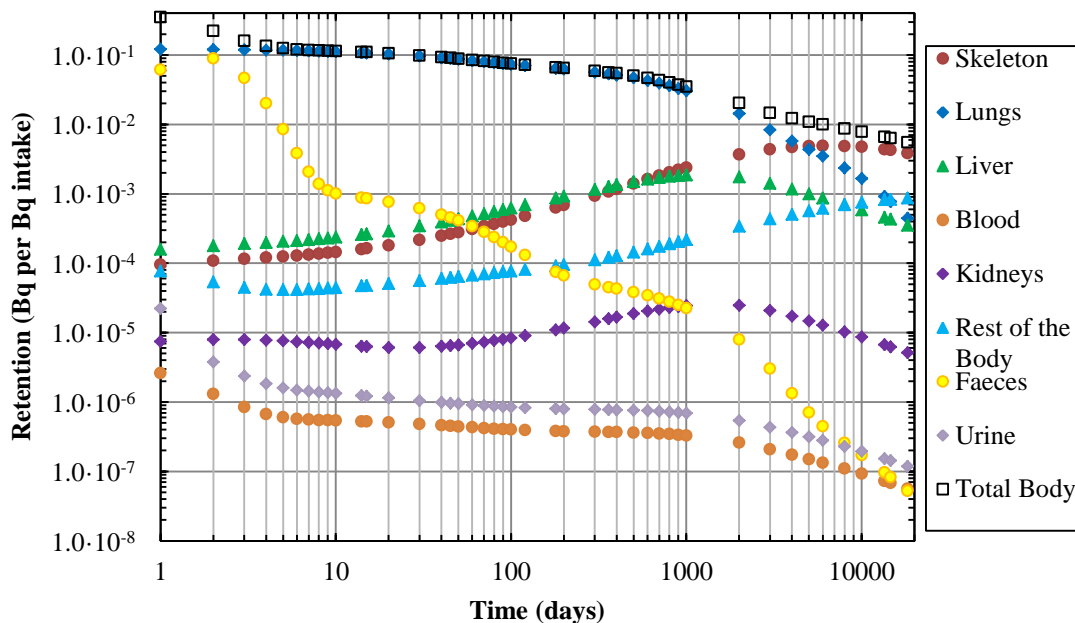
Figure 7.12: Retention curves for ^{241}Am inhalation absorption type S, AMAD 1 μm, following an acute intake; values calculated using the BfS software DOSAGE (Noßke and Karcher 2014) by Klaus Karcher (Giussani 2013).

Table 7.12: Case 1 ^{241}Am activity in the skull bone estimated using the BfS phantom and personalized correction factors, and extrapolation of the activity in the complete skeleton assuming that the skull bone contains 15.7% of the mineral bone mass from the total skeleton.

Detectors sum	Time after exposure (d)	Activity (Bq)			
		Skull	Uncertainty	Skeleton	Uncertainty
3-4	35	64.3	4.0	409.7	25.5
3-4-2	83	7.3	2.0	46.2	12.7
3-4-2	151	5.1	1.2	32.4	7.6

Table 7.13: Case 1 ^{241}Am activity intake and dose estimation, using the retention curve in skeleton (see Figure 7.12) calculated by Klaus Karcher (Giussani 2013) for a biokinetic model for an inhalation absorption type S, AMAD 1 μm, following an acute intake (inhalation).

Detector	Time after exposure (d)	Retention in skeleton (Bq per Bq intake)	BfS calibration		
			Activity intake (Bq)	Dose 50 years (Sv)	Dose in the first year (Sv)
3-4	35	$2.30 \cdot 10^{-4}$	$1.78 \cdot 10^{+6}$	26.18	9.55
3-4-2	83	$3.74 \cdot 10^{-4}$	$1.23 \cdot 10^{+5}$	1.82	0.66
3-4-2	151	$5.56 \cdot 10^{-4}$	$5.82 \cdot 10^{+4}$	0.86	0.31

Table 7.14: Case 2 ^{241}Am activity in the skull bone estimated using the BfS phantom and personalized correction factors, and extrapolation of the activity in the complete skeleton assuming that the skull bone contains 15.7% of the mineral bone mass from the total skeleton.

Detector	Time after exposure (d)	Activity (Bq)			
		Skull	Uncertainty	Skeleton	Uncertainty
3-4	35	7.9	1.2	50.6	7.6
3-4-2	83	2.3	0.9	14.7	5.7
3-4-2	151	1.0	1.0	6.2	6.4

Table 7.15: Case 2 ^{241}Am activity intake and dose estimation, using the retention curve in skeleton (see Figure 7.12) calculated by Klaus Karcher (Giussani 2013) for a biokinetic model for an inhalation absorption type S, AMAD 1 μm, following an acute intake (inhalation).

Detector	Time after exposure (d)	Retention in skeleton (Bq per Bq intake)	BfS calibration		
			Activity intake (Bq)	Dose 50 years (Sv)	Dose in the first year (Sv)
3-4	35	$2.30 \cdot 10^{-4}$	$2.20 \cdot 10^{+5}$	3.23	1.18
3-4-2	83	$3.74 \cdot 10^{-4}$	$3.92 \cdot 10^{+4}$	0.58	0.21
3-4-2	151	$5.56 \cdot 10^{-4}$	$1.11 \cdot 10^{+4}$	[a]0.16	[a]0.06

[a] – Dose values based on activity values that are below the detection system MDA.

For both cases the dose values calculated are significantly different depending on the measurement time after the exposure. The differences are mainly due to the decrease of the measured activity as a function of time, see Figure 7.10 and Figure 7.11. This decrease is in contradiction with the calculated retention curves for [241]Am which predicts an increase of the [241]Am activity in the bone as a function of time, see Figure 7.12.

The reason for the contradiction between experimental and theoretical values is possibly due to the short time between the measurements and the exposure. Generally skull measurements are performed several years after the incorporation, when the [241]Am is mainly localized in the skeleton, lungs and liver, thus the use in skull measurements of calibration phantoms where only the skull bone is contaminated. However, for Case 1 and Case 2 the measurements were performed only some months after the exposure and as a consequence there is still possibly a great [241]Am activity present in soft tissues such as the brain, the adipose or the muscle tissue. The excretion of the [241]Am activity from these soft tissues would explain the rapid decrease of the measured activity between the measurement campaigns, see Figure 7.10 and Figure 7.11. Unfortunately this cannot be confirmed since no retention curves are available for these soft tissues, because they are not source organs in the ICRP model (Giussani 2013). Additionally, the available skull calibration does not contain any contribution from an additional contamination of soft tissue.

Taking into account the previous arguments the best estimations of the effective dose for 50 years are based on the last measurements thus 0.86 Sv for Case 1 and 0.16 Sv for Case 2, however, note that Case 2 dose estimation is based in an activity value below the detection system MDA, and thus not within the 95% confidence level, but this measurement number of counts is above the detection system decision limit L_C. Additionally it is noted, that there might be additional contribution to the dose from the first few weeks for both cases.

7.6 Conclusion

Accidental exposures such as reported in this work demonstrate that preparedness is fundamental in the field of radiation protection. The correction factors calculated through Monte Carlo simulations together with anthropomorphic phantoms in Chapter 6 allowed performing a "individual-specific" calibration of the HMGU partial body counter for Case 1 and Case 2 critical body parameters. As a result, estimated incorporated activities are 1.6 and 1.9 times larger than those estimated using the BfS anthropomorphic phantom without applying any correction for person-specific parameters.

To determine the Case 1 and Case 2 effective dose, ^{241}Am biokinetic retention curves calculated at the BfS were used. These dose estimations revealed that skull measurements in recent exposures should take into account that possibly there is still a great ^{241}Am activity present in soft tissues such as the brain, the adipose or the muscle tissue. Since typical calibration skull phantoms have only contaminated bone, this could result in a bias of the dose estimation. As can be observed the Case 1 and Case 2 dose estimations based in the first measurement are 6 to 8 times superior compared to estimations based in latter measurements. As future work Monte Carlo simulations and anthropomorphic phantoms should be used determine the impact in detection efficiency from the ^{241}Am present in the soft tissues and provide correction factors for this effect.

8 Conclusions and Outlook

In this work, the Helmholtz Center Munich partial body counter has been specifically calibrated for two real human accidental exposures to ^{241}Am incorporation. This personalized calibration allowed to improve the estimation of the incorporated activity and the corresponding internal dose by values up 1.6 and 1.9 times larger than those estimated without applying any correction for person-specific parameters.

To achieve this, the Helmholtz Center Munich partial body counter was calibrated using three skull phantoms from nine available world-wide, and the measurements were validated by participation in the first world-wide *in-vivo* skull measurements intercomparison coordinated by the Author and promoted through the European Radiation Dosimetry Group network.
Having the measurements validate, to study the partial body counter detection efficiency of low-energy photons, a computational set-up of one germanium detector was developed for Monte Carlo simulations using the GEANT4 code, and validate by comparison with measurement results and the MCNPX Monte Carlo code.
Finally the head of the Max-06 voxel phantom, a computational anthropomorphic phantom that was produced from human anatomical cross-sectional images, together with the GEANT4 Monte Carlo code was used to study critical body parameters. The results revealed that parameters such as the time after the internal contamination and the mean head radius size, can change significantly the detection efficiency which will, if not corrected form, result in inaccurate estimations of the activity present in the human skeleton. Using these Monte Carlo results for the first time correction factors were calculated to correct skull geometry efficiency calibrations for all major critical head parameters. These factors can be used to determine "individual-specific" calibration factors. Additionally it can be assumed that the correction factors calculated in this work can also be also applied to other partial body counter calibrations.

The GEANT4 benchmark performed in this work showed that this code produces results identical to the MCNPX at 59.54 keV. However, for lower energies GEANT4 demonstrated to be superior thanks to the use of the Penelope physics list, which are specially designed for low-energy particles transport problems.
All simulations results demonstrate that the Monte Carlo codes are able to reproduce the experimental measurements in all major aspects. Monte Carlo simulations have several advantages compared to measurements such as being more flexible, less expensive, time saving, and able to provide better statistics than the measurement results. These advantages are particularly important given the limitations of the physical phantoms which are very expensive to build, for which only a very limited number available world-wide. Additionally all phantoms contain features that are not representative of the human anatomy, e.g. an incomplete fill of the brain region, and an incorrect description of scalp thickness. On the other hand, state of the art computational phantoms, due to their great detail, are closer to the human anatomy than physical phantoms, and through their flexibility are easily adjustable to individual specific dimensions. Taking in account the advantages provided by the use of computational tools demonstrated in this work it is expected that in the near by future physical phantoms calibrations will be fully replaced by computational phantoms and numerical calibrations.

In an effort to improve the accuracy of dose estimations after internal contamination, the methods and correction factors provided in this work allow every partial body counter user to correct his standard skull calibration to achieve "individual-specific" calibration factors for skull measurements without the need of further measurements or simulations. Thus, this work

is considered to provide a major improvement in internal dosimetry after incorporation of "bone seeking" radionuclides emitting low-energy photons.

As future work, the additional measurement positions on the skull surface should be investigated and the other detectors used should be simulated, to confirm if as assumed in this work, the corrections factors calculated for the HMGU detector 3 at the side position of the head can be used for all other positions and independent of the crystal size.

Additionally, as observed in the Case 1 and Case 2 measurements, the biokinetic of [241]Am has a significant role in the dose estimations from skull bone measurements. The impact of the detection efficiency from the [241]Am present in the soft tissues should be determined using Monte Carlo simulations, anthropomorphic phantoms and biokinetic retention curves from the surrounding tissues. Such results could then be used to determine correction factors for this time-dependent effect.

9 Scientific publications

9.1 Publications of this work in peer reviewed Journals and Proceedings

P. Nogueira, W. Rühm, T. Vrba, W. Buchholz, P. Fojtík, G. Etherington, D. Broggio, J. Huikari, O. Marzocchi, T. Lynch, A. Lebacq, C. Li, J. Ośko, D. Franck, B. Breustedt, D. Leone, J. Scott, A. Shutt, B. Hauck, K. Capello, B. Pérez-López, J. Francisco Navarro-Amaro, T. Pliszczyński, K. Fantínová, S. Tolmachev, M. López-Ponte. (in preparation) <u>EURADOS ^{241}Am *in-vivo* skull measurements intercomparison.</u>

T. Vrba, P. Nogueira, D. Broggio, M. Caldeira, K. Capello, K. Fantínová, C. de Sousa Figueira, J. Hunt, D. Leone, M. Murugan, O. Marzocchi, M. Moraleda, A. Shutt, S. Suh, M. Takahashi, K. Tymińska, M. A. Lopez, R. Tanner (Submitted). <u>EURADOS intercomparison exercise on MC modeling for the in-vivo monitoring of Am-241 in skull phantoms (Part I)</u>, Radiation Physics and Chemistry.

M. A. Lopez, J. Navarro Amaro, B. Pérez López, T. Navarro Bravo, P. Nogueira, T. Vrba (2013). <u>Acción EURADOS para la determinación de mericio en cráneo mediante medidas in-vivo y simulación Monte Carlo</u> (Spanish), 3 Congresso Conjunto SEFM 19 – SEPR 14, Cáceres.

9.2 Oral format publications of this work

EURADOS ^{241}Am Skull measurements intercomparison – preliminary results, EURADOS Annual meeting, Barcelona Spain, February 2013.

Monte Carlo Simulation of the real activity distribution pattern in a skull voxel phantom, ICRS-12 & RSPD-2012 - 12th International Conference on Radiation Shielding & 17th Topical Meeting of the Radiation protection and Shielding Division of ANS, Nara, Japan, September 2012.

EURADOS ^{241}Am Skull measurements intercomparison **-** progress report II, EURADOS Annual meeting, Vienna Austria, February 2012

EURADOS ^{241}Am Skull measurements intercomparison **-** progress report I, EURADOS WG7 plenary meeting, Gent Belgium, September 2011.

9.3 Poster format publications of this work

Partial body counter of the Institute of Radiation Protection, WE- Heraeus Advance Physics School on Ionizing Radiation and Protection of Man and his Environment, Bad Honnef Germany, May 2011.

9.4 Author publications in peer reviewed Journals

P. Nogueira, M. Zankl, H. Schattl, P. Vaz (2011). Monte Carlo calculation of fluence to eye lens absorbed dose conversion coefficients for monoenergetic electrons Physics in Medicine and Biology, Vol 56 pp. 6919–34.

R. Luís, J. Bento, G. Carvalhal, P. Nogueira, L. Silva, P. Teles, P. Vaz (2010). Parameter optimization of a planar BEGe detector using Monte Carlo simulations Nuclear Instruments and Methods in Physics Research, Vol 623, Issue 3 pp. 1014–9.

J. Bento*, P. Teles*, L. Silva, P. Nogueira, M. Neves, P. Vaz. Performance parameters of a Whole Body Counter; Radiation Measurements 2010, Vol 45, Issue 2 pp. 190–5.

P.Nogueira, L. Silva, P. Teles, J. Bento, P. Vaz (2010). Monte Carlo Simulation of the energy peak efficiency of a WBC Applied Radiation and Isotopes, Vol 68. Issue 1 pp. 184–9.

P. Nogueira, E. Fernandes, L. Silva, P. Teles, A.D. Oliveira, P. Vaz (2009). Monte Carlo Simulation of a Whole Body Counter International Journal of Low Radiation, Vol 6, Issue 4 pp. 312–24.

P. Nogueira, E. Fernandes, L. Silva, P. Teles, C. Carrapiço, P. Vaz, A.D. Oliveira (2008-2009). Simulação Monte Carlo de um contador de corpo inteiro Radioprotecção Vol II, Numero 14 e 15.

10 Bibliography

Agostinelli, S., J. Allison, K. Amako, J. Apostolakis, H. Araujo, P. Arce, M. Asai, D. Axen, S. Banerjee, G. Barrand, F. Behner, L. Bellagamba, J. Boudreau, L. Broglia, A. Brunengo, H. Burkhardt, S. Chauvie, J. Chuma, R. Chytracek, G. Cooperman, G. Cosmo, P. Degtyarenko, A. Dell'Acqua, G. Depaola, D. Dietrich, R. Enami, A. Feliciello, C. Ferguson, H. Fesefeldt, G. Folger, F. Foppiano, A. Forti, S. Garelli, S. Giani, R. Giannitrapani, D. Gibin, J. J. Gómez Cadenas, I. González, G. Gracia Abril, G. Greeniaus, W. Greiner, V. Grichine, A. Grossheim, S. Guatelli, P. Gumplinger, R. Hamatsu, K. Hashimoto, H. Hasui, A. Heikkinen, A. Howard, V. Ivanchenko, A. Johnson, F. W. Jones, J. Kallenbach, N. Kanaya, M. Kawabata, Y. Kawabata, M. Kawaguti, S. Kelner, P. Kent, A. Kimura, T. Kodama, R. Kokoulin, M. Kossov, H. Kurashige, E. Lamanna, T. Lampén, V. Lara, V. Lefebure, F. Lei, M. Liendl, W. Lockman, F. Longo, S. Magni, M. Maire, E. Medernach, K. Minamimoto, P. Mora de Freitas, Y. Morita, K. Murakami, M. Nagamatu, R. Nartallo, P. Nieminen, T. Nishimura, K. Ohtsubo, M. Okamura, S. O'Neale, Y. Oohata, K. Paech, J. Perl, A. Pfeiffer, M. G. Pia, F. Ranjard, A. Rybin, S. Sadilov, E. Di Salvo, G. Santin, T. Sasaki, N. Savvas, Y. Sawada, S. Scherer, S. Sei, V. Sirotenko, D. Smith, N. Starkov, H. Stoecker, J. Sulkimo, M. Takahata, S. Tanaka, E. Tcherniaev, E. Safai Tehrani, M. Tropeano, P. Truscott, H. Uno, L. Urban, P. Urban, M. Verderi, A. Walkden, W. Wander, H. Weber, J. P. Wellisch, T. Wenaus, D. C. Williams, D. Wright, T. Yamada, H. Yoshida and D. Zschiesche (2003). "Geant4—a simulation toolkit." Nuclear Instruments and Methods in Physics Research Section A: Accelerators, Spectrometers, Detectors and Associated Equipment **506**(3): 250-303.

Amako, K., S. Guatelli, V. N. Ivanchenko, M. Maire, B. Mascialino, K. Murakami, P. Nieminen, L. Pandola, S. Parlati, M. G. Pia, M. Piergentili, T. Sasaki and L. Urban (2005). "Comparison of Geant4 Electromagnetic Physics Models Against the NIST Reference Data." Nuclear Science, IEEE Transactions on **52**(4): 910-918.

Bento, J. T., P., L. Silva, P. Nogueira, M. Neves and P. Vaz (2010). "Performance parameters of a whole body counter." Radiation Measurements **45**(2): 190-195.

Berger, M. J. (1963). Monte Carlo Calculation of the penetration and diffusion of fast charged particles. Methods in computational physics. F. S. Alder B, Rotenberg M New York, Academic Press**:** 135–215.

Blumgart, H. L. and S. Weiss (1927). "STUDIES ON THE VELOCITY OF BLOOD FLOW: III. The Velocity of Blood Flow and its Relation to other Aspects of the Circulation in Patients with Rheumatic and Syphilitic Heart Disease." J Clin Invest **4**(2): 149-171.

Bolch, W., C. Lee, M. Wayson and P. Johnson (2010). "Hybrid computational phantoms for medical dose reconstruction." Radiation and Environmental Biophysics **49**(2): 155-168.

Breitenstein, B. D., C. E. Newton, H. T. Norris, K. R. Heid, B. Robinson, H. E. Palmer, G. A. Rieksts, H. B. Spitz, J. F. McInroy, H. A. Boyd, B. C. Eutsler, D. Romero, P. W. Durbin and C. T. Schmidt (1985). "The U.S. Transuranium Registry Report on the 241Am Content of a Whole Body." Health Physics **49**(4): 559-648.

Broggio, D., J. Bento, M. Caldeira, E. Cardenas-Mendez, J. Farah, T. Fonseca, C. Konvalinka, L. Liu, B. Perez, K. Capello, P. Cowan, J. A. Cruzate, L. Freire, J. M. Gómez-Ros, S. Gossio, B. Heide, J. Huikari, J. Hunt, S. Kinase, G. H. Kramer, O. Kurihara, A. Kyrieleis, A. L. Lebacq, D. Leone, C. Li, J. Li, L. C. Mihailescu, M. Moraleda, J. F. Navarro, C. Oliveira, N. Puerta, U. Reichelt, C. Simões, D. Sommer, M. Takahashi, P. Teles, F.

Vanhavere, T. Vrba, D. Franck, G. Gualdrini and M. A. Lopez (2012). "Monte Carlo modelling for the in vivo lung monitoring of enriched uranium: Results of an international comparison." Radiation Measurements **47**(7): 492-500.

Caon, M., G. Bibbo and J. Pattison (1999). "An EGS4-ready tomographic computational model of a 14-year-old female torso for calculating organ doses from CT examinations." Phys Med Biol **44**(9): 2213-2225.

Carinou, E., V. Koukouliou, M. Budayova, C. Potiriadis and V. Kamenopoulou (2007). "The calculation of a size correction factor for a whole-body counter." Nuclear Instruments and Methods in Physics Research Section A: Accelerators, Spectrometers, Detectors and Associated Equipment **580**(1): 197-200.

Chibani, O. and X. A. Li (2002). "Monte Carlo dose calculations in homogeneous media and at interfaces: A comparison between GEPTS, EGSnrc, MCNP, and measurements." Medical Physics **29**(5): 835-847.

Cohen, N., H. B. Spitz and M. E. Wrenn (1977). "Estimation of skeletal burden of "bone-seeking" radionuclides in man from in vivo scintillation measurements of the head." Health Phys **33**: 431-441.

Collaboration, G. (2009). Geant4 User's Guide for Application Developers

Cristy, M. and K. Eckerman (1987). Specific absorbed fractions of energy at various ages from internal photon sources. Oak Ridge, Tennessee, USA, Oak Ridge National Laboratory. **Report No. ORNL/TM-8381Nl**.

Currie, L. A. (1968). "Limits for qualitative detection and quantitative determination. Application to radiochemistry." Analytical Chemistry **40**(3): 586-593.

Debertin, K. and R. G. Helmer (1988). Gamma- and X-Ray Spectrometry with Semiconductor Detectors, North Holland.

Dimbylow, P. (1996). The development of realistic voxel phantoms for electromagnetic field dosimetry Workshop on Voxel Phantom Development. Chilton, UK**:** 1-7.

Dimov, I. T. M. S. (2000). Monte Carlo methods for applied scientists. [S.l.], World Scientific Publ. Co.

Doerfel, H. and F. Karlsruhe (2006). General Guidelines for the Estimation of Committed Effective Dose from Incorporation Monitoring Data: (project IDEAS - EU Contract No. FIKR-CT2001-00160), Forschungszentrum Karlsruhe.

Evans, R. D. (1937). "Radium poisoning. II. The quantitative determination of the radium content and radium elimination rate of living persons." American Journal of Roentgenol **37**: 10.

Farah, J., D. Broggio and D. Franck (2011). "Examples of Mesh and NURBS modelling for in vivo lung counting studies." Radiat Prot Dosimetry **144**(1-4): 344-348.

Ferrari, P. and G. Gualdrini (2005). "An improved MCNP version of the NORMAN voxel phantom for dosimetry studies." Phys Med Biol **50**(18): 4299-4316.

Fojtik, P. (2011). National Radiation Protection Institute personal communication

Fojtik, P., I. Malatova, V. Beckova and V. Pfeiferova (2013). "A case of occupational internal contamination with 241Am." Radiat Prot Dosimetry **156**(2): 190-197.

Fry, F. A. (1976). "Long-term Retention of Americium-241 Following Accidental Inhalation." Health Physics **31**(1): 13-20.

García-Talavera, M., H. Neder, M. J. Daza and B. Quintana (2000). "Towards a proper modeling of detector and source characteristics in Monte Carlo simulations." Applied Radiation and Isotopes **52**(3): 777-783.

Garny, S. (2009). Development of a Biophysical Treatment Planning System for the FRM II Neutron Therapy Beamline.

Gavaldà, F. S., J. M. F. Varea, J. S. Roma and O. d. C. i. D. Econòmic (2009). PENELOPE 2008: A Code System for Monte Carlo Simulation of Electron and Photon Transport : Workshop Proceedings, Barcelona, Spain 30 June-3 July 2008, OECD.

Genicot, J. L., V. Koukouliou and E. Carinou (2008). "Monte Carlo calculations applied to the parametrical studies in a whole body counter." Radiat Prot Dosimetry **128**(1): 49-61.

Gibbs, S. J., A. Pujol Jr, T.-S. Chen, A. W. Malcolm and A. E. James Jr (1984). "Patient risk from interproximal radiography." Oral Surgery, Oral Medicine, Oral Pathology **58**(3): 347-354.

Gilmore, G. (2008). Practical gamma-ray spectrometry, Wiley.

Giussani, A. (2013). Rentention Type S AMAD 1.

Gómez-Ros, J. M., L. de Carlan, D. Franck, G. Gualdrini, M. Lis, M. A. López, M. Moraleda, M. Zankl, A. Badal, K. Capello, P. Cowan, P. Ferrari, B. Heide, J. Henniger, V. Hooley, J. Hunt, S. Kinase, G. H. Kramer, D. Löhnert, S. Lucas, V. Nuttens, L. W. Packer, U. Reichelt, T. Vrba, J. Sempau and B. Zhang (2008). "Monte Carlo modelling of Germanium detectors for the measurement of low energy photons in internal dosimetry: Results of an international comparison." Radiation Measurements **43**(2–6): 510-515.

Goudsmit, S. and J. L. Saunderson (1940). "Multiple Scattering of Electrons." Physical Review **57**(1): 24-29.

Griffith, R. V., A. L. Anderson and J. C. Fisher (1978). Tissue-equivalent torso phantom for calibration of transuranic nuclide counting facilities Advances in Radiation Monitoring, IAEA Conference. Vienna. **IAEA-SM-229/56:** 4493-4504.

Gualdrini, G., P. Battisti, R. Biagini, P. De Felice, A. Fazio and P. Ferrari (2000). "Development and characterisation of a head calibration phantom for in vivo measurements of actinides." Applied Radiation and Isotopes **53**(1–2): 387-393.

Gualdrini, G., C. Daffara, K. W. Burn, P. Battisti, P. Ferrari and L. Pierotti (2005). "Monte Carlo modelling of a voxel head phantom for in vivo measurement of bone-seeker nuclides." Radiat Prot Dosimetry **115**(1-4): 320-323.

Halbleib, J. A., R. P. Kensek, G. D. Valdez, S. M. Seltzer and M. J. Berger (1992). "ITS: the integrated TIGER series of electron/photon transport codes-Version 3.0." Nuclear Science, IEEE Transactions on **39**(4): 1025-1030.

Hegenbart, L. (2009). Numerical Efficiency Calibration of In Vivo Measurement Systems. Doktor-Ingenieurs Dissertation, University of Karlsruhe - Karlsruhe Institute of Technology.

Hegenbart, L., S. Polz, A. Benzler and M. Urban (2012). "Voxel2MCNP: software for handling voxel models for Monte Carlo radiation transport calculations." Health Phys **102**(2): 221-229.

Hegenbart, L. and F. Schwabendand (2011). Physicalische Kalibrierphantome in der In-vivo-Messtechnik. Stralenschutzpraxis. **2:** 6.

Helmer, R. G., J. C. Hardy, V. E. Iacob, M. Sanchez-Vega, R. G. Neilson and J. Nelson (2003). "The use of Monte Carlo calculations in the determination of a Ge detector efficiency curve." Nuclear Instruments and Methods in Physics Research Section A: Accelerators, Spectrometers, Detectors and Associated Equipment **511**(3): 360-381.

Hendricks, J. S. (2000). Monte Carlo N-Particle Transport Code System MCNP4C.

HFERAG (2000). Human Engineering Design Data Digest, U.S. Department of Defense Human Factors Engineering Technical Advisory Group Washinton, DC**:** 158.

Hickman, D. P. (1987/8). Thesis.

Hickman, D. P. and N. Cohen (1988). "Reconstruction of a human skull calibration phantom using bone sections from an 241Am exposure case." Health Phys **55**(1): 59-65.

Hubbell, J. H. and S. M. Seltzer (2004). Tables of X-Ray Mass Attenuation Coefficients and Mass Energy-Absorption Coefficients (version 1.4). . http://physics.nist.gov/xaamdi [2013, November 7]. National Institute of Standards and Technology, Gaithersburg, MD.

Hunt, J. G., I. Malátová and S. Foltánová (1999). "Calculation and Measurement of Calibration Factors for Bone-Surface Seeking Low Energy Gamma Emitters and Determination of 241Am Activity in a Real Case of Internal Contamination." Radiation Protection Dosimetry **82**(3): 215-218.

Hurtado, S., M. García-León and R. García-Tenorio (2004). "GEANT4 code for simulation of a germanium gamma-ray detector and its application to efficiency calibration." Nuclear Instruments and Methods in Physics Research Section A: Accelerators, Spectrometers, Detectors and Associated Equipment **518**(3): 764-774.

IAEA (1999). Assessment of occupational exposure due to intakes of radionuclides: safety guide, International Atomic Energy Agency.

ICRP-23 (1975). Reference man: Anatomical, physiological and metabolic characteristics. ICRP Publication 23. Oxford, UK, Pergamon Press.

ICRP-70 (1995). Basic Anatomical & Physiological Data for use in Radiological Protection - The Skeleton. ICRP Publication 70. Oxford, UK, Pergamon Press.

ICRP-78 (1997). Individual Monitoring for Internal Exposure of Workers. ICRP Publication 78. Oxford, UK, Pergamon Press. **27**.

ICRP-89 (2002). Basic anatomical and physiological data for use in radiological protection: reference values. ICRP Publication 89. Oxford, UK, Pergamon Press.

ICRP-110 (2009). Adult Reference Computational Phantoms. ICRP Publication 110, Elsevier. **39**.

ICRU-44 (1989). Tissues Substitutes in Radiation Dosimetry and Measurements. ICRU Report 44. Bethesda, MD, International Commission on Radiation Units and Measurements.

ICRU-46 (1992). Photon, electron, proton and neutron interaction data for body tissues. ICRU Report 46. Bethesda, MD, International Commission on Radiation Units and Measurements.

ICRU-69 (2003). Direct Determination of the Body Content of Radionuclides. ICRU Report 69. Bethesda, MD, International Commission on Radiation Units and Measurements.

ICRU (2003). Direct Determination of the Body Content of Radionuclides. ICRU Report 69. Bethesda, MD, International Commission on Radiation Units and Measurements.

Institute, A. N. S. (1996). Performance criteria for radiobioassay. ANNSI N13.30. New York.

Ishikawa, T. and M. Uchiyama (1997). "Calculation of Counting Efficiency for 137Cs Using Voxel Phantoms with Lungs and a Skeleton." Radiation Protection Dosimetry **69**(3): 199-204.

Ishikawa, T. and M. Uchiyama (1997). "Estimation of the Counting Efficiences for Individual Subjects in 137Cs Whole Body Counting, Using Voxel Phantoms." Radiation Protection Dosimetry **71**(3): 195-200.

Jackson, M. and N. Lowe (2002). Advances in Isotope Methods for the Analysis of Trace Elements in Man, Taylor & Francis.

James, F. (1990). "A review of pseudorandom number generators." Computer Physics Communications **60**(3): 329-344.

Jeraj, R., P. J. Keall and P. M. Ostwald (1999). "Comparisons between MCNP, EGS4 and experiment for clinical electron beams." Physics in Medicine and Biology **44**(3): 12.

Johnson, L. C. (1964). "Morphologic Analysis in Pathology: The Kinetics of Disease and General Biology of Bone." In: Frost, H.M. (Ed.), Bone Biodynamics, Little Brown and Co., Boston, MA, USA,: 111.

Johnston, P. N. (1985). De-excitation of the L2 Subshell in Transradium Elements, La Trobe University.

Jurado Vargas, M. and A. L. Guerra (2006). "Application of PENELOPE code to the efficiency calibration of coaxial germanium detectors." Applied Radiation and Isotopes **64**(10–11): 3.

Kathren, R. L., T. P. Lynch and R. J. Traub (2003). "Six-year follow-up of an acute 241Am inhalation intake." Health Phys **84**(5): 576-581.

Kawrakow, I. (2000). "Accurate condensed history Monte Carlo simulation of electron transport. I. EGSnrc, the new EGS4 version." Med Phys **27**(3): 13.

Kellar, J. (1995). Fabrication of an Anthropomorphic Calibration Phantom for In Vivo Measurement of 152Eu in the Skull. MS project, University of Cincinnati

Kim, C. H., J. H. Jeong, W. E. Bolch, K. W. Cho and S. B. Hwang (2011). "A polygon-surface reference Korean male phantom (PSRK-Man) and its direct implementation in Geant4 Monte Carlo simulation." Phys Med Biol **56**(10): 3137-3161.

Knoll, G. F. (2010). Radiation Detection and Measurement, John Wiley & Sons.

König, K., W. Wahl, W. Rühm and W. Burkart (1998). "Direct beta measurements to determine in vivo whole-body activities of 90Sr in residents of the southern Urals: description of a new method." Radiation and environmental biophysics **37**(1): 6.

Kovtun, A. N., V. B. Firsanov, V. I. Fominykh and G. A. Isaakyan (2000). "Metrological Parameters of the Unified Calibration Whole-Body Phantom with Gamma-Emitting Radionuclides." Radiation Protection Dosimetry **89**(3-4): 239-242.

Kramer, G. H., L. C. Burns and S. Guerriere (2002). "Monte Carlo simulation of a scanning detector whole body counter and the effect of BOMAB phantom size on the calibration." Health Phys **83**(4): 526-533.

Kramer, G. H. and B. M. Hauck (2006). "The sliced bomab phantom: a new variant for intercomparison." Health Phys **90**(2): 161-166.

Kramer, R., H. J. Khoury, J. W. Vieira and V. J. Lima (2006). "MAX06 and FAX06: update of two adult human phantoms for radiation protection dosimetry." Phys Med Biol **51**(14): 3331-3346.

Kramer, R., M. Zankl, G. Williams and G. Drexler (1982). The calculation of dose from external photon exposures using reference human phantoms and Monte-Carlo methods, Part 1: The male (ADAM) and female (EVA) adult mathematical phantoms. Munich, Gesellschaft fur Strahlen-und Umweltforschung gmbH. **GSF report S-885**.

Laborie, J. M., G. Le Petit, D. Abt and M. Girard (2000). "Monte Carlo calculation of the efficiency calibration curve and coincidence-summing corrections in low-level gamma-ray spectrometry using well-type HPGe detectors." Applied Radiation and Isotopes **53**(1–2): 57-62.

Laurer, G. (1993). Letter to W. Burkhart from 8th April 1993, New York University Medical Center. Laboratory for Radiation Studies.

Lebacq, A. L., M. Bruggeman and F. Vanhavere (2011). "Efficiency calibration of a whole-body-counting measurement setup using a modular physical phantom." Radiat Prot Dosimetry **144**(1-4): 411-414.

Lee, C., J. L. Williams, C. Lee and W. E. Bolch (2005). "The UF series of tomographic computational phantoms of pediatric patients." Med Phys **32**(12): 3537-3548.

Lee, M. H., E. C. Jung and K. S. Song (2008). "Determination of a Minimum Detectable Activity through a Measurement of Pu Isotopes in Environmental Samples." BULLETIN-KOREAN CHEMICAL SOCIETY **29**(6): 5.

Lewis, H. W. (1950). "Multiple Scattering in an Infinite Medium." Physical Review **78**(5): 526-529.

Lopez, M. A., D. Broggio, K. Capello, E. Cardenas-Mendez, N. El-Faramawy, D. Franck, A. C. James, G. H. Kramer, G. Lacerenza, T. P. Lynch, J. F. Navarro, T. Navarro, B. Perez, W. Ruhm, S. Y. Tolmachev and E. Weitzenegger (2011). "EURADOS intercomparison on measurements and Monte Carlo modelling for the assessment of americium in a USTUR leg phantom." Radiat Prot Dosimetry **144**(1-4): 295-299.

López, M. A., J. F. Navarro, T. Navarro, J. M. Gómez Ros and M. Moraleda (2004). In-vivo calibration of a LE Ge Detection System for the assessment of Americium in bone at the WBC of CIEMAT. IRPA 11, Madrid.

Lopez, M. N., P. (2012). EURADOS - Internal Dosimetry Network. Annual Report FY2011/2012. M. D. Parker and S. Y. Tolmachev. Washinton State University, United States Transuranium and Uranium Registries.

Luís, R., J. Bento, G. Carvalhal, P. Nogueira, L. Silva, P. Teles and P. Vaz (2010). "Parameter optimization of a planar BEGe detector using Monte Carlo simulations." Nuclear Instruments and Methods in Physics Research Section A: Accelerators, Spectrometers, Detectors and Associated Equipment **623**(3): 1014-1019.

Malátová, I., V. Becková, T. Vrba and H. Pospísilová (2004). Exposure of workers from Intake of 241Am in the Czech Republic. 11th International Congress of the IRPA, , Madrid, Spain.

Malátová, I. and S. Foltánová (2000). "Uncertainty of the Estimation of 241Am Content of the Human Body." Radiation Protection Dosimetry **89**(3-4): 295-299.

Malátová, I., S. Foltánová and T. Novotný (1999). Estimation of the 241Am Content in the Skeleton of a Person Contaminated 25 years ago. 6th SRP International Symposium, Southport.

Mallett, M. W., D. P. Hickman, D. A. Kruchten and J. W. Poston, Sr. (1995). "Development of a method for calibrating in vivo measurement systems using magnetic resonance imaging and Monte Carlo computations." Health Phys **68**(6): 773-785.

Marzocchi, O. (2011). Design and Setup of a New HPGe Detector Based Body Counter Capable of Detecting Also Low Energy Photon Emitters. Dr. Ing., University of Bologna.

McInroy, J. F., H. A. Boyd, B. C. Eutsler and D. Romero (1985). "The U.S. Transuranium Registry report of the 241Am content of a whole body. Part IV: Preparation and analysis of the tissues and bones." Health Phys **49**(4): 587-621.

Metropolis, N. and S. Ulam (1949). "The Monte Carlo method." J Am Stat Assoc **44**(247): 335-341.

Moraleda, M., J. M. Gómez-Ros, M. A. López, T. Navarro and J. F. Navarro (2004). "A MCNP-based calibration method and a voxel phantom for in vivo monitoring of 241Am in

skull." Nuclear Instruments and Methods in Physics Research Section A: Accelerators, Spectrometers, Detectors and Associated Equipment **526**(3): 551-559.

Moraleda, M., J. M. Gómez-Ros, M. A. López, T. Navarro and J. F. Navarro (2005). "A Monte Carlo-based knee phantom for in vivo measurements of 241Am in bone." Nuclear Instruments and Methods in Physics Research Section A: Accelerators, Spectrometers, Detectors and Associated Equipment **538**(1–3): 731-737.

Navarro, J. F., M. A. López, T. Navarro, J. M. G. Ros and M. Moraleda (2007). "ASSESSMENT OF THE INTERNAL DOSE OF 241Am IN BONE BY IN VIVO MEASUREMENTS OF ACTIVITY DEPOSITED IN KNEE." Radiation Protection Dosimetry.

Nogueira, P., W. Rühm, T. Vrba, M. Volnhals, L. M. and Z. M. (2012). Oral Presentation: Monte Carlo Simulation of the real Activity distribution pattern in a Skull Voxel Phantom. ICRS-12 & RSPD-2012 - 12th International Conference on Radiation Shielding & 17th Topical Meeting of the Radiation protection and Shielding Division of ANS,, Nara, Japan.

Nogueira, P., L. Silva, P. Teles, J. Bento and P. Vaz (2010). "Monte Carlo simulation of the full energy peak efficiency of a WBC." Applied Radiation and Isotopes **68**(1): 184-189.

Nogueira, P., L. Silva, P. Teles, E. Fernandes, A. D. Oliveira and P. Vaz (2009). "A Monte Carlo simulation of a whole body counter." International Journal of Low Radiation **6**(4): 312-324.

Nogueira, P., M. Zankl, H. Schlattl and P. Vaz (2011). "Dose conversion coefficients for monoenergetic electrons incident on a realistic human eye model with different lens cell populations." Phys Med Biol **56**(21): 6919-6934.

Noßke, D. (2013). Cortical bone and Trabecular Bone retention curves, personal communication.

Noßke, D. and K. Karcher (2014). DOSAGE Biokinetic quality assurance software, personal comunication**:** 1.

Palmer, H. E., H. B. Spitz and G. A. Rieksts (1985). "US Transuranium Registry report on the SU Am content of a whole body. Part III: Gamma-ray measurements." Journal Name: Health Phys.; (United States); Journal Volume: 4: Medium: X; Size: Pages: 577-586.

Pelowitz, D. B. (2008). "MCNPX User's Manual, LA-CP-07-1473, Version 2.6.0."

Perry-Castañeda. (2008). "Perry-Castañeda Map Collection, Europe Political Map (http://www.lib.utexas.edu/maps/)."

Perry-Castañeda. (2008a). "Perry-Castañeda Map Collection, North America Political Map (http://www.lib.utexas.edu/maps/)."

Petoussi-Henss, N., M. Zankl, U. Fill and D. Regulla (2002). "The GSF family of voxel phantoms." Phys Med Biol **47**(1): 89-106.

Pölz, S. (2014). Personalized body counter calibration using anthropometric parameters. PhD.

Poon, E. and F. Verhaegen (2005). "Accuracy of the photon and electron physics in GEANT4 for radiotherapy applications." Med Phys **32**(6): 1696-1711.

Reines, F., R. L. Schuch, C. L. Cowan, Jr., F. B. Harrison, E. C. Anderson and F. N. Hayes (1953). "Determination of total body radioactivity using liquid scintillation detectors." Nature **172**(4377): 521-523.

Reynaert, N., H. Palmans, H. Thierens and R. Jeraj (2002). "Parameter dependence of the MCNP electron transport in determining dose distributions." Med Phys **29**(10): 2446-2454.

Ros, J. M., M. Moraleda, M. A. Lopez, T. Navarro and J. F. Navarro (2007). "Monte Carlo based voxel phantoms for in vivo internal dosimetry." Radiat Prot Dosimetry **125**(1-4): 161-165.

Rühm, W., K. König, I. Malátová, H. Doerfel, S. Foltanova, P. Sahre, R. Schütz and W. Wahl (1998). "Intercomparison Exercise for the Determination of 241Am in the Human Skeleton." Radiation Protection Dosimetry **79**(1-4): 517-521.

Rühm, W., R. Truckenbrodt and K. König (1997). Einrichtung und betrieb einer inkorporationsmeßstelle Bayer zur direktbestimmung der Körperaktivität. München, Bundesamt für Strahlenschutz.

Sachse, F. B., C. D. Werner, K. Meyer-Waarden and O. Dossel (2000). "Development of a human body model for numerical calculation of electrical fields." Comput Med Imaging Graph **24**(3): 165-171.

Salvat, F. and O. N. E. Agency (2001). Penelope: A Code System for Monte Carlo Simulation of Electron and Photon Transport, Workshop Proceedings, Issy-les-Moulineaux, France 5-7 November 2001, OECD Nuclear Energy Agency.

Salvat, F., J. M. Fernandez-Varea, E. Acosta and J. Sempau (2001). The physics of electron / positron transport in PENELOPE. Ninth EGS4 User's Meeting Tsukuba, Japan.

Segars, W. P. (2001). Development and application of the new dynamic NURBS-based cardiac-torso (NCAT) phantom, University of North Carolina at Chapel Hill.

Segars, W. P. and B. M. W. Tsui (2009). "MCAT to XCAT: The Evolution of 4-D Computerized Phantoms for Imaging Research." Proceedings of the IEEE **97**(12): 1954-1968.

Seltzer, S. M. (1991). "Electron-photon Monte Carlo calculations: The ETRAN code." International Journal of Radiation Applications and Instrumentation. Part A. Applied Radiation and Isotopes **42**(10): 917-941.

Shipman, P., A. Walker and D. Bichell (1985). The human skeleton, Harvard University Press.

Shirotani, T. (1988). "Realistic Torso Phantom for Calibration of in-vivo Transuranic-Nuclide Counting Facilities." Journal of Nuclear Science and Technology **25**(11): 875-883.

Sievert, R. M. and B. Hultqvist (1957). "Some Swedish investigations of the radioactivity in the human body." Br. J. Radiology(7): 12.

Snyder, W., M. Ford, G. Warner and H. Fisher (1969). "Estimates of absorbed fractions for monoenergetic photon source uniformly distributed in various organs of a heterogeneous phantom. Medical Internal Radiation Dose Committee (MIRD) " J. Nuclear Med. **10**.

Spitz, H. B. and J. Lodwick (2000). "Design, Fabrication & Evaluation of a New Calibration Phantom for In vivo Measurement of Bone-seeking Radionuclides." Radiation Protection Dosimetry **89**(3-4): 275-282.

Spitzer, V. M., D. G. Whitlock and N. L. o. Medicine (1998). Atlas of the Visible Human Male: Reverse Engineering of the Human Body, Jones and Bartlett Publishers.

Strulab, D., G. Santin, D. Lazaro, V. Breton and C. Morel (2003). "GATE (geant4 application for tomographic emission): a PET/SPECT general-purpose simulation platform." Nuclear Physics B - Proceedings Supplements **125**(0): 75-79.

Tabatadze, G., R. R. Brey, A. C. James and N. N. R. (2008). "USTUR case 0102 voxel phantom for external radiation detector response simulation." 3rd Annual Meeting of the Health Physics Society; July 13–17; Pittsburgh, PA. .

Taranenko (2005). VOXEL PHANTOM SETUP IN MCNPX. American Nuclear Society Topical Meeting in Monte Carlo.

Thompson, R. C. (1983). "1976 Hanford americium exposure incident: overview and perspective." Health Phys **45**(4): 837-845.

Tolmachev, S. (2012). United States Transuranium and Uranium Registries personal communication.

Toohey, R., E. Palmer, L. Anderson, C. Berger, N. Cohen, G. Eisele, B. Wachholz and W. Burr, Jr. (1991). "Current status of whole-body counting as a means to detect and quantify previous exposures to radioactive materials. Whole-body Counting Working Group." Health Phys **60 Suppl 1**: 7-42.

Truckenbrodt, R., W. Rühm and K. König (1999). "In vivo measurements of Am-241 in the human skeleton." Kerntechnik **64**: 5.

Vaz, P. (2010). "Monte Carlo methods and techniques status and prospects for future evolution." Applied Radiation and Isotopes **68**(4–5): 536-541.

Vrba, T. (2007). "Development and application of anthropomorphic voxel phantom of the head for in vivo measurement." Radiation Protection Dosimetry **127**(1-4): 201-204.

Vrba, T. (2010a). "Head calibration phantoms for actinides: measurements and simulations." Radiation Protection Dosimetry **144**(1-4): 357-360.

Vrba, T. (2010b). "Comparison of geometries for in vivo measurements of actinides in the skull." Appl Radiat Isot **68**(4-5): 918-921.

Vrba, T. (2010c). Development of Approaches for Realistic Retrospective Evaluation of Doses of selected Cases of Internal Contamination. Third European IRPA Congress, Helsinki, Finland

Vrba, T. (2012). Influence of Head Shape on Measured Activity of Actinides. IRPA13, Glasgow, Scotland.

Vrba, T., I. Malátová, P. Fojtík, M. Fülöp and P. Ragan (2013). "A SIMPLE PHYSICAL PHANTOM FOR AN INTERCOMPARISON EXERCISE ON 241Am ACTIVITY DETERMINATION IN THE SKULL." Radiation Protection Dosimetry.

Vrba, T., P. Nogueira, D. Broggio, M. Caldeira, K. Capello, K. Fantínová, C. Figueira, J. Hunt, D. Leone, M. Murugan, O. Marzocchi, M. Moraleda, A. Shutt, S. Suh, M. Takahashi, K. Tymińska, M. Antonia Lopez and R. Tanner (2013). "EURADOS intercomparison exercise on MC modeling for the in-vivo monitoring of Am-241 in skull phantoms (Part I)." Radiation Physics and Chemistry(0).

Wernli, C. and J. Eikenberg (2007). "Twenty-year follow-up of a Pu/Am inhalation case." Radiat Prot Dosimetry **125**(1-4): 506-512.

Williams, G., M. Zankl, W. Abmayr, R. Veit and G. Drexler (1986). "The calculation of dose from external photon exposures using reference and realistic human phantoms and Monte Carlo methods." Phys Med Biol **31**(4): 449-452.

Xu, X. G., T. C. Chao and A. Bozkurt (2000). "VIP-Man: an image-based whole-body adult male model constructed from color photographs of the Visible Human Project for multi-particle Monte Carlo calculations." Health Phys **78**(5): 476-486.

Xu, X. G. and K. F. Eckerman (2010). Handbook of Anatomical Models for Radiation Dosimetry, Taylor & Francis.

Xu, X. G. and C. Shi (2005). Preliminary development of a 4d anatomical model for monte carlo simulation. Monte Carlo 2005 Topical meeting. The Monte Carlo method: versatility unbounded in a dynamic computing world, Chattanooga, TN.

Xu, X. G., V. Taranenko, J. Zhang and C. Shi (2007). "A boundary-representation method for designing whole-body radiation dosimetry models: pregnant females at the ends of three gestational periods--RPI-P3, -P6 and -P9." Phys Med Biol **52**(23): 7023-7044.

Xu, X. G., J. Y. Zhang and Y. H. Na (2008). Preliminary data for mesh-based deformable phantom development:is it possible to design person-specific phantoms on demand? ICRS-11 and RPSD 2008 Radiation Shielding and the 15th Topical Meeting of the Radiation. Protection and Shielding Division, Callaway Gardens, Pine Mountain, Georgia, USA

Zankl, M. (2007). State of the art of voxel phantom development. Uncertainty Assessment in Computational Dosimetry: A comparison of approaches, Bologna, Italy, 8-10 October 2007.

Zankl, M., K. F. Eckerman and W. E. Bolch (2007). "Voxel-based models representing the male and female ICRP reference adult — the skeleton." Radiation Protection Dosimetry.

Zankl, M., R. Veit, G. Williams, K. Schneider, H. Fendel, N. Petoussi and G. Drexler (1988). "The construction of computer tomographic phantoms and their application in radiology and radiation protection." Radiation and Environmental Biophysics **27**(2): 153-164.

Zubal, I. G., C. R. Harrell, E. O. Smith, Z. Rattner, G. Gindi and P. B. Hoffer (1994). "Computerized three-dimensional segmented human anatomy." Med Phys **21**(2): 299-302.

List of figures

List of tables

11 Appendix

11.1 Detection Efficiency

The detection efficiency also known as full energy peak efficiency is a relation between the peak area and the amount of radioactivity measured. The detection efficiency can be divided in two components: the geometrical efficiency and intrinsic geometry. The first one accounts for the number of photons emitted and the number of photons arriving to the detector surface (solid angle between source and detector), while the second one accounts for the photons energy which rules the absorption and full energy deposition in the detector volume. Due to the dependence on the geometry and the energy of the photons, it is required to use calibration sources with the same shape and photon energies to the measured sample of unknown activity.

The relation between the measured number of counts in the full energy peak efficiency and the sample activity can be described as following:

$$\varepsilon = \frac{N}{A\gamma T} \qquad \qquad 11.1$$

where ε is the full energy peak efficiency,
N is the total number of counts in the region of interest area minus the background counts,
A is the activity of the radionuclide measured,
γ is the emission probability of the gamma of interest, and
T is the measurement time in seconds.

Acknowledgments / Agradecimentos

Foremost, I wish to thank Prof. Dr. Werner Rühm for the guidance and support of my PhD study and research, for his motivation, enthusiasm, and hard questions.
I also wish to thank my thesis committee members: Maria Zankl and Dr. Maria Lopez, for their guidance and encouragement.

Special thanks to my colleagues Christian Pioch, Matthias Volnhals and Sebastian Trinkl for their help and guidance into the GEANT4 world.

My sincere thanks to all my colleagues that have been nearby in the last years and have motivated me in my work: Vladimir Mares, Josef Irlinger, Ferdinand Bergmeier, Tomasz Maczka, and Dr. Marek Wielunski.

I would also like to thank Gerhard Donth, Anita Herrling, and Judith Brehme, for their support to my work.

I also would like to thank to Case 1 and Case 2 for their cooperation and allowing the publication of their data.

Furthermore, I wish to thank all researchers from the Institutes who provided data and scientific support to my work, especially the ones from the BfS Institute.

I thank also my old colleagues from ITN Portugal that have introduced and guided me into the field of radiation detection physics and Monte Carlo methods: Dr. Pedro Vaz, Lidia Silva, Joana Bento, Raul Luis, Ana Belchior, Pedro Teles, Yuri Romanets, Carlos Carapiço, Dr. Augusto Oliveira, and Dr. João Alves.

Agradeço aos meus pais pelos seus conselhos, encorajamento e por sempre acreditarem em mim. E aos meus sogros pela sua motivação.

Por fim, um agradecimento muito especial do fundo do meu coração à minha namorada e à minha filha pela sua ajuda, encorajamento e paciência, sem as quais este doutoramento nao teria sido possível.

CURRICULUM VITAE

Name: Pedro Miguel Agostinho Nogueira
Birthday: 22-12-1981
Nationality: Portuguese
Address: Reschreiterstr 19
80933 München, Deutschland

PROFESSIONAL EXPERIENCE

December 2010 – Present

> PhD position at the Helmholtz Zentrum München under the guidance of Prof. Dr Werner Rühm. The main subjects are:

- Internal dosimetry
  - Calibration of a Partial Body Counter composed by 4 Germanium detector's for human skull measurements.
  - Quantification of the influence of body parameters on the detection efficiency of a Partial Body Counter.

- Computational dosimetry
  - Development of a computational set-up of a Partial Body Counter for the Monte Carlo code GEANT4 (C++).
  - Development of suitable voxel phantoms for a "personalize" (patient dependent) calibration of a PBC.

March 2010 – May 2010

> Leonardo da Vinci scholarship at the Medical Informatics department of the University Hospital Hamburg Eppendorf (UKE). Under the guidance of Dr René Werner I develop the following activities.

- Principles of intensity modulated radiation therapy (IMRT).
- Registration based 4D motion modeling.
- 4D dose calculation for IMRT.
  - Influence of the weighting factor.
  - Influence of the temporal resolution.

June 2008 – February 2010

> Research scholarship from Foundation for Science and Technology at ITN (Instituto Tecnológico e Nuclear de Portugal). Under the supervision of Prof. Dr Pedro Vaz I develop the following activities.

- Computational dosimetry
  - Development of a mathematical and voxel phantom of the human eye for calculation of the dose conversion coefficients for the eye lens. Project developed under de guidance of Dr Maria Zankl.

- Monte Carlo simulations
  - Development of a computational setup in MCNPX for the determination of the physical parameters and calibration of the detection system of a Whole Body Counter.
  - Development of a computational setup in MCNPX for a nonstandard geometry calibration of a Brood energy germanium detector.

- Gamma ray spectrometry
  - Calibration of the detection system of a Whole Body Counter using a RMC-II Phantom.

- Thermoluminescence dosimetry
  - Evaluation of termoluminescence properties of Lithium Borate crystals. Project developed under the guidance of Dr João Alves.

January 2008 – May 2008

Research scholarship in the scientific project *ASEMWATERNET* at *INETI /LNEG* (Laboratório Nacional de Engenharia e Geologia).

During this period I performed the characterization of the effluent receiver systems in the river Mondego (Coimbra, Portugal). Project was done under supervision of Dr José Cardoso Duarte.

March 2007 – December 2007

Research scholarship in the scientific project *Bio-Reactor Jet-Loop* at *INETI* (*Instituto Nacional de Engenharia, Tecnologia e Inovação*). National Institute of Engineering Technology and Innovation

Project focused on the influence of the mechanical and hydraulical parameters in the microbial population in a reactor type jet-Loop (bio-reactor *SPURT*). The influence of mechanical parameters and the type of microflora and the development and application of innovative methods for analysis and control of the involved biomass in the treatments was also studied. Project was done under supervision of Dr José Cardoso Duarte.

September 2005 - December 2006

      Internship at CBME (The Centre for Molecular and Structural Biomedicine)

      Development of a Monte-Carlo simulation of the electron transfer kinetics in a small segment of the electronic chain of transport in mitochondrial internal membrane of mice. Project was done under supervision of Prof. Dr Jorge Martins.

Education & Qualifications

2010-Present: PhD candidate (Dr. rer. biol. hum.) at the Medical Faculty of the Ludwig-Maximilians University Munich.
Thesis: Person-specific calibration of a Partial Body Counter.
Mid-term PhD evaluation: Principles of radiobiology in radiotherapy and Oncological nuclear imaging using Positron Emission Tomography.

2010-Present: Student on the doctoral program Helena Helmholtz Graduate School Environmental Health.

2008-2009: Postgraduation in "Radiological Security and Protection" at the Technical Superior Institute of Lisbon Technical University, with the final average of Sixteen (16/20).

1999-2006: Licenciatura (Four years Degree) in Biochemistry obtained at the University of Algarve, with the final average of Fourteen (14/20).

Eidesstattliche Versicherung

Agostinho Nogueira, Pedro Miguel
Name, Vorname

Ich erkläre hiermit an Eides statt,

dass ich die vorliegende Dissertation mit dem Thema

Person-specific Calibration of a Partial Body Counter

selbständig verfasst, mich außer der angegebenen keiner weiteren Hilfsmittel bedient und alle Erkenntnisse, die aus dem Schrifttum ganz oder annähernd übernommen sind, als solche kenntlich gemacht und nach ihrer Herkunft unter Bezeichnung der Fundstelle einzeln nachgewiesen habe.

Ich erkläre des Weiteren, dass die hier vorgelegte Dissertation nicht in gleicher oder in ähnlicher Form bei einer anderen Stelle zur Erlangung eines akademischen Grades eingereicht wurde.

Ort, Datum   Unterschrift Doktorandin/Doktorand